UNIVERSITY OF CALIFORNIA

Los Angeles

Biophysical investigation of 2D embryonic stem cell derived cardiomyocytes

A dissertation submitted in partial satisfaction of the requirements for the degree Doctor of Philosophy in Chemistry

by

Huanqi Zhu

2015

ABSTRACT OF THE DISSERTATION

Biophysical investigation of 2D embryonic stem cell derived cardiomyocytes

by

Huanqi Zhu

Doctor of Philosophy in Chemistry

University of California, Los Angeles, 2015

Professor James K. Gimzewski, Chair

Human embryonic stem cell derived cardiomyocytes (hESC-CMs) can be potential used to in a stem cell-based regenerative therapy to cure heart related disease. The maturity of HESC-CMs still remains fetal-type even though many differentiation protocols have been discovered. In the first part of the thesis, I will focus on electrical physiological characterization of the maturation process of a confluent layer of hESC-CMs. With the high throughput of monitoring microelectrode array (MEA) system, we observed the development of hESC-CMs over weeks and analyze the electrophysiological features during maturation in great detail. In the second part of the thesis, we further investigate the external factors that can affect maturation process of stem cell derived cardiomyocytes in vitro such as electrical stimulation. In the third part of the thesis, the mechanical properties of cancer cells are explored. We discussed the role of mechanical factor in cancer cells. This could add a new dimensional approach in characterize and enhance the maturation of hESC-CMs in future research. In the fourth part of the thesis, we present

nanoscale characterization of action and actin binding proteins using Atomic Force Mircoscope (AFM).

The dissertation of Huanqi Zhu is approved.

Thomas G. Mason

Jian Yu Rao

James K. Gimzewski, Committee Chair

University of California, Los Angeles

2015

Dedicated to my family and friends

Table of Contents

List of Tables

List of Figures

Acknowledgements

Chapter 2 is a version of Huanqi Zhu, Adam Z. Stieg, James K. Gimzewski, Haruko Nakano, and Atsushi Nakano, 2015, "High resolution electrophysiological assessment of Human Embryonic stem cell-derived cardiomyocytes".

Chapter 3 is a version of Huanqi Zhu, Haruko Nakano, Atsushi Nakano, Adam Z. Stieg, and James K. Gimzewski. 2015, "Overdrive suppression of Mouse stem cell-derived cardiomyocytes using Microelectrode Array".

Chapter 4 is a version of Alia Ghoneum, Huanqi Zhu, JungReem Woo, Nikita Zabinyakov, Shivani Sharma, and James K. Gimzewski, 2014, "Biophysical and Morphological Effects of Nanodiamond/Nanoplatinum Solution (DPV576) on Metastatic Murine Breast Cancer Cells in Vitro", Nanotechnology 25, 46510. The published manuscript carries the following acknowledgement: Authors would like to acknowledge support from International Center for Materials Nanoarchitectonics Satellite (MANA), National Institute for Materials Science (NIMS), Tsukuba, Japan. We acknowledge the use of the Scanning Probe Microscope facility at the Nano and Pico Characterization Laboratory at the CNSI. SEM image courtesy Venex Co., Ltd. Kanagawa, Japan.

Chapter 5 is a version of Shivani Sharma, Huanqi Zhu, Elena E. Grintsevich, Emil Reisler, and James K. Gimzewski, 2013, "Correlative nanoscale imaging of actin filaments and their complexes", *Nanoscale* 2013(5), 5692-5702. The published manuscript carries the following acknowledgement: Authors would like to acknowledge support from International Center for Materials Nanoarchitectonics Satellite (MANA), National Institute for Materials Science (NIMS),

Tsukuba, Japan (J.K.G.), California Nanosystems Institute, UCLA (S.S.) and USPHS grant R01 GM 077190 (E.R.).

Vita

2010-2012	M. S. Chemistry: University of California, Los Angeles
2006-2010	B.S. in Physics: University of Science and Technology of China

2015	Part-time in Wyzerr
2014	Internship in Western digital

Publications

- Hirohito Shimizu, Johann Schredelseker, Jie Huang, Kui Lu, Shamim Naghdi, Fei Lu, Sarah Franklin, Hannah DG. Fiji, Kevin Wang, **Huanqi Zhu**, Cheng Tian, Billy Lin, Haruko Nakano, Amy Ehrlich, Junichi Nakai, Adam Z Stieg, James K. Gimzewski, Atsushi Nakano, Joshua I. Goldhaber, Thomas M. Vondriska, Gyorgy Hajnoczky, Ohyun Kwon, and Jau-Nian Chen, **2015**, "Mitochondrial $\mathbf{Ca^{2+}}$ uptake by the voltage-dependent anion channel 2 regulates cardiac rhythmicity", *eLife* 2015(4) e04801.
- Alia Ghoneum*, **Huanqi Zhu***, JungReem Woo, Nikita Zabinyakov, Shivani Sharma, and James K. Gimzewski, **2014**, "Biophysical and Morphological Effects of Nanodiamond/Nanoplatinum Solution (DPV576) on Metastatic Murine Breast Cancer Cells *in Vitro*", *Nanotechnology* **25** 46510. (* equally contributed)
- Shivani Sharma, **Huanqi Zhu**, Elena E. Grintsevich, Emil Reisler, and James K. Gimzewski, **2013**, "Correlative nanoscale imaging of actin filaments and their complexes", *Nanoscale* 2013(5), 5692-5702.

Manuscripts in preparation

- **Huanqi Zhu**, Adam Z. Stieg, James K. Gimzewski, Haruko Nakano, and Atsushi Nakano, **2015**, "High resolution electrophysiological assessment of Human Embryonic stem cell-derived cardiomyocytes".
- **Huanqi Zhu**, Haruko Nakano, Atsushi Nakano, Adam Z. Stieg, and James K. Gimzewski. **2015**, "Overdrive suppression of Mouse stem cell-derived cardiomyocytes using Microelectrode Array".

Chapter 1.

Introduction

1.1 Introduction of Heart Disease and Stem Cell Based Therapy

Heart disease describes a range of conditions that affect human heart, such as blood vessel diseases, arrhythmias, and heart defections[1-2]. It is the leading cause of death for both men and women in the United States. According to the Center for Disease Control and Prevention, about 610,000 people die of heart disease in the United States every year – that's 1 in every 4 deaths. Almost 735,000 Americans suffer from a heart attack every year and often develop a condition called heart failure (HF). There are an increasing number of deaths due to heart disease until 1980. After that, the number remains high with a slow declining.

HF or myocardial infarction (MI) happens when the flow of oxygen-rich blood to a section of heart muscle suddenly becomes blocked and the heart can't get oxygen[3]. The section of heart muscles becomes "starved" for oxygen during the blockage and begins to die. The damage is irreversible after 30 minutes of blockage. HF may have destructive effects on the renal, respiratory and hepatic organ systems.

Patients suffering from HF often have issues with heart arrhythmia, and approximately half of all deaths related to HF result from arrhythmias[4]. An arrhythmia is a problem with the rate or rhythm of the heartbeat. The heart can beat too fast (tachycardia), too slow (bradycardia), or with an irregular rhythm. The heart may not be able to pump enough blood to the body during an arrhythmia, which causes damages to the brain, heart, and other organs.

While healthy lifestyle serves as primary or secondary prevention, treatments with medications are often necessary for most patients with HF. Common medications include diuretics, inotropes, vasodilators, and beta blockers. However, one major limitation of these therapies is that they do not address the underlying cause of myocardial dysfunction[5]. Because of these shortcomings, people have been searching for new methods of treatment.

One promising solution is to replace the malfunction/damaged cells with correct cells and restore the heart function[6-8]. It has been assumed that if enough correct cells can be generated, they would be able to replace cells that have been lost or damaged by disease. People follow the same idea in looking for treatment in HF. The heart contraction function can be restored if new heart muscle cells (cardiomyocytes) replace the damaged cells after a HF.

Several distinct cell types have been used in experimental and pilot trials. The question that which cells are best suited for cardiac regeneration and vascularization remained open. One of the promising approaches is the stem cell based therapy[8-9]. The potential of human pluripotent stem cells to self-renew indefinitely and differentiate into virtually any cell types makes them a valuable source for cell-based regenerative therapy, human developmental studies, disease modeling, and drug discovery/assessment[10-12]. There is a growing recognition that the stem cell based therapy will play a more and more important role in heart disease treatment. As the human heart is the least regenerative of tissues, cardiomyocytes derived from human embryonic stem cell/induced pluripotent stem cells (hESC/iPSC-CMs) provide a particularly powerful biological tool[13-18]. The National Institutes of Health US$2.5 billion, 5.2 billion on stem cell research in the period of 2004-2007, 2011-2014, respectively.

To treat the heart disease, various stem cell resources have been investigated such as human embryonic stem cells, adult stem cells from bone marrow, and cardiac progenitor cells. Despite the ethical issue that human embryonic stem cells derivation requiring the destruction of human embryos which is quite debatable in many countries, human embryonic stem cells have many advantages and are very promising for realizing cardiac regeneration through cardiomyocyte replacement because of their high capacity to undergo directed differentiation into genuine cardiomyocytes and supportive cardiac cells.

1.2 The challenge of hESC-CMs approach

Acquiring a large amount of mature cardiac cells is significant for clinical research. Although multiple differentiation protocols have evolved over the years to allow for large scale induction of human cardiomyocytes, the maturity of hESC/iPC-CMs remains fetal-type. In fact, the contractile force generated by mouse ESC-derived cardiomyocytes are in general about 1/10 of that by isolated neonatal cardiomyocytes[19]. Efforts have been made to study the maturation process of cardiomyocytes and find ways to further induce the maturation of hESC/iPC-CMs in vitro, with promising results with tissue engineering approaches, electrical stimulation, and mechanical loading[20-22].

During embryogenesis, the heart is the first functional organ to develop and needs to be operational while it is still rapidly proliferating and forming. This mandates the embryonic heart to strike a delicate balance between its genesis and functionality. The induction of distinct cardiac gene program is only the first step of the cardiogenesis. Subsequent to induction, cardiomyocytes undergo remarkable maturation into structurally and functionally competent cardiomyocytes during fetal stages, including the assembly of contractile proteins into myofibrillar structure, expression of ion channel and gap junctions at the right location, organization of mitochondria and SR along the myofibrils, etc. Although the analysis of late-stage cardiogenesis is clinically more relevant than that of early-stage differentiation process, our understanding of the maturation process is still at its primitive stage. For example, it was demonstrated only recently that Nkx2-5, one of the most characterized transcription factors in the heart, plays totally opposite roles in the proliferation of cardiac progenitors/myocytes during early vs late cardiogenesis[23]. As the maturity level of the cardiomyocytes is relatively less

reflected in mRNA expression pattern, the functional properties of hESC-CMs are critical parameters to monitor.

Currently, people have characterized the structural changes and functional changes during the maturation process. The cell shape changed from a circular shape during immature stage to a rod shape in mature stage. And the contractile proteins are assembled and aligned together in mature stage. There is an increased cardiac gene expression during the maturation process.

1.3 Biophysical Methods in hESC-CMs study

The definitive characteristic that distinguishes the heart tissues environment from other organs is its rhythmic physical contraction. A comprehensive understanding of how cardiac myocytes maturate in this unique biophysical environment at fetal stages is critical for both deeper understanding of the pathogenesis of congenital heart disease and application of PSCs to cardiac regeneration[20, 24].

Our view of mammalian cardiogenesis was modified by the discovery of the second heart field. Although it remains controversial whether the SHF represents another “organ field” for the heart, discovery of the SHF is biologically important in that it implies cardiac progenitors are continuously added to the heart tube in multiple “temporal” waves. This temporal difference, rather than spatial difference, creates a unique interaction between already mature myocardium and the late-migrating progenitors: Ad demonstrated by us and others, late-migrating multipotent cardiac progenitors in the SHF become progressively exposed to the unique electromechanical environment generated by already maturated myocardium. In other words, while cardiomyocytes

differentiate to produce the electromechanical field in the developing heart, we postulate that unique electromechanical environment in turn serves as a cue for the progenitors to further maturate. Despite accumulating knowledge of how the myocardium matures to generate unique electromechanical forces, little is known about how the electromechanical field induces cardiogenesis.

Biophysical cues have been known to play a role in the functionality of rat neonatal ventricular bardiomyocytes and ES cells. Prior studies including ours have demonstrated that contractile forces and stiffer scaffolds increase the maturity of cardiomyocytes. However far less is known about the role of electromechanical cues during the differentiation of human ESC-CMs. Cardiomyocytes maturate to generate unique biophysical activities, which in turn can affect the maturation of cardiac progenitors, forming a positive feedback loop between genetic mechanisms and biophysical environments. We explore the electromechanical forces as a cause as well as a consequence of cardiac maturation.

The role of electromechanical cues in cardiogenesis is fully examined by several new modalities. We have recently established a high-yield 2D culture mothod of human ESC-CM from Norio Nakatsuji (Kyoto University). Electromechanical properties are measured by super resolution confocal microscopy (STED), atomic force microscopy (AFM), and multielectrode arrays (MEA)[25-29]. Genetic/epigenetic high throughput screening of transcriptome and methylome is performed at our High Throughput Sequence Core.

1.4 References

1. Berul, C.I., *Arrhythmias in Adult Congenital Heart Disease.* Cardiology, 2015. **131**: p. 80-80.
2. Stammen, K., et al., *Congenital heart disease: Arrhythmias, cardiopulmonary bypass, and "grown-ups".* Essentials of Pediatric Anesthesiology, 2015: p. 78-94.
3. Rosendorff, C., *Treatment: special conditions Co-existing heart disease: coronary artery disease, myocardial infarction, heart failure.* Journal of the American Society of Hypertension, 2015. **9**(8): p. 651-654.
4. Wellens, H.J.J., *Cardiac arrhythmias: The quest for a cure - A historical perspective.* Journal of the American College of Cardiology, 2004. **44**(6): p. 1155-1163.
5. Bairey Merz, C.N., et al., *ACCF/AHA/ACP 2009 competence and training statement: a curriculum on prevention of cardiovascular disease: a report of the American College of Cardiology Foundation/American Heart Association/American College of Physicians Task Force on Competence and Training (Writing Committee to Develop a Competence and Training Statement on Prevention of Cardiovascular Disease): developed in collaboration with the American Academy of Neurology; American Association of Cardiovascular and Pulmonary Rehabilitation; American College of Preventive Medicine; American College of Sports Medicine; American Diabetes Association; American Society of Hypertension; Association of Black Cardiologists; Centers for Disease Control and Prevention; National Heart, Lung, and Blood Institute; National Lipid Association; and Preventive Cardiovascular Nurses Association.* J Am Coll Cardiol, 2009. **54**(14): p. 1336-63.

6. Pompilio, G., et al., *Bone Marrow Cell Therapy for Ischemic Heart Disease The Never Ending Story*. Circulation Research, 2015. **117**(6): p. 490-493.

7. Ishigami, S., et al., *Cardiac progenitor cell therapy reduces myocardial fibrosis and stiffness to improve cardiac function in patients with univentricular heart disease.* European Heart Journal, 2015. **36**: p. 685-685.

8. Sanina, C. and J.M. Hare, *Mesenchymal Stem Cells as a Biological Drug for Heart Disease Where Are We With Cardiac Cell-Based Therapy?* Circulation Research, 2015. **117**(3): p. 229-233.

9. Wehman, B. and S. Kaushal, *The Emergence of Stem Cell Therapy for Patients With Congenital Heart Disease*. Circulation Research, 2015. **116**(4): p. 566-569.

10. Suemori, H., et al., *Efficient establishment of human embryonic stem cell lines and long-term maintenance with stable karyotype by enzymatic bulk passage.* Biochemical and Biophysical Research Communications, 2006. **345**(3): p. 926-932.

11. Takahashi, S., et al., *Comparative single-institute analysis of cord blood transplantation from unrelated donors with bone marrow or peripheral blood stem-cell transplants from related donors in adult patients with hematologic malignancies after myeloablative conditioning regimen.* Blood, 2007. **109**(3): p. 1322-1330.

12. Yu, J.Y., et al., *Induced pluripotent stem cell lines derived from human somatic cells.* Science, 2007. **318**(5858): p. 1917-1920.

13. Mummery, C.L., *Human embryonic stem cells: possibilities for future cell transplantation therapy.* Tijdschrift Voor Diergeneeskunde, 2002. **127**(6): p. 189-191.

14. Laflamme, M.A., et al., *Cardiomyocytes derived from human embryonic stem cells in pro-survival factors enhance function of infarcted rat hearts.* Nature Biotechnology, 2007. **25**(9): p. 1015-1024.

15. Kattman, S.J., et al., *Stem Cells and Their Derivatives: A Renaissance in Cardiovascular Translational Research.* Journal of Cardiovascular Translational Research, 2011. **4**(1): p. 66-72.

16. Willems, E., et al., *Small-Molecule Inhibitors of the Wnt Pathway Potently Promote Cardiomyocytes From Human Embryonic Stem Cell-Derived Mesoderm.* Circulation Research, 2011. **109**(4): p. 360-U38.

17. Kibayashi, T., et al., *Development of an in vitro imaging system for the study of the mechanisms underlying mesenchymal stem cell transmigration across the blood brain barrier.* Journal of Neurochemistry, 2012. **123**: p. 112-112.

18. Arshi, A., et al., *Rigid microenvironments promote cardiac differentiation of mouse and human embryonic stem cells.* Science and Technology of Advanced Materials, 2013. **14**(2).

19. Feinberg, A.W., et al., *Functional Differences in Engineered Myocardium from Embryonic Stem Cell-Derived versus Neonatal Cardiomyocytes.* Stem Cell Reports, 2013. **1**(5): p. 387-396.

20. Tulloch, N.L., et al., *Growth of Engineered Human Myocardium With Mechanical Loading and Vascular Coculture.* Circulation Research, 2011. **109**(1): p. 47-U195.

21. Lieu, D.K., et al., *Mechanism-Based Facilitated Maturation of Human Pluripotent Stem Cell-Derived Cardiomyocytes.* Circulation-Arrhythmia and Electrophysiology, 2013. **6**(1): p. 191-201.

22. Nunes, S.S., et al., *Biowire: a platform for maturation of human pluripotent stem cell-derived cardiomyocytes.* Nature Methods, 2013. **10**(8): p. 781-+.

23. Nakashima, T., et al., *Rapid electrical stimulation causes alterations in cardiac intercellular junction proteins of cardiomyocytes.* American Journal of Physiology-Heart and Circulatory Physiology, 2014. **306**(9): p. H1324-H1333.

24. Zhang, D.H., et al., *Tissue-engineered cardiac patch for advanced functional maturation of human ESC-derived cardiomyocytes.* Biomaterials, 2013. **34**(23): p. 5813-5820.

25. Clements, M. and N. Thomas, *High-Throughput Multi-Parameter Profiling of Electrophysiological Drug Effects in Human Embryonic Stem Cell Derived Cardiomyocytes Using Multi-Electrode Arrays.* Toxicological Sciences, 2014. **140**(2): p. 445-461.

26. Asai, Y., et al., *Combination of Functional Cardiomyocytes Derived from Human Stem Cells and a Highly-Efficient Microelectrode Array System: An Ideal Hybrid Model Assay for Drug Development.* Current Stem Cell Research & Therapy, 2010. **5**(3): p. 227-232.

27. Caspi, O., et al., *In Vitro Electrophysiological Drug Testing Using Human Embryonic Stem Cell Derived Cardiomyocytes.* Stem Cells and Development, 2009. **18**(1): p. 161-172.

28. Kujala, V.J., et al., *Averaging in vitro cardiac field potential recordings obtained with microelectrode arrays.* Computer Methods and Programs in Biomedicine, 2011. **104**(2): p. 199-205.

29. Otsuji, T.G., et al., *Progressive maturation in contracting cardiomyocytes derived from human embryonic stem cells: Qualitative effects on electrophysiological responses to drugs.* Stem Cell Research, 2010. **4**(3): p. 201-213.

Chapter 2.

Electrophysiological Characterization of the Maturation Process of hESC-CMs

2.1 Abstract

Current embryonic bodies (EBs) approach to study cardiomyocytes has limitations in compatibility with physical measurements and imaging systems, precluding the investigation of spatial resolved perperties such as in-pulse propagation, pace-making leader et al. Here we introduce a model system that utilizes a 2D confluent layer of human embryonic stem cells derived cardiomyocytes (hESC-CMs), allowing collective extracellular field potential monitoring of hESC-CMs at the full capacity of Microelectrode array (MEA) system, complementary with structural characterization using high resolution optical microscopic images and fluorescence immunostainings, further confirmed with detailed gene expression level analysis along the process. Implementation of this approach allows access to investigate hESC-CMs in vitro from a new and comprehensive angle.

2.2 Introduction

The potential of human pluripotent stem cells to self-renew indefinitely and differentiate into virtually any cell types makes them a valuable source for human developmental biology, cell-based regenerative therapy, disease modeling, and drug discovery/assessment [1-5]. As the human heart is the least regenerative of tissues, cardiomyocytes derived from human embryonic stem cell/induced pluripotent stem cells (hESC/iPSC-CMs) provide a particularly powerful biological tool [6-11]. The differentiation protocols have evolved over the years to allow for large-scale induction of human cardiomyocytes. Efforts have been made to induce further maturation of ESC/iPSC-CMs in vitro, with promising results with tissue engineering approaches, electrical stimulation, and mechanical loading[12-15]. However, the maturity of in vitro hESC/iPSC-CMs still remains fetal-type with the limited electromechanical properties. In fact,

the contractile force generated by the cardiomyocytes from pluripotent stem cells is roughly 10% of the cardiomyocytes isolated from the neonatal heart[16].

Subsequent to the induction of cardiac gene program during early cardiogenesis, cardiomyocytes undergo remarkable maturation process to develop into structurally and functionally competent cardiomyocytes during fetal stages, characterized by the assembly of contractile proteins into myofibrillar structure, expression of ion channels and gap junctions at the right location, organization of mitochondria and SR along the myofibrils, etc. The study of late-stage cardiogenesis is translationally relevant, as most of the events leading to congenital heart anomalies occur at fetal stages and cell therapy requires functional cardiomyocytes with strong contractile force. Although great progress has been made in the studies of specification and multilineage differentiation of cardiac progenitors, our understanding of the cardiac maturation process is still at its primitive stage[17]. While the differentiation level of the early cardiac progenitors are well defined by the marker gene expression, the maturity of the cardiomyocytes at late developmental stages is relatively less reflected in the gene expression pattern[18-21]. Given that the biophysical cues are not only the results but also the essential drivers of the cardiac maturation [11, 22-25], the electrophysiological properties of hESC-CMs are critical parameters to monitor.

Here, we introduce a model system that allows us to monitor the spatiotemporal maturation process of the electrophysiological activity of a confluent layer of hESC-CMs. Human H9 cell line is differentiated into cardiomyocytes lineage based on a protocol previously described[10]. After further processes, a confluent layer of hESC-CMs are cultured on substrate for comprehensive characterizations. We use the MultiChannel System to measure the induced electrical potential during the maturation process. This model allows the Microelectrode Array

(MEA) to function at its full capacity, enabling real-time (up to 40,000 samples/sec), and simultaneous acquisition of up to 120 channels from spatially distributed microelectrode. Furthermore, structural changes and reorganization of hESC-CMs are clearly assessed through image systems with the confluent layer sample. Morphologically changes during cardiac maturation are characterized with high resolution optical microscopy and fluorescence immunostainings. In addition to the above physical measurements, molecular readouts including gene expression are tested to in genetic level.

We first characterize the stability of cell culture using MEA. Intrinsic parameters representing the contraction motion of hESC-CMs such as beating rate, field potential amplitude and field potential duration are analyzed. Results show a stable period of 10 days with the hESC-CMs cultured in MEA. Spatial dependent properties of hESC-CMs are further explored. The pacemaker is identified in the confluent layer sample and its temporal behavior is shown for the first time. We observe the pacemaker is pretty stable within the short observation window (20 minutes in current setup), but changes positions from day to day. The conduction velocity is further calculated and showed to increase over time. These results are consistent with the observations in vivo. We also investigate morphological change of hESC-CMs over time through imaging systems. Both optical microscope and fluorescence stained images clearly show that hESC-CMs are well aligned at later stage compared with those in early stage. It shows how structural proteins organized into sarcolemma along the maturation.

This model provides access to spatial related research of hESC-CMs in vitro, allowing understanding the behavior of hESC-CMs maturation. It can be further used to test previous hypotheses and conclusions of cardiomyocytes that are draw in vivo.

2.3 Methods

Cell line and 2D cardiomyocytes culture protocol

Human H9 (WiCell) ES cells are grown on top of mouse embryonic fibroblast feeder in DMEM (Gibco) media supplemented with 20% Knock Out serum replacement (Life Technologies) and 8ng/ml bFGF (Peprotech) to keep them undifferentiated. H9 hESCs are differentiated into cardiomyocyte lineage using a protocol as previously described[1]. Floating cardiac colonies were collected and dispersed in protease solution (0.1% collagenase type I (Life Technologies), 0.25% trypsin, 1 U/mL DNase I (Applied Biosystems), 116 mMNaCl, 20 mM HEPES, 12.5 mM NaH2PO4, 5.6 mM glucose, 5.4 mMKCl, and 0.8 mM MgSO4, adjusted to pH 7.35). After dispersion, the cells are filtered using a 40μm cell strainer (BD Falcon) and are plated on Matrigel-coated (BD Biosciences) MEA. Usages of all the human ES cell lines are approved by the UCLA Embryonic Stem Cell Research Oversight (ESCRO) Committee and the Institutional Review Boards (IRB).

Microelectrode array measurements

Covered by a confluent layer of hESC-CMs, the MEA gives access to the cellular electrocardiogram (ECG), determined by the transmembraneous electrical changes during periodic action potentials in the cardiac muscle cell. Therefore, MEA measurements not only could provide long term, non-invasive monitoring the CMs from multiple microelectrodes simultaneously, but also allows the evaluation of spatial influence including signal pacemaker identification and signal propagation.

HESC-CMs (differentiation day 16) are plated on uncoated, microelectrode arrays (MEAs) containing 120 integrated TiN electrodes (30 µm diameter, 200 µm interelectrode spacing). The MEAs are placed in an incubator with a temperature of 37 °C and 5% CO_2. Two days are given to allow the cardiomyocytes to well attach to MEA surface and we start the recording at the differentiation state of day 18. Local field potentials (LFPs) at each electrode are collected over a period of 20 minutes, twice a day, and 3 weeks in total with a sampling rate of 1 KHz using the MEA2100-HS120 system (Multichannel systems, Reutlingen, Germany). Data analysis is carried out using the MC_DataTool (Multichannel Systems), Origin (OriginLab Corporation) and Matlab (MathWorks).

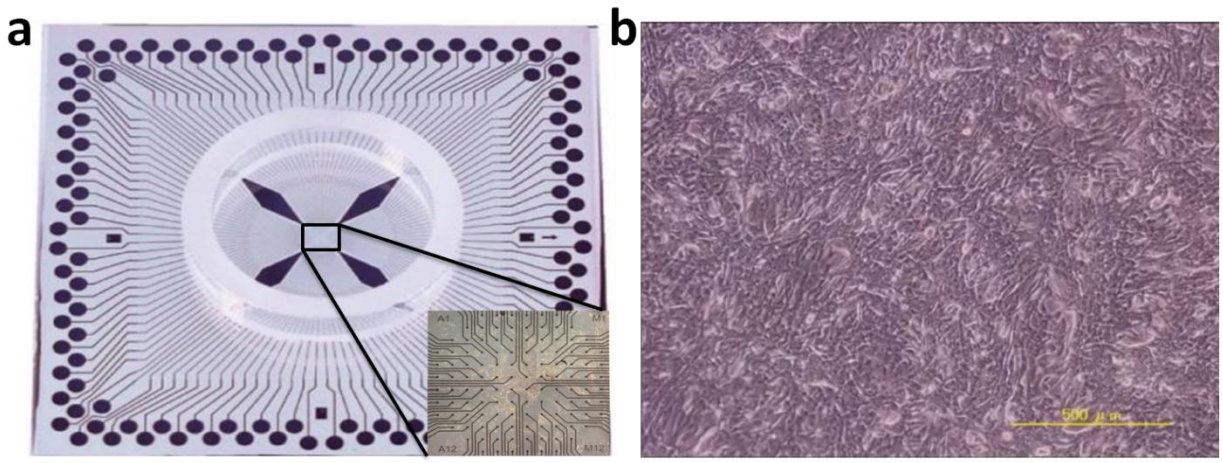

Fig 1. Schematic of the electrical characterization of human embryonic cardiomyocytes (hESC-CMs) using Microelectrode Array (MEA). (a) Schematic of a MEA chip with 120 monitoring electrodes located in the middle, subset optical image shows the layout of 120 electrodes. (b) Optical image of hESC-CMs. The scale bar is 500 µm. The hESC-CMs are sufficient to cover all electrodes in the MEA chip.

Data conversion

The raw data files acquired through the MEA2100-HS120 system are converted into ASCII files using the MC_DataTool. During the conversion, all 120 channels are selected from the channel configuration map following left to right, top to down order. The ASCII files contain 121 columns. The first column contains the sampling count information and the second to the last column represents time serial field potential data collected from 120 channels in the same order of electrodes being selected during the conversion. The local voltage features detected by each electrode could thus be extracted by analyzing the digital column data corresponding to that electrode.

Field potential peak detection

The digital signal collected from each electrode is a sequence of voltage spikes, which correspond to the contraction motion of the cardiomyocytes. One featured information is when the contraction happens exactly, i.e. local activation time (LAT). The time of first peak in the field potential wavelet is quantified as LAT. We use the Matlab function 'findpeaks' to accurately determine the LAT for all 120 channels after loading the ASCII file into Matlab program. Tunable parameters include 'minpeakheight' and 'minpeakdistance'. We set the 'minpeakheight' as 16 μV, considering the noise level in the MEA system was ± 8μV which means a noticeable peak has a minimum signal-to-noise ratio of 4. The 'minpeakdistance' is set as 1000 ms, which is based on the experimental observation that cardiomyocytes beat with an interval longer than 1000 ms. After locating the LAT of each peak in the field potential waveform, we calculate the peak-to-peak interval (beat interval) between each beat in every channel.

In general, the contraction motion of the whole cardiomyocytes is synchronized together, thus the beat intervals detected are quite close among each channel. We calculate the standard deviation of the beat interval for each channel. If the standard deviation from one channel is quite off from the majority, it is highly possible that it comes from a bad electrode with significant noise. To get rid of the misleading information from the noisy electrode, a threshold of 10% is used. If the standard deviation of beat interval from one channel is within 10% of the median standard deviation from all channels, that channel is used for further analysis. Otherwise information from that channel is discarded.

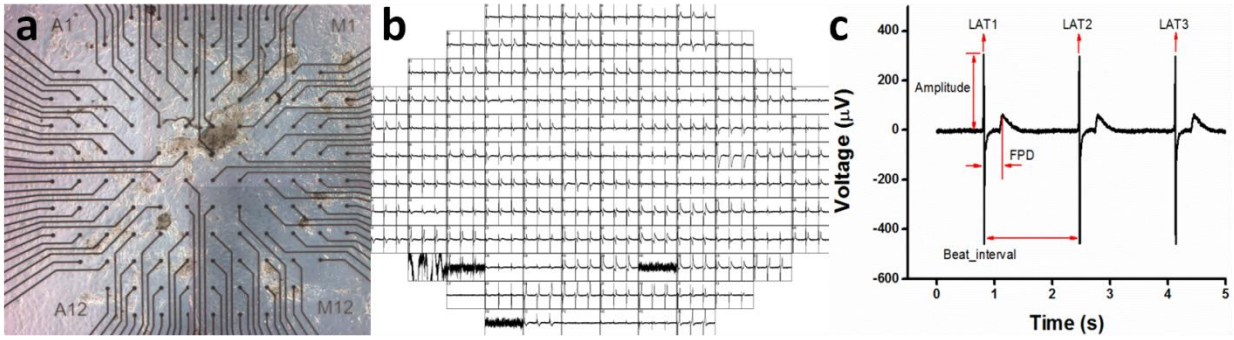

Fig 2. Schematic of the field potential monitoring of the rhythmic contraction motion of cardiomyocytes using MEA system. (a) Optical image of confluent layer human embryonic stem cell derived cardiomyocytes (hESC-CMs) on top of the 120 microelectrode array. The field potential signal can be monitored through all the electrodes simultaneously. (b) Screenshot of the real-time field potential signal of hESC-CMs from 120 electrodes. There are 4 noisy channels at the bottom because of the bad connections. (c) Representative Field potential signal collected from one of the 120 electrodes. Each electrical spike represents one contraction beat of the hESC-CMs. Features such as field potential amplitude, beat interval and field potential duration (FPD) can be quantified.

With the tunable parameters in ‘findpeaks’ and the threshold of acceptable standard deviation, we could get rid of the channels with significant noise level and accurately measure the LAT for all channels during the 20-minute recording period.

Beat interval calculation

The beat interval is measured as the peak-to-peak time difference in the field potential waveform. After above peak detection and threshold post-process, the beat interval and standard deviation are collected for all the channels except the significant noisy ones. In the time course development experiment, the confluent layer of cardiomyocytes covers the 2D electrode array pretty well. Typically around 100 out of 120 channels are selected to calculate the beat interval after the peak detection. Starting from cell age of 18 to day 38, the average beat interval and average standard deviation are calculated over the selected 100 channels at each 20-minitue recording period.

Pacemaker analysis

Pacemaker is identified as the leader in initializing the beating pace of cardiomyocytes. Quantitatively, pacemaker beats the fastest and also beats the earliest. To locate the pacemaker in the confluent layer of cardiomyocytes, the pacemaker in terms of generating the earliest beat is identified. The time for each electrical beat could be measured through the peak detection module. Whenever the cardiomyocytes contracts, the local activation time of that field potential waveform is measured for all the 120 channels. An earlier response time meant that channel is

closer to the pacemaker, assuming a wave-shape propagation nature of field potential starting from the pacemaker.

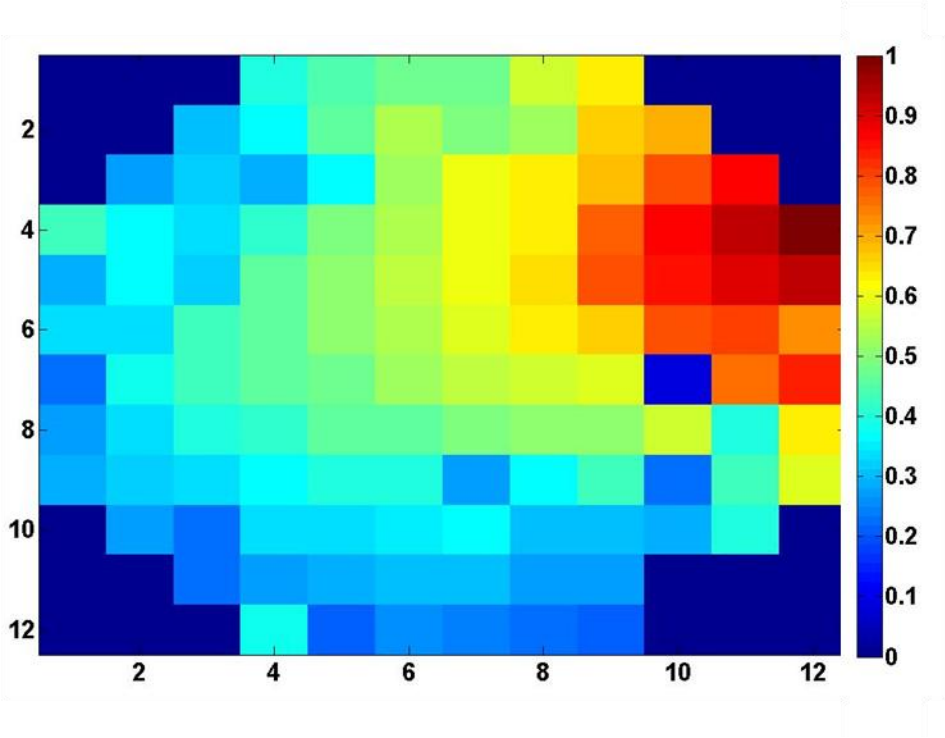

Fig 3. Representative contour plot of the pacemaker in the 2D human embryonic cardiomyocytes. The electrical firing of the field potential from all the electrodes is ranked by time. The activation time is then normalized between 0 and 1 (0 represents the last beat, and 1 represents the first beat). The red region in the contour plot shows the group of cells leading the pace of the 2D cardiomyocytes. A nice pace propagation is observed within the 120 electrodes.

The response time of all 120 channels is normalized between 0 and 1, which 1 represents the earliest beat and 0 represents the latest beat. The distribution of the response time over the MEA map is visualized with a color coded contour plot using Origin, where red presents 1 and black represents 0. A sequential contour plot could be generated during one recording period,

where most of the time the pacemaker contour plots are quite similar during that recording period. One representative figure is selected to represent the response time distribution at each 20-minitue recording period. Results at cell age of day 19 to day 30 are shown in Fig 3.

Conduction speed analysis

Conduction speed is defined as how fast the field potential propagated across the MEA surface. The time for each electrical beat is already measured through the peak detection. The time lag and distance of each channel with respect to the pacemaker (earliest beat identified from the 120 channels) are calculated. The conduction speed at each channel is therefore calculated. To calculate the average conduction speed at each recording period, the conduction speed is averaged in both 120 channels and the 20-minitues recording period. Results starting from cell age of day 18 to day 30 are shown in Fig 10.

True pacemaker identification

Pacemaker is identified as the leader in the whole cardiomyocytes. The localized pacemaker within the MEA electrode area is detected through the previous pacemaker analysis. The true pacemaker could fall outside the region of the MEA electrode area. Assuming the whole cardiomyocytes have only one pacemaker and the pace-generating signal propagates like a wave, the position of the true pacemaker could be back tracked based on the partial propagation waveform that is detected in the MEA electrode area.

Compared to the localized pacemaker, a contour plot of propagation time at each channel within the MEA electrode area is showed. Each archer-shape line has the same propagation time.

A circle could be fitted to the archer-shape line and the origin of the circle represents the location of the true pacemaker. A Matlab circle fit module developed by Izhak Bucher is adopted in the above process.

RNA and fluorescence test details

Total RNA (RNeasy Micro, Qiagen) is subjected to cDNA synthesis using qScript cDNA supermix (Quanta Biosciences). Quantitative RT- PCR was performed using SYBER Select Master Mix (Life Technologies) on Viia^{TM}7 system (Life Technologies). All values are normalized with respect to GAPDH expression level and expressed relative to day 5 hESC-CMs as 1.

2.4 Results

Transcriptional signature of hESC-CM

Differentiation of hESC-CMs recapitulates the embryonic development. We induced cardiomyocytes from hESCs and plated on MEA chip as described[10]. To analyze their molecular signature during in vitro cardiogenesis, H9 hESCs were differentiated and examined by RNA-seq. Expression profiling showed that mesodermal markers (Mesp1, Bry) were highest at day 2. Cardiac progenitor marker, ISL1, was at its peak at day 5. Spontaneous contraction started at around day 7. By day 14, major cardiac structural proteins, ion channels, and gap junctions become strongly expressed. At this stage, ~90% of the cells are MF20^{+} cardiomyocytes with typical sarcomeric structures.

Quatitative RT-PCR analysis demonstrated the upregulated expression of cardiac marker genes such as cardiac Troponin T, NKX2-5 compared to day 5 hESC derived cells corresponding to cardiac mesodermal stage. Cardiac maturation marker, such as the subtype ratio of myosin heavy chain β/α, glucose transporter 4/1, also showed higher expression than that of day 5.

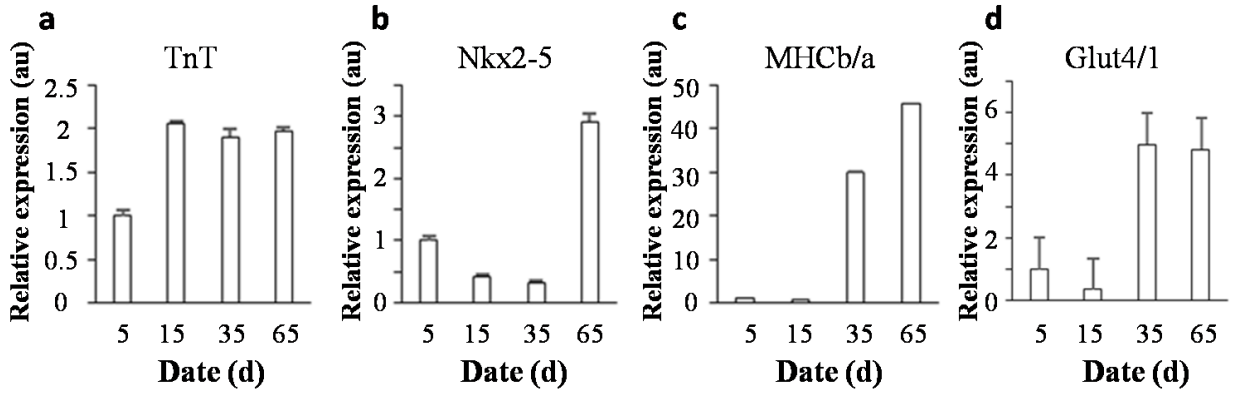

Fig 4. mRNA relative expression by qPCR up to 65 days. (a- d) represents the expression level of cardiac marker genes over time such as Troponin t (TnT), Nkx2-5, myosin heavy chain β/α (MHCb/a) and glucose transporter 4/1 (Glut4/1), respectively.

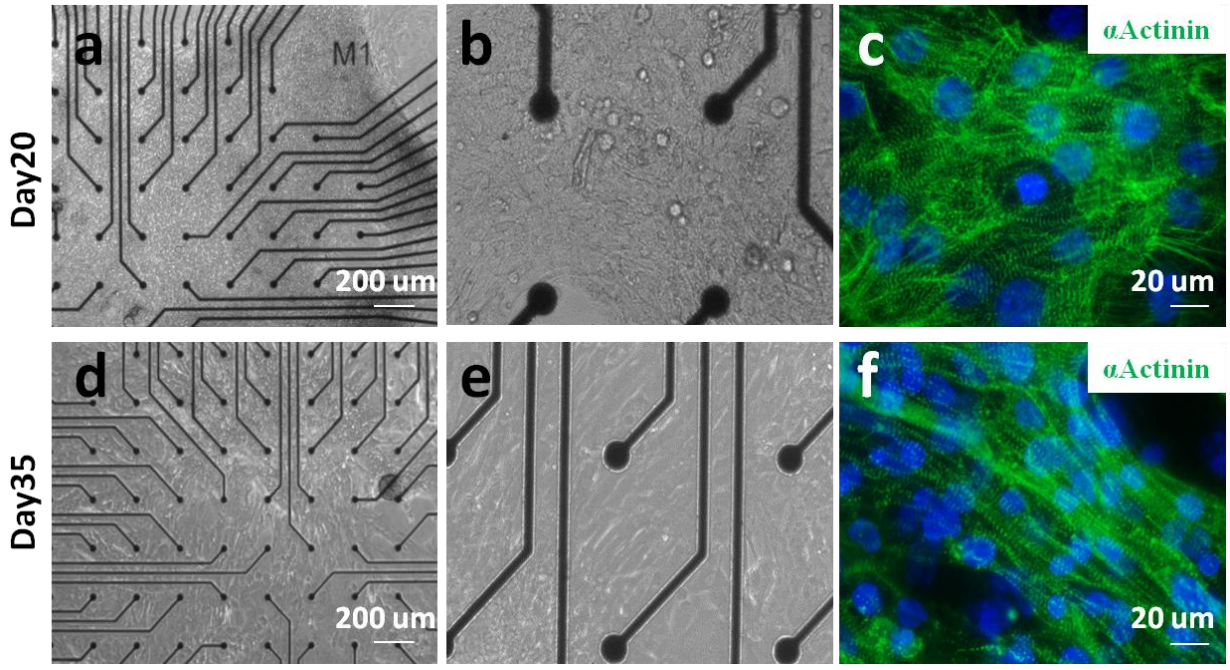

Fig 5. Morphological characterization of cardiomyocytes at different differentiation stages detected by optical microscope and fluorescence imaging. (a) Optical image of cardiomyocytes at differentiated age of day 20 on top of MEA. (b) Zoomed in optical image of (a). The cardiomyocyte cells have a disk-shape at this stage. (c) Fluorescence image of cardiomyocytes with α-actinin staining. The contraction protein is disordered at this stage. (d) Optical image of cardiomyocytes at differentiated age of day 35. (e) Zoomed in optical image of (d). The cardiomyocyte cells become a rod-shape and aligned well at this stage. (f) Fluorescence image of cardiomyocytes with α-actinin staining. The contraction protein is much well organized at this stage.

Molecular and cellular characterization of hESC-CMs

hESC-CM seeded on MEA chip were morphologically analyzed over time. Bright field and fluorescent images of differentiation day 20 hESC-CM (Fig 5a,b,c) demonstrated sarcomeric structures as shown in green striation but the cells are in a clumped and disorganized manner, whereas differentiation day 35 hESC-CM (Fig 5d,e,f) appeared to be much more elongated and oriented perpendicular to the lateral registration of sarcomeres. The well-aligned and organized cell orientation of hESC-CM at later stage showed the morphology development during the maturation process.

Time course of beat interval

Fig 6 showed the trend of beat interval and standard deviation over the 2 weeks recording window. hESC-CMs beat steadily and consistently for 10-14 days on MEA. The beat interval was around 2s with standard deviation below 0.0014s. Starting from day 28, the beating of the hESC-CM became unstable and irregular, since the beat interval fluctuates and its standard deviation changed dramatically. The results from three independent tests were consistent. This possibly reflected the technical limitation of the in vitro monolayer culture.

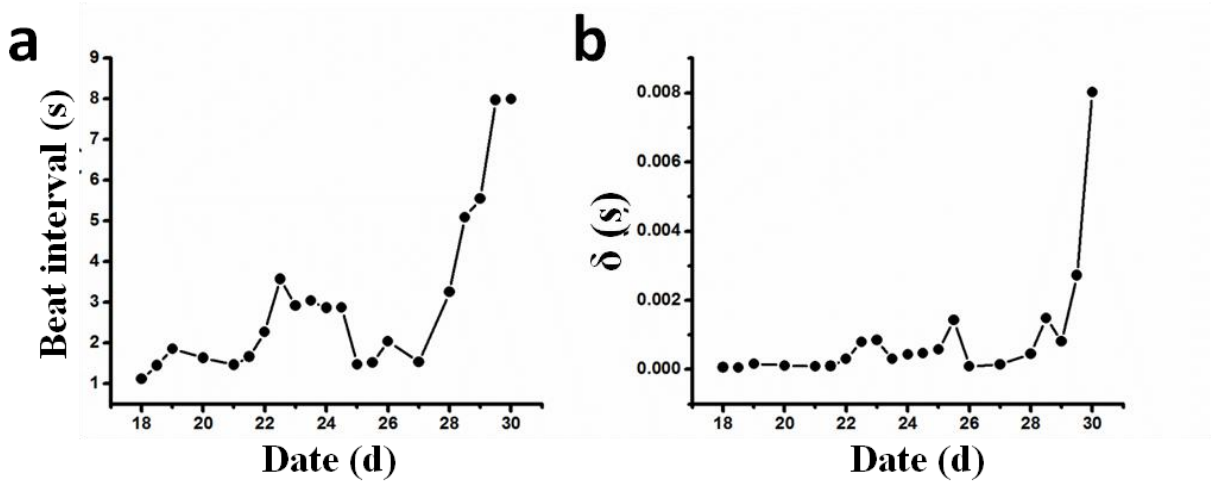

Fig 6. Beat interval and standard deviation of the field potential pattern of cardiomyocytes over 2 weeks recording. (a) The beat_interval trend showed a similar and steady beat rate for around 10 days after plating the cardiomyocytes. The beat rate fluctuated dramatically after day 28. (b) The standard deviation trend matched pretty well with beat_interval trend. High standard deviation meaning much irregular beating pattern was observed at later stage.

Field potential duration and amplitude

Field potential duration was around 0.3-0.4s and relatively stable throughout the differentiation. On the other hand, field potential amplitude rapidly increased until day 23 and started to decline at day 27-30. Again, the breaking point is around day 28 with our current culture system.

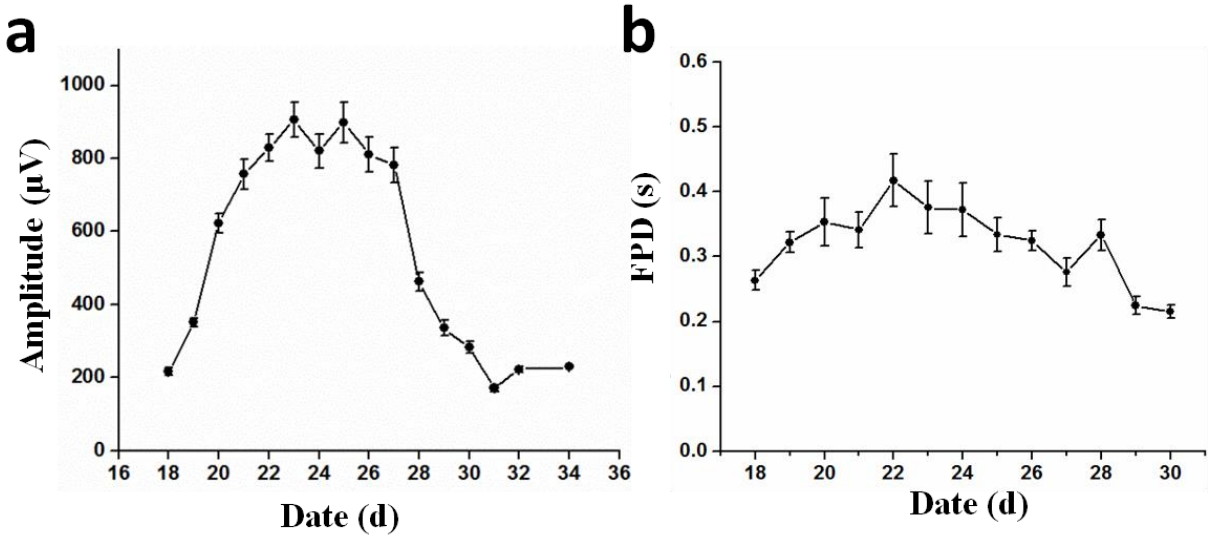

Fig 4. Field potential amplitude and duration of cardiomyocytes over 2 weeks recording. (a) The field potential amplitude showed an increased trend at the beginning and decreased from day 28. (b) The field potential duration was pretty stable within the 2 weeks recording period.

Activation map of field potential propagation

The electric activity of hESC-CMs is initialized by a small group of cells pacemaking cells and propagates to the surrounding cardiomyocytes connected via gap junction. The combination of confluent layer of hESC-CM and the large microelectrode array allows for position-dependent analysis of the electrical activities. The field potential propagation could thus be characterized by the phase difference of the field potential in each channel covered by the confluent layer of hESC-CM. Fig 8 showed representative field potential propagation waves at varying cell age from day 19 to 30. The propagation waveform generated circular wave fronts originating from a point source. Analysis over the 20-minitue recording window showed consistent propagation map, indicating that the pace making source was stable. However, the

propagation map changed over days as the orientation of the propagation indicated, indicating that the pacemaking source was not completely stable over long time.

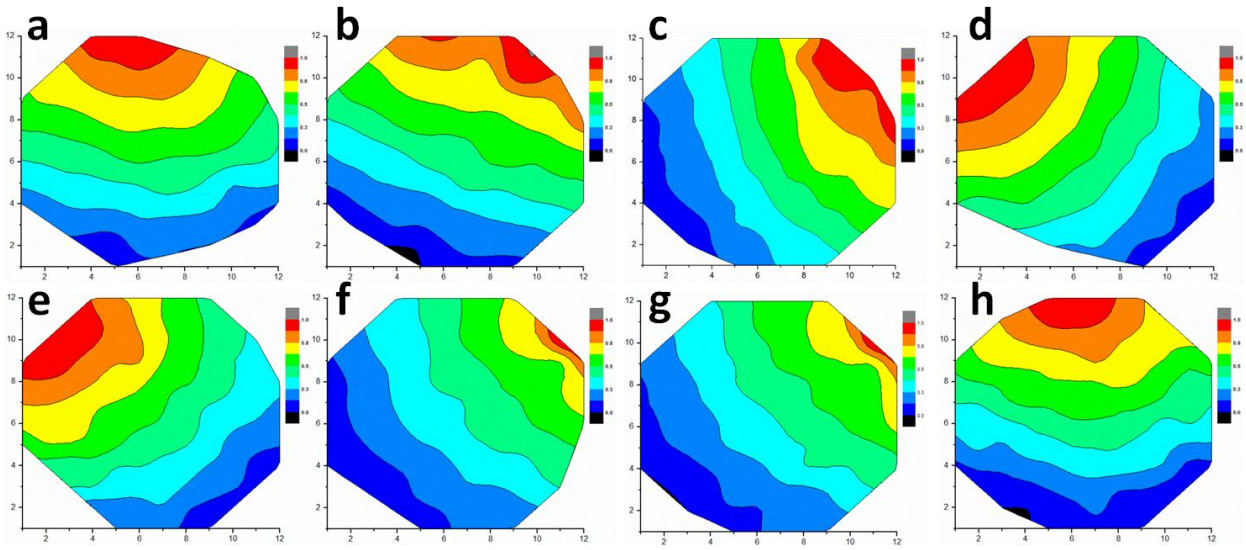

Fig 5. Representative contour plot of pacemaker in the 2D cardiomyocytes starting from cell age of day 19 to day 29. The activation time of the field potential at each electrode position was color coded between red (pacemaker) and blue (last follower). (a) – (h) represented the pacemaker map from cell age of day 19, 20, 21, 22, 23, 26, 28 and 29, respectively. The pacemaker was quite stable within the 20 minutes observation at each day, but their position changed over days.

Identification of pacemaking cells

The monolayer hESC-CMs extend over the electrode array within MEA plate. Therefore, the position of pacemaking cells may fall outside of the array of electrodes. Assuming that the propagation waves originate from a point source, the contour of activation map is approximated by circle. Hence, the radius of the curvature of the activation map of field potential can predict the location of pacemaking cells. Fig 9(c) showed that for pacemaker map Fig 9(a), the

coordinates of the true pacemaker was (10.0, 15.6) outside of the MEA, with the bottom left corner of the MEA was selected as the original point. Fig 9(f) showed that for pacemaker map Fig 9(d), the coordinates of the pacemaking cells was (1.5, 9.7) inside of the MEA.

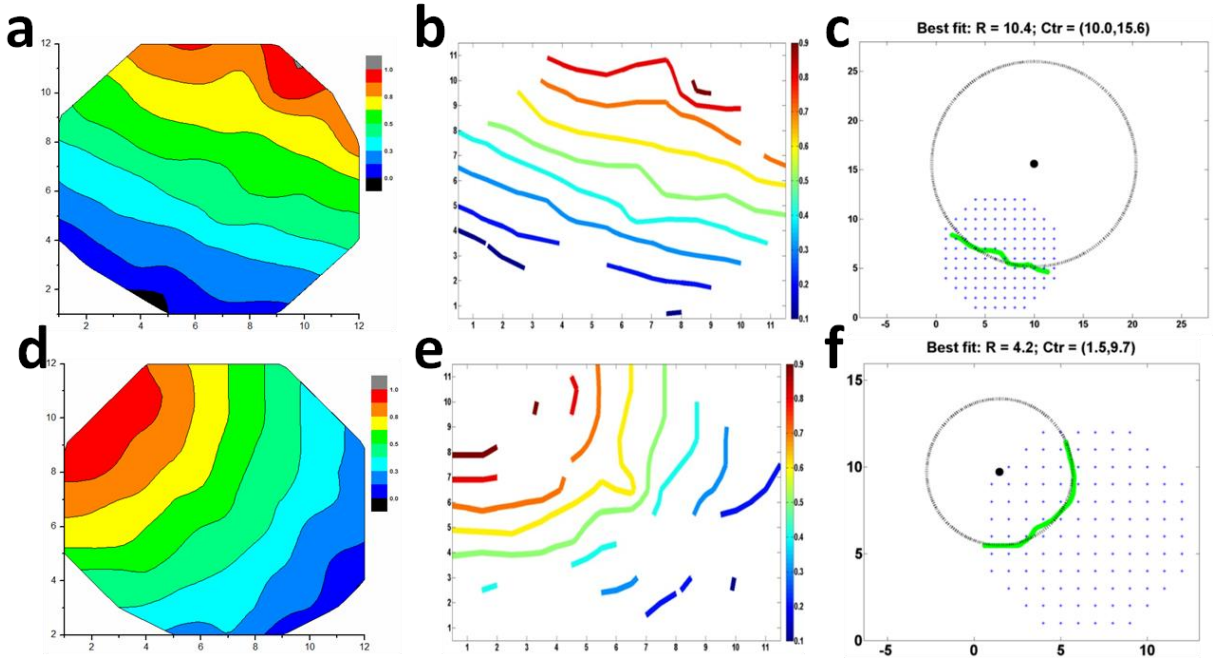

Fig 6. True pacemaker identification analysis in the 2D hESC-CM system at differentiation age of day 20 (a, b, c) and day 22 (d, e, f). (a) Representative contour plot of pacemaker in the 2D hESC-CM. (b) Contour graph of the propagation wave generated from the activation map. The circle wavelet was used to identify the center of propagation wave. (c) Center of the propagation wave was identified by fitting the wavelet with a circle. The origin of the circle represented the position of pacemaking cells. The pacemaking cells were located outside the MEA area. (d) – (f) Similar scheme of pacemaker identification as (a) – (c) at a cell stage of day 22. The pacemaking cells for this set were located inside the MEA area.

Conduction velocity

During the embryogenesis, cardiac conduction velocity increases as the heart maturates, with neonatal and adult cardiomyocytes show ~0.3m/s and ~1m/s, respectively. To examine whether conduction velocity increases during the maturation of hESC-CMs in our system, the conduction speed was calculated by analyzing the signal traveling distance and time lag. The conduction speed at day 18 (Fig 10) was around 35 mm/s. As the hESC-CMs maturate over days, conduction velocity increased up to around 120mm/s at day 28.

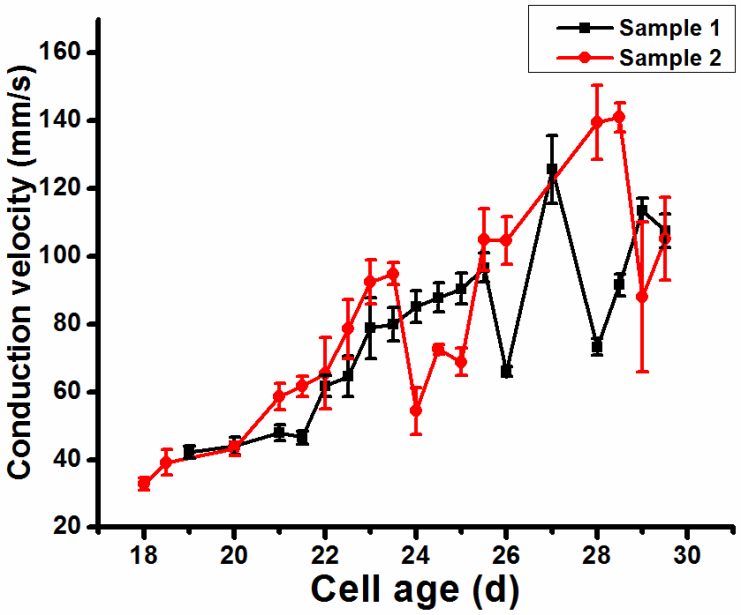

Fig 7. Conduction speed in the 2D cardiomyocytes system over 2 weeks recording. Sequential conduction speed of conduction speed in relationship with the cell age. An increased trend was observed consistently in two independent samples.

2.5 Discussions

We presented a model system that used monolayer hESC-CMs cultured on MEA platform. The system provided not only the common voltage-type signals from hESC-CM, but also allowed the study of position-dependent properties of electrical activities. The size of hESC-CM can be up to centimeter. The whole electrode array can monitor electrical signals over a 2.2mm*2.2mm area. This model system worked at full capacity and provided a coverage area which was much bigger compared with convention embryonic body method. This made it possible to study important position-dependent properties of hESC-CM such as pacemaking cells and conduction speed.

The electrophysiological properties of hESC-CM during the maturation process were studied. Beat interval was analyzed to quantify the collective behavior of hESC-CM over weeks. The beat interval of hESC-CM starting from cell age of day 18 to day 28 showed a steady period of around 10 days. The results from three independent tests were consistent. This could result from the limitations of 2D monolayer culture method. Considering one can plate hESC-CMs at different differentiation stage on the MEA, this 10-day window can allow full access to characterize the electrophysiological properties of hESC-CM at different stage. It is therefore possible to monitor the hESC-CM during early and late cardiogenesis[17], and provide insight into the process of maturation process.

Investigation of the activation time at each channel allowed us to rank the cells across the electrode array in order of beating time. The contour plot in Fig 3 showed the propagation. The planar propagation waveform suggested a point source. The shape of activation map at each day changed time to time, meaning the point source changed positions over 12 days. Since the size of hESC-CM was much larger compared with the size of electrode array, the point source could fall

outside of the electrode array. The pacemaking identification module overcame this limitation. The wavefront back fitting method could find out the coordinates of the pacemaking cells. The discovery of pacemaking cells allowed better understanding of the functionality and development of hESC-CM. We can concluded that there was only one pacemaking region in the system at a time because of the planar waveform and it was not stable, although the beat rate was very steady in the same time. This phenomenon is closely related to fact that during embryogenesis, the developing heart can stay operational while it is still rapidly proliferating and forming.

Conduction velocity is an important indicator of the maturity of cardiomyocytes. The limited access of MEA to cardiomyocytes using the traditional embryonic body culture method makes it very difficult to measure the conduction velocity. The high output 2D system is the first one to demonstrate the measurement of conduction speed in vitro. After the identification of the pacemaking cells, the conduction velocity was calculated in two directions and shown to be distance-independent. Fig 10 showed the conduction velocity was around 35 mm/s at cell age of day 18. Moreover, we observed an increasing conduction speed over time. This confirmed with the discovery that conduction velocity increased as the heart maturates in vivo.

2.6 Summary

In summary, the hybrid of monolayer culture of hESC-CMs and electrophysiological measurement on MEA provides a direct method to examine the spatiotemporal dynamics of the electromechanical maturation in human cardiomyocytes. The utility of MEA for the hESC/iPSC-CMs has been largely limited to the disease modeling and drug assessment[5, 26-33]. Monolayer culture method overcomes technical problems associated with recording of conventional three-dimensional cell embryoid bodies.Our system allows for monitoring electric signals over weeks from the cells in direct contact with electrodes, identify pacemaking cells, and perform computational analyses of localized voltage-type signal and position-dependent properties of electrical activities.Notably, accurate measurement of the spatiotemporal dynamics of electrophysiological parameters in this system allows the discovery of unique insights into the process of differentiation and cell maturation into a beating and coordinated layer: electrophysiological parameters associated with cardiomyocyte maturity are directly correlated with their distance from pacemaking cells. This suggests that spatial cue from the pacemaking cells play a key role in determining the functionality of the working cardiomyocytes.This accurate, real-time, and flexible method will set a new standard for electrophysiological analyses of hESC/iPSC-CMs with broad applicability in the stem cell biology.

2.7 References

1. Thomson, J.A. et al. Embryonic stem cell lines derived from human blastocysts. *Science* **282**, 1145-1147 (1998).

2. Suemori, H. et al. Efficient establishment of human embryonic stem cell lines and long-term maintenance with stable karyotype by enzymatic bulk passage. *Biochem Biophys Res Commun* **345**, 926-932 (2006).

3. Takahashi, K. et al. Induction of pluripotent stem cells from adult human fibroblasts by defined factors. *Cell* **131**, 861-872 (2007).

4. Yu, J. et al. Induced pluripotent stem cell lines derived from human somatic cells. *Science* **318**, 1917-1920 (2007).

5. Clements, M. & Thomas, N. High-throughput multi-parameter profiling of electrophysiological drug effects in human embryonic stem cell derived cardiomyocytes using multi-electrode arrays. *Toxicol Sci* **140**, 445-461 (2014).

6. Mummery, C. et al. Cardiomyocyte differentiation of mouse and human embryonic stem cells. *J Anat* **200**, 233-242 (2002).

7. Laflamme, M.A. et al. Cardiomyocytes derived from human embryonic stem cells in pro-survival factors enhance function of infarcted rat hearts. *Nat Biotechnol* **25**, 1015-1024 (2007).

8. Kattman, S.J. et al. Stage-specific optimization of activin/nodal and BMP signaling promotes cardiac differentiation of mouse and human pluripotent stem cell lines. *Cell Stem Cell* **8**, 228-240 (2011).

9. Willems, E. et al. Small-molecule inhibitors of the Wnt pathway potently promote cardiomyocytes from human embryonic stem cell-derived mesoderm. *Circ Res* **109**, 360-364 (2011).

10. Minami, I. et al. A small molecule that promotes cardiac differentiation of human pluripotent stem cells under defined, cytokine- and xeno-free conditions. *Cell Rep* **2**, 1448-1460 (2012).

11. Arshi, A. et al. Rigid microenvironments promote cardiac differentiation of mouse and human embryonic stem cells. *Sci Technol Adv Mater* **14** (2013).

12. Tulloch, N.L. et al. Growth of engineered human myocardium with mechanical loading and vascular coculture. *Circ Res* **109**, 47-59 (2011).

13. Lieu, D.K. et al. Mechanism-based facilitated maturation of human pluripotent stem cell-derived cardiomyocytes. *Circ Arrhythm Electrophysiol* **6**, 191-201 (2013).

14. Zhang, D. et al. Tissue-engineered cardiac patch for advanced functional maturation of human ESC-derived cardiomyocytes. *Biomaterials* **34**, 5813-5820 (2013).

15. Nunes, S.S. et al. Biowire: a platform for maturation of human pluripotent stem cell-derived cardiomyocytes. *Nat Methods* **10**, 781-787 (2013).

16. Feinberg, A.W. et al. Functional Differences in Engineered Myocardium from Embryonic Stem Cell-Derived versus Neonatal Cardiomyocytes. *Stem Cell Reports* **1**, 387-396 (2013).

17. Nakashima, Y. et al. Nkx2-5 suppresses the proliferation of atrial myocytes and conduction system. *Circ Res* **114**, 1103-1113 (2014).

18. Sartiani, L. et al. Developmental changes in cardiomyocytes differentiated from human embryonic stem cells: a molecular and electrophysiological approach. *Stem Cells* **25**, 1136-1144 (2007).

19. Lundy, S.D., Zhu, W.Z., Regnier, M. & Laflamme, M.A. Structural and Functional Maturation of Cardiomyocytes Derived from Human Pluripotent Stem Cells. *Stem Cells Dev* (2013).

20. Robertson, C., Tran, D.D. & George, S.C. Concise review: maturation phases of human pluripotent stem cell-derived cardiomyocytes. *Stem Cells* **31**, 829-837 (2013).

21. Yang, X., Pabon, L. & Murry, C.E. Engineering adolescence: maturation of human pluripotent stem cell-derived cardiomyocytes. *Circ Res* **114**, 511-523 (2014).

22. Engler, A.J. et al. Embryonic cardiomyocytes beat best on a matrix with heart-like elasticity: scar-like rigidity inhibits beating. *J Cell Sci* **121**, 3794-3802 (2008).

23. Bajaj, P., Tang, X., Saif, T.A. & Bashir, R. Stiffness of the substrate influences the phenotype of embryonic chicken cardiac myocytes. *J Biomed Mater Res A* **95**, 1261-1269 (2010).

24. Forte, G. et al. Substrate Stiffness Modulates Gene Expression and Phenotype in Neonatal Cardiomyocytes In Vitro. *Tissue Eng Part A* (2012).

25. Hazeltine, L.B. et al. Effects of substrate mechanics on contractility of cardiomyocytes generated from human pluripotent stem cells. *Int J Cell Biol* **2012**, 508294 (2012).

26. Asai, Y., Tada, M., Otsuji, T.G. & Nakatsuji, N. Combination of functional cardiomyocytes derived from human stem cells and a highly-efficient microelectrode array system: an ideal hybrid model assay for drug development. *Curr Stem Cell Res Ther* **5**, 227-232 (2010).

27. Caspi, O. et al. In vitro electrophysiological drug testing using human embryonic stem cell derived cardiomyocytes. *Stem Cells Dev* **18**, 161-172 (2009).

28. Egashira, T. et al. Disease characterization using LQTS-specific induced pluripotent stem cells. *Cardiovasc Res* **95**, 419-429 (2012).

29. Harding, S.E., Ali, N.N., Brito-Martins, M. & Gorelik, J. The human embryonic stem cell-derived cardiomyocyte as a pharmacological model. *Pharmacol Ther* **113**, 341-353 (2007).

30. van den Heuvel, N.H., van Veen, T.A., Lim, B. & Jonsson, M.K. Lessons from the heart: Mirroring electrophysiological characteristics during cardiac development to in vitro differentiation of stem cell derived cardiomyocytes. *J Mol Cell Cardiol* **67C**, 12-25 (2013).

31. Kujala, V.J. et al. Averaging in vitro cardiac field potential recordings obtained with microelectrode arrays. *Comput Methods Programs Biomed* **104**, 199-205 (2011).

32. Navarrete, E.G. et al. Screening drug-induced arrhythmia [corrected] using human induced pluripotent stem cell-derived cardiomyocytes and low-impedance microelectrode arrays. *Circulation* **128**, S3-13 (2013).

33. Otsuji, T.G. et al. Progressive maturation in contracting cardiomyocytes derived from human embryonic stem cells: Qualitative effects on electrophysiological responses to drugs. *Stem Cell Res* **4**, 201-213 (2010).

Chapter 3.

Overdrive Suppression of Mouse Stem Cell-derived Cardiomyocytes using Microelectrode Array

3.1 Abstract

We explore the effects of electrical stimulation over mouse stem cell-derived cardiomyocytes cultured with micro-electrode array in vitro. A sequential voltage pulse is applied to the cardiomyocytes through pre-selected group of electrodes. Long term effects of electrical stimulation are observed through sequential electrical pulses which last at least 10 minutes. The spontaneous field potential signals of the beating cardiomyocytes have stronger amplitude compared with the signals before the application of electrical stimulation. The interaction between spontaneous beating and external pacing signal is also studied. The spontaneous beatings of cardiomyocytes can be suppressed and tend to follow the external pacing signals with proper electrical stimulations. The research of electrical stimulation can potentially provides insight into the interaction between external electrical stimulation and development/differentiation of cardiomyocytes.

3.2 Introduction

The possibility that stem cell derived cardiomyocytes replace the damaged heart tissue is widely discussed and studied[1-4]. Despite many differentiation protocols have evolved over past years to produce large scale of cardiomyocytes, the maturity level of cardiomyocytes remains fetal type[5]. Lack of understanding of the differentiation and integration process of cardiomyocytes, notably with respect to electrical signaling, significantly hampers the development of stem cell based therapy.

There is increasing interest in exploring the effects of electrical stimulation over the differentiation of stem cell derived cardiomyocytes. People have shown that during fetal

development, electrical signals are present and may help guide stem cells toward a cardiomyocyte fate[6]. Electrical field stimulation over an eight-day period increased the amplitude of synchronous contractions in a tissue construct of cardiac cells[7]. Application of DC electric field for 90s over an embryoid body of murince ES cells produced double yield of beating EBs[6]. It has been shown electrical stimulation can enhance the expression of cardiac related genes[8-9]. Moreover, the mechanisms through which the replacement cardiomyocytes contribute to improving heart function remain unclear. Poor control on the integration mechanism and fate of implanted cells can potentially lead to serious complications such as teratoma formation or induced arrhythmia[10-11]. The integration process is complicated since the grafts are constantly under the influence of the host. Therefore, it is quite necessary to fully explore the consequences of external electrical signaling over the differentiation and integration of stem cell derived cardiomyocytes.

Currently the research is mainly involved with a model called embryonic body approach[12-14], which electrical stimulation is applied to embryonic body cell cluster through microelectrode. However, there are many limitations of the current experimental setup. Only the overall effects of the electrical stimulation are studied because of the size capacity. Real time information of the system response is lost since one cannot stimulate and monitor the system at the same time using the embryonic body approach.

Here, we present a long-term culture model of mouse cardiomyocyte confluent layer on microelectrode array in vitro. Mouse cardiomycytes are prepared based on a protocol previously described[15]. After further processes, a confluent layer of mouse cardiomyocytes is plated on various substrates for comprehensive characterizations. With cells cultured with Microelectrode Array (MEA) chip, this model makes full use of all the electrodes and provides spatial resolution

which is not typically available. Previously, we have shown how to characterize various electrical features during the differentiation process of human embryonic stem cells derived cardiomyocytes. Moreover, it allows us to explore the effects of electrical stimulation over cardiomyocytes with great flexibility. In the current experimental setup, the external electrical stimulation signals are programmable and can be applied to any selected group of electrodes of the MEA. With this new model, we can not only compare the spontaneous beating signals from stimulated cardiomyocytes and non-stimulated cardiomyocytes, but also we can acquire information about the real time response of the cardiomyocytes during the external electrical stimulation.

We first characterize the general effects of electrical stimulation over mouse cardiomyocytes. Intrinsic parameters representing the contraction motion of mouse cardiomycytes before the stimulation and after stimulation are analyzed. Results show that a phenomenon of electroporation happens during long term external stimulation. We further investigate the interaction between external pacing signal and the spontaneous beating signal. This could provide insight into the graft process which the new planted graft tissues are under the influence of existing host tissue. We observe a phenomenon called overdrive suppression. With proper setting of external pacing signal, the spontaneous beating of the stem cell cardiomyocytes can be suppressed and tends to follow the external signal.

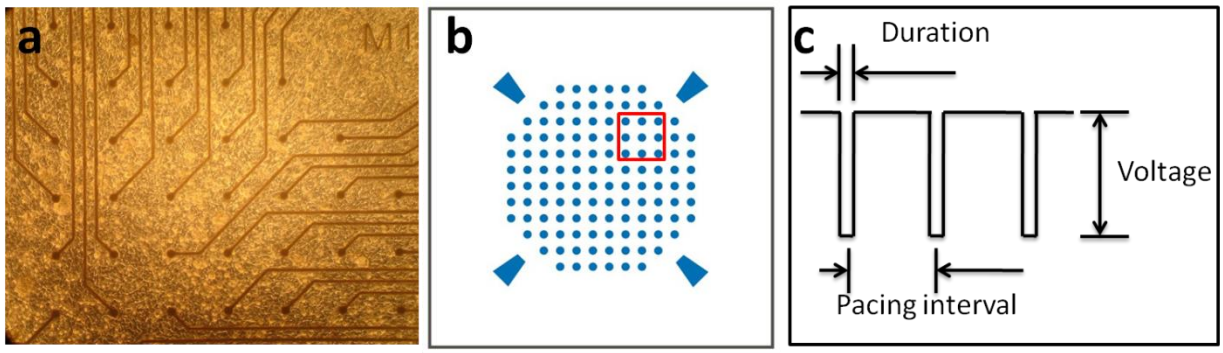

Fig 8. Schematic of the electrical stimulation on confluent layer of mouse stem cell derived cardiomyocytes using the MEA system. (a) Optical image of a confluent layer of mouse stem cell derived cardiomyocytes on top of microelectrode array. (b) Schematic of the 120 electrodes from the microelectrode array. Without electrical stimulation, the spontaneous beatings of cardiomyocytes are monitored from all the electrodes simultaneously. During electrical stimulation, the nine electrodes in the red box are selected as the working electrodes to apply external electrical stimulation in this case, while the rest electrodes could serve as monitoring electrodes at the same time. (c) The external electrical stimulation signal is programmable, and is determined by three parameters as shown in the graph. A negative mono-phase voltage sequence is adopted in the current experimental setup.

3.3 Methods:

Microelectrode array measurements

Mouse cardiomyocytes (differentiation day 2) are plated on uncoated, mocroelectrode array (MEA) containing 120 integrated TiN electrodes (30 µm diameter, 200 µm interelectrode spacing), as shown in Fig 1(a). The sample is cultured in an incubator with a temperature of 37 °C and 5% CO_2. Two days are given to allow the cardiomyocytes to well attach the MEA

surface and we start the electrical stimulation at the differentiation day 4. Using the MEA2100-HS120 system (Multichannel systems, Reutlingen, Germany), the spontaneous beating can be characterized through the monitoring of 120 electrodes simultaneously. The system also allows electrical stimulation through multifocal electrodes and real time monitor through unoccupied electrodes at the same time, as shown in Fig 1(b). Covered by a confluent layer of mouse cardiomyocytes, the MEA system applies sequential external voltage signals to cardiac cells in contact with the pre-selected microelectrodes. The rest electrodes would serve as monitoring electrodes.

In the current experimental setup, a negative monophase voltage sequence shown in Fig 1(c) is applied to a selected group of electrodes with tunable parameters (voltage amplitude is typically around -1.5 V, voltage duration 200 ~ 320 us, and pacing interval around 200 ms). The stimulation lasts for over 10 minutes for electroporation experiment, and about 2 minutes for overdrive suppression experiment. Local field potentials (LFPs) at each electrode are collected over a period of 20 minutes with a sampling rate of 1 KHz before and after the stimulation. Data analysis was carried out using the MC_DataTool (Multichannel Systems), Origin (OriginLab Corporation) and Matlab (MathWorks).

Data conversion

The raw data files acquired through the MEA2100-HS120 system are converted into ASCII files using the MC_DataTool. During the conversion, all 120 channels are selected from the channel configuration map following top to down, left to right order. The ASCII files contain 121 columns. The first column represents a sampling count column and the second column to the last column represent time serial field potential data collected from 120 channels in the same

order of electrodes being selected during the conversion. The local voltage features detected by each electrode can thus be extracted by analyzing the digital column data corresponding to that electrode.

Field potential analysis

When analyzing the dataset before and after the electrical stimulation, the digital signal collected from each electrode is a sequence of voltage spike, which corresponds to the spontaneous contraction motion of the cardiomyocytes. The quantitative analyses are mostly based on the information of field potential amplitude. We use the Matlab function 'findpeaks' to accurately determine the amplitude for all the active channels after loading the ASCII file into Matlab program. Tunable parameters included 'minpeakheight' and 'minpeakdistance'. We set the 'minpeakheight' as 16 μV, considering the noise level in the MEA system is ± 8μV which means a noticeable peak had a minimum signal-to-noise ratio of 4. The 'minpeakdistance' is set as 150ms, which is based on the experimental observation that mouse cardiomyocytes beat at a frequency around 5 Hz.

When analyzing the dataset during the electrical stimulation, the digital signal collected from each electrode is a combination of intrinsic sequence of voltage spike which corresponds to the spontaneous contraction motion of the cardiomyocytes, and the propagated external pacing voltage signal which has same frequency as we program for the external pacing signal. The qualitative and quantitative analyses are mostly based on the information of beat interval. We used Matlab to plot the signal to identify the relationship between the external pacing signal and intrinsic beating signal.

3.4 Results

Electroporation induced by continuous electrical stimulation

Spontaneous and rhythmic mechanical contractions were observed under optical microscope and the field potentials of cardiomyocytes could be detected with the MEA system. After delivering a train of monophase negative electrical pulses (-1.5v voltage amplitude, 200us voltage duration for each pulse, and last in 10 minutes) to the mouse cardiomyocytes, the microelectrode array gained electrical access to the cell interior by local electroporation. Once switched back into recording mode, the electrodes that were used as the stimulated ones recorded up to 60 uV of rhythmic intracellular action potentials (Fig 2a), which were 3 times larger compared with the field potential signals before the electrical stimulation. The beating interval remained unchanged before and after electroporation. Electrical stimulation on various group of electrodes confirmed the phenomenon.

Electroporation induced access to cell interior is transient because of the spontaneous cell membrane resealing[16-17]. The amplitude of recorded action potentials decayed quickly in scale of a minute, as shown in Fig 2(c). The lifetime of intracellular access is around 20s if we define it as the time when the amplitude decays to half of its initial amplitude.

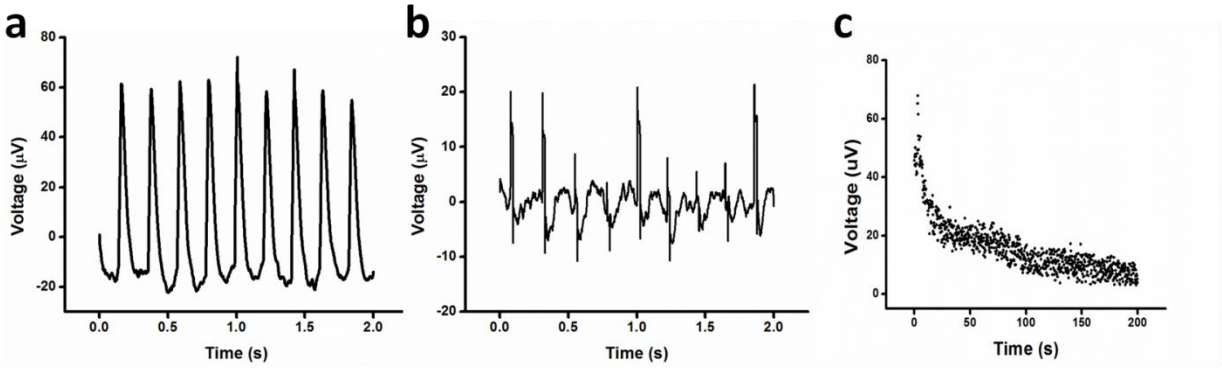

Fig 9. Intracellular access through continuous electrical stimulation. (a) Right after local electroporation, intracellular recording of action potentials in mouse cardiomyocytes was achieved. (b) After cell resealing, the action potentials in mouse cardiomyocytes returned back to extracellular recording of field potentials. (c) Time plot of recorded action potentials for the first 200s after electroporation.

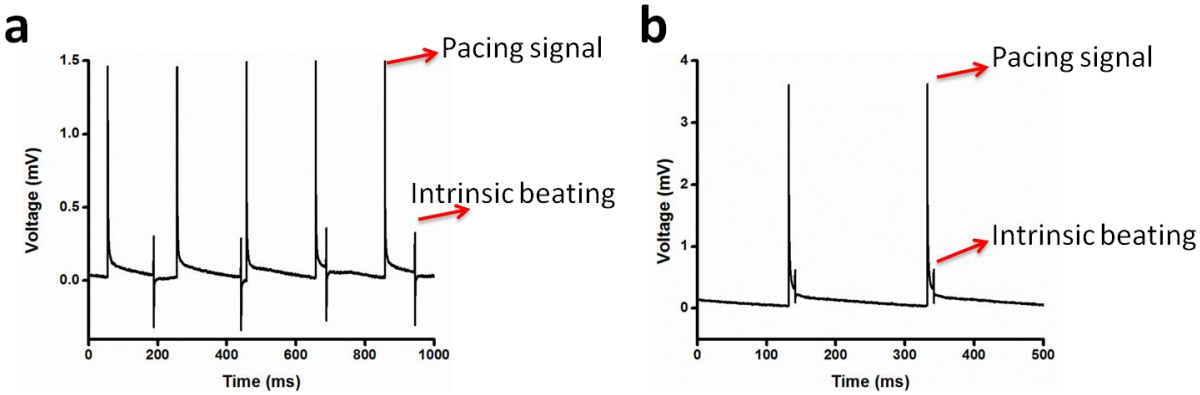

Fig 10. Schematic of the interaction between intrinsic beating signal and external pacing signal. (a) When the external pacing signal has no direct interaction with intrinsic beating. Their beating frequencies are independent. (b) When the external pacing signal has direct interaction with the intrinsic beating. The intrinsic beating of cardiomyocytes is suppressed, and is triggered by the external pacing signal.

Overdrive suppression discussion

Naturally, a phenomenon called overdrive suppression has been studied for multiple decades[18-21]. The primary pacemaker site within the heart is the sinoatrial (SA) node; other cells have pacemaker activity (automaticity) or have the capacity of becoming pacemakers. The higher frequency of SA nodal firing suppresses other pacemaker sites. In cased of heart malfunction or damages, an artificial pacemaker may be used to provide an external pulse to control and synchronize the body's intrinsic conduction system. We further investigate the interaction of external pacing signal and the spontaneous beating signal in vitro. This could provide insight into the graft process which the new planted graft tissues are under the influence of existing host tissue.

A train of monophase negative electrical pulses were delivered to mouse cardiomyocytes at cell differentiation state of day 4. Both intrinsic rhythmic beating signal and the external pacing signal were detected through the MEA measurements (Fig 3). When there is no direct interaction between the intrinsic beating signal and the external pacing signal, the cardiomyocytes beat at their spontaneous pace without receiving any obvious influence from the external pacing signal (Fig 3a). The calculated intrinsic beating frequency during the external pacing remains the same as the intrinsic beating frequency before the external pacing. However, under proper external pacing, there is a direct interaction between the intrinsic beating signal and the external pacing signal. The intrinsic beating of cardiomyocytes is suppressed, and is triggered by the external pacing signal (Fig 3b). The calculated intrinsic beating frequency during the external pacing is now not the same as the intrinsic beating frequency before the external pacing. The cardiomyocytes has a new beating frequency the same as the external pacing signal. For

example, the cardiomyocytes with an intrinsic beating interval of 243 ms was stimulated by sequential electric pulses (-1.5 V voltage amplitude, 200 us voltage duration for each pulse, and pacing interval of 200 ms), the overdrive suppression was observed. The intrinsic beating interval changed to 200 ms following the external pacing signal, as shown in Fig 3(b).

a

Pacing voltage	Pacing status
-1V	No
-1.25V	No
-1.5V	Yes
-1.75V	Yes

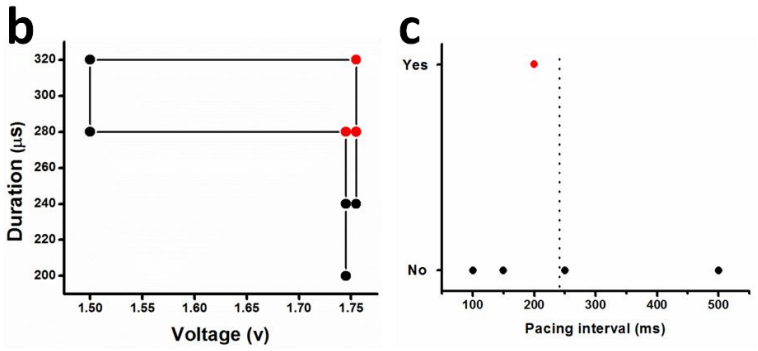

Fig 11. Suitable parameters including voltage amplitude, voltage duration, and pacing interval of external electrical pulses to trigger the overdrive suppression. The intrinsic beating of cardiomyocytes has a beat interval of 243 ms. (a) The pacing interval and voltage duration is set to be 200 ms and 200 us, respectively. External pacing signal has a voltage threshold of -1.5 V. Voltage below -1.5 V (-1V, -1.25V in this case) does not trigger the overdrive suppression, while voltage above -1.5V (-1.5V and -1.75V) triggers the overdrive suppression. (b)The pacing interval is set to be 200 ms. Red dots (with voltage duration no less than 200 us, voltage no less than -1.75 V) represent the suitable combination of voltage duration and voltage in order to trigger the overdrive suppression. (c) The pacing voltage and duration is set to be -1.5 V and 200 us, respectively. Only when the pacing interval is 200 ms, slightly smaller than the intrinsic beating interval of 243 ms, the external pacing signal triggers the overdrive suppression.

Tunable electrical parameters to induce overdrive suppression

Not all external electrical pulses could trigger the overdrive suppression. We further explored the suitable parameters for the external pacing signal that could suppress the intrinsic beating of cardiomyocytes. There are three parameters determining the sequential electrical pulses such as voltage amplitude, voltage duration and pacing interval, as shown in Fig 1(c). A hypothesis that a stronger external pacing signal tends to have a larger impact over the spontaneous contraction motion of cardiomyocytes was tested.

The rhythmic contraction motion of cardiomyocytes was characterized before applying the electrical stimulation. The intrinsic beating motion had a beating interval of 243 ms (with a beating frequency slightly higher than 4 Hz). We first tested the influence of pacing voltage, with a fixed pacing interval and voltage duration of 200 ms and 200 us, respectively. The pacing voltage ranged among -1 V, -1.25 V, -1.5 V and -1.75 V. External pacing signal with a strong voltage (-1.5 V and -1.75 V) suppressed the original intrinsic beating of cardiomyocytes, and the cardiomyocytes beated with an interval of 200 ms which was the same as the pacing signal. External pacing signal with a small voltage (-1 V and -1.25 V) did not have any obvious effect in changing the beat frequency of cardiomyocytes as shown in Fig 4(a). Furthermore, we tested the combination effect of pacing voltage amplitude and voltage duration, representing the length and strength of the external pacing. The pacing interval was set as 200 ms, slightly faster than the intrinsic beating. The voltage duration ranged among 200 us, 240 us, 280 us and 320 us, while the voltage amplitude ranged between -1.5 V and -1.75 V. Fig 4(b) showed that only when the external voltage and voltage duration were strong and long enough, it would trigger the overdrive suppression. Red dots located at the right top corner of the graph (-1.75 V and 280 us, -1.75 V and 320 us) represented the suitable combination. Finally we tested the appropriate

pacing interval. The voltage amplitude and voltage duration were set as -1.5 V and 200 us. The pacing interval ranged among 100 ms, 150 ms, 200 ms, 250 ms and 500 ms. Only when the pacing frequency was slightly faster than the intrinsic beating frequency, the overdrive suppression was triggered. Sequential electrical pulses with beat interval of 200 ms (red dot, Fig 4c) suppressed the initial spontaneous beating with beat interval of 243 ms. External pacing signal with a much faster frequency or slower frequency than 200 ms (i.e. 5 Hz) did not trigger the overdrive suppression as shown in Fig 4(c).

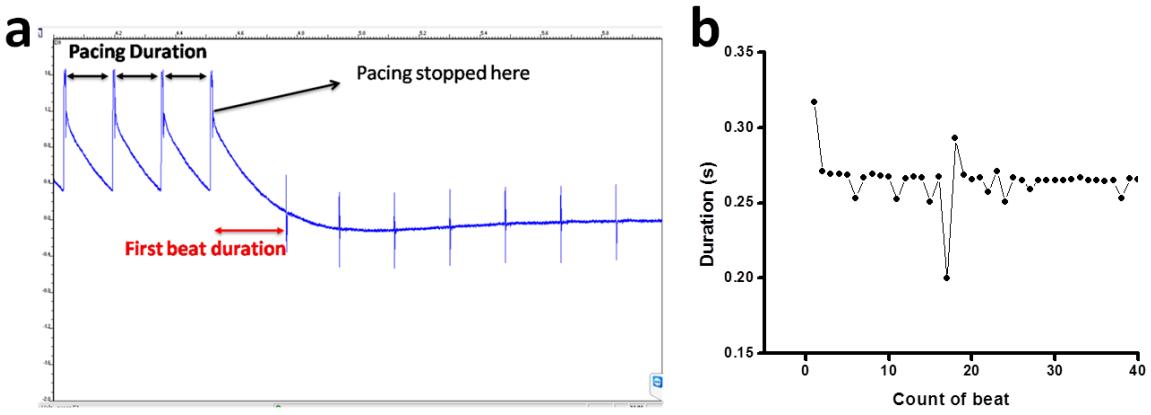

Fig 12. Schematic of recovery time of intrinsic beating after the overdrive suppression is stopped. (a) The overdrive suppression phenomenon is showed at the beginning of the graph, which the intrinsic beating of cardiomyocytes follows the external pacing signals. The intrinsic beating of cardiomyocytes recovered after the external pacing is stopped. (b) The recovery time is defined as the first beat interval right after the external pacing is stopped. The recovery time is generally much longer compared with the intrinsic beating interval of cardiomyocytes, showing the system takes longer to recover from the external stimulation.

Recovery time

Under overdrive suppression, the intrinsic beating of cardiomyocytes is suppressed by external pacing signal. An interesting question is how the cardiomyocytes would behave after the external stimulation stops. Whether the cardiomyocytes would continue to beat at the same frequency of the pacing signal, or they would recover from the external stimulation and pick up the intrinsic beating rate, or something totally unexpected. The time it takes for the cardiomyocytes to contract for the first time after stopping the external pacing signal is defined as recovery time. It represents how soon the system re-initializes the contraction motion without the external leading signal. The recovery time is more and more frequently used to quantify the robustness of the system. The shorter the recovery time, the more robust the system is.

After applying proper external electrical stimulation to the cardiomyocytes, overdrive suppression status is achieved. The MEA system allows visually monitoring the co-existence between the intrinsic beating signal and the external pacing signal. The external pacing sequence was then stopped while the local field potential signal was being recorded without stopping. Fig 5(a) shows that the overdrive suppression phenomenon is observed at the beginning, while the spontaneous beating of cardiomyocytes shows up after the external electrical stimulation is stopped. We measured the recovery time and it turned out that the recovery time was generally much longer than the spontaneous beating interval of cardiomyocytes as shown in Fig 5(b). The results confirm that the cardiomyocytes system takes time to realize that there is no external pace leader, thus it generally takes much longer than a normal beat interval for the cardiomyocytes system to re-initialize the contraction motion.

3.5 Discussions

We have shown that external electrical stimulation has an impact on the electrical signaling of mouse cardiomyocytes. The combination of confluent layer of cardiomyocytes and the microelectrode array system allows a very flexible and powerful way to investigate the interaction between electrical signaling of intrinsic beating and external pacing. Long term electrical stimulation could possibly provide electrical access to the cell interior by generating holes through the cell membrane. Field potential amplitude serves as a sensitive marker to monitor the effects. The process is reversible since the field potential amplitude drops back to normal value after the cell membrane heals in a few minutes. Further test could be done to fully characterize the morphology change under electrical stimulation using Electron microscope (EM) or fluorescence labeling. Short term electrical stimulation with proper parameters is able to suppress the intrinsic beating pace of cardiomyoyctes and lead the beating rhythm. We have shown detailed investigation of necessary parameters for the external pacing signal in order to trigger the so called overdrive suppression phenomena. Generally a strong external pacing signal with a slightly faster pace than the intrinsic beating frequency of the cardiomyocytes is needed. The recovery time after the external stimulation is stopped could be potentially used to characterize the systematic properties of cardiomyocytes such as aging, robustness and so on.

3.6 References

1. Tsang, S.Y., *Embryonic stem cell-derived cardiomyocytes for therapy: how close are we?* International Journal of Cardiology, 2008. **125**: p. S26-S26.
2. Gallo, P., C.S. Peschle, and G. Condorelli, *Sources of cardiomyocytes for stem cell therapy: An update.* Pediatric Research, 2006. **59**(4): p. 79r-83r.
3. Ban, K., et al., *Cell Therapy with Embryonic Stem Cell-Derived Cardiomyocytes Encapsulated in Injectable Nanomatrix Gel Enhances Cell Engraftment and Promotes Cardiac Repair.* Acs Nano, 2014. **8**(10): p. 10815-10825.
4. Serena, E., et al., *An in vitro model for cardiac cell therapy: coupling a microfluidic platform with arrayed human embryonic stem cells-derived cardiomyocytes for screening pathological conditions.* Cardiovascular Research, 2010. **87**: p. S110-S110.
5. Feinberg, A.W., et al., *Functional Differences in Engineered Myocardium from Embryonic Stem Cell-Derived versus Neonatal Cardiomyocytes.* Stem Cell Reports, 2013. **1**(5): p. 387-396.
6. Sauer, H., et al., *Effects of electrical fields on cardiomyocyte differentiation of embryonic stem cells.* Journal of Cellular Biochemistry, 1999. **75**(4): p. 710-723.
7. Radisic, M., et al., *Functional assembly of engineered myocardium by electrical stimulation of cardiac myocytes cultured on scaffolds.* Proceedings of the National Academy of Sciences of the United States of America, 2004. **101**(52): p. 18129-18134.
8. Xia, Y., et al., *Electrical stimulation of neonatal cardiac myocytes activates the NFAT3 and GATA4 pathways and up-regulates the adenylosuccinate synthetase 1 gene.* Journal of Biological Chemistry, 2000. **275**(3): p. 1855-1863.

9. Xia, Y., L.M. Buja, and J.B. McMillin, *Activation of the cytochrome c gene by electrical stimulation in neonatal rat cardiac myocytes - Role of NRF-1 and c-Jun.* Journal of Biological Chemistry, 1998. **273**(20): p. 12593-12598.

10. Lees, J.G., et al., *In vitro and in vivo differentiation of hESC on PLGA scaffolds and the incidence of teratoma formation.* Cytometry Part A, 2006. **69A**(5): p. 401-401.

11. Chang, M.G., et al., *Proarrhythmic potential of mesenchymal stem cell transplantation revealed in an in vitro coculture model.* Circulation, 2006. **113**(15): p. 1832-1841.

12. Bratt-Leal, A.M., R.L. Carpenedo, and T.C. McDevitt, *Engineering the Embryoid Body Microenvironment to Direct Embryonic Stem Cell Differentiation.* Biotechnology Progress, 2009. **25**(1): p. 43-51.

13. Greenhough, S., et al., *Development of an Embryoid Body-Based Screening Strategy for Assessing the Hepatocyte Differentiation Potential of Human Embryonic Stem Cells Following Single-Cell Dissociation.* Cellular Reprogramming, 2013. **15**(1): p. 9-14.

14. Kinney, M.A., R. Saeed, and T.C. McDevitt, *Systematic analysis of embryonic stem cell differentiation in hydrodynamic environments with controlled embryoid body size.* Integrative Biology, 2012. **4**(6): p. 641-650.

15. Minami, I., et al., *A Small Molecule that Promotes Cardiac Differentiation of Human Pluripotent Stem Cells under Defined, Cytokine- and Xeno-free Conditions.* Cell Reports, 2012. **2**(5): p. 1448-1460.

16. Gehl, J., *Electroporation: theory and methods, perspectives for drug delivery, gene therapy and research.* Acta Physiologica Scandinavica, 2003. **177**(4): p. 437-447.

17. Tovar, O. and L. Tung, *Electroporation and Recovery of Cardiac Cell-Membrane with Rectangular Voltage Pulses.* American Journal of Physiology, 1992. **263**(4): p. H1128-H1135.

18. Vassalle, M., *Relationship among Cardiac-Pacemakers - Overdrive Suppression.* Circulation Research, 1977. **41**(3): p. 269-277.

19. Kato, T., et al., *Relationships between Spontaneous Cardiac-Arrest and Induced Cardiac-Arrest by Overdrive Suppression Test in Sick Sinus Syndrome.* Japanese Circulation Journal-English Edition, 1977. **41**(7): p. 752-752.

20. Batrouni, M., *Overdrive Suppression Design Pattern.* Cooperative Design, Visualization, and Engineering, Cdve 2014, 2014. **8683**: p. 103-110.

21. Graziani, A.T. and M. Vassalle, *Mechanisms underlying overdrive suppression and overdrive excitation in guinea pig sino-atrial node.* Journal of Biomedical Science, 2006. **13**(5): p. 703-720.

Chapter 4.

Spatial Nanomechanical Profiling of Metastatic Breast Cancer Cells and Applications in Treatment with Nanodiamond/Nanoplatinum Solution (DPV576)

4.1 Abstract

Investigation of the mechanical properties of cancer cells, such as Young's modulus, provides insights into the biophysical characteristics of cancer metastasis. The traditional method of measuring stiffness of single cancer cells using Atomic Force Microscopy (AFM) assumes that a cell is a homogenous entity. Such an assumption disregards the fact that different cellular regions have localized properties and gives an incomplete understanding of cell mechanics. In the current study, we sought to identify the nanomechanical changes present at different cellular regions (cell nuclear and lamellipodial of live murine metastatic breast cancer cells (4T1) using AFM indentation. Moreover, by using customized MATLAB routines, we explored regional cell stiffness at varying indentation depths, breakthrough events, cellular plasticity and cell adhesion. Complementary to the quantified mechanical measurements using single force indentation curves, we obtained AFM Peak Force images of live 4T1 cells to spatially map and compare the topography, stiffness, deformation and adhesion parameters of 4T1 cells. We discuss and propose the applications of modified single cell mechanics data analysis in combination with topographic cellular and sub-cellular characteristics to better understand the overall biophysical characteristics of metastatic cancer cells. The proposed analysis module is applied to studying nanomechanical changes in 4T1 cells post exposure to a nanodiamond/nanoplatinum mixture dispersed in aqueous solution (DPV576). This study demonstrates the changes in cell stiffness and tracks early structural alterations of metastatic breast cancer cells post treatment with DPV576, which may have important implications in the role of nanodiamond/nanoplatinum based cancer cell therapy and sensitization to chemotherapy drugs.

4.2 Introduction

Breast cancer has been ranked as the second most common type of cancer and the deadliest, claiming the lives of 39,620 in the United States annually, with 232,340 new cases estimated in 2013 alone (National Cancer Institute, National Institutes of Health 2013). It has been reported that metastasis is responsible for 90% of the deaths in breast cancer patients[1]. Much of the research conducted has been proteomic and genomic in nature[2]. Many pathways and factors are involved in breast cancer metastasis, indicating the complexity of this condition. As such, significant attention has been given to investigating the nuclear aspects of metastasis, including identification of potential cancer biomarkers[2], modification of various transcription factors[3-4]and over-expression of known tumor-suppressor genes[5].

Biomechanics and the biophysical properties of cells have recently gained increased importance. Young's modulus, a quantitative indicator of material stiffness, has been newly recognized as a cellular phenotypic characteristic associated with cancer cells[6-8] . It is understood that cancer not only causes functional and biological alterations in cells but also results in significant changes in their physical, structural and morphological characteristics[9]. Dynamic rearrangements in the actin cytoskeleton are common to all forms of cancer[9]. Several studies have shown that cancerous cells have a lower average Young's modulus than that of normal cells[7, 10-11]. However, the inhomogeneous structure of cells[12] requires a spatial approach which differentiates both the local structure at different regions of cells and the subsurface structure of cells at varying depths. People have studied the local mechanical properties of cells such as cell body, lamellipodium and leading edge[13-15]. It has also been reported that cell regions at varying depths show distinct stiffness revealing cytoskeleton organization[16-18]. However, the substrate effect[19] over measurements of cell stiffness

especially in lamellipodial region limits the accuracy of results. Therefore, a thoroughly cellular mechanical study overcoming the substrate effect and exploration of the correlation between biophysical properties and distinct structural regions of the cell is needed to elucidate the role of mechanics in both metastatic cell migration and proliferation.

In order to conduct such a comprehensive study of cell mechanics, it is imperative to acknowledge to role that the cytoskeletal network plays in metastasis[20]. Of particular interest are the structural alterations of lamellipodia, a web-like projection on the motile side of the cell that is composed of a two dimensional actin network[21]. After attaching to a new adhesion site, actin filament (F-actin) subunits accumulate at the specific region to form a microspike, a miniature protrusion that initiates the forward movement of the cell. Actin subunits continue to polymerize at this microspike, forming a filopodia, a longer finger-like projection which will then bind to another adhesion site at a distant location[22]. The process of actin polymerization in lamellipodia allows cells to undergo a unique shift from an epithelial type to a less differentiated type. This step is known as the epithelial to mesenchymal transition (EMT), a major stage in the initiation of adverse diseases such as organ fibrosis and cancer metastasis[23-24]. Understanding the dynamics of these cytoskeletal structures compared to the nuclear region allows us to formulate a more holistic cellular model.

We performed AFM (atomic force microscopy) based nanomechanical analysis on live, metastatic, murine breast cancer cells (4T1) as a model to explore the variations in localized mechanical properties of cells at varying indentation depths. We detected differences in cell stiffness of the central nuclear region of the 4T1 cells and their lamellipodia extensions. The quantified mechanical measurements were complemented with Peak Force Quantitative Nanomechanical property Mapping (QNM) mapping. Correlative AFM-based cell

nanomechanical profiling, cell morphology and topographic stiffness maps from Peak Force AFM provided an improved and integrative understanding of the structure and mechanics of metastatic 4T1 cells at the nanoscale level.

Furthermore, Nanoparticles have recently gained increased attention as drug delivery systems for the treatment of cancer due to their minute size, unique chemical properties, and low cytotoxicity. Studies by Schrand *et al.* reported that NDs are non-toxic in various different cell types and did not cause significant reactive oxygen species [25]. Moreover, NDs instilled intratracheally showed no significant adverse effects in the lungs of mice [26]. Although much work has been done with NDs, biophysical analysis and morphological changes at the single cell level, which are important in understanding the dynamics of metastasis, are lacking. It is understood that metastasis also causes significant changes in the biological, structural and physical characteristics of cells [9].Actin rearrangement within the cytoskeletal organization is common to cancer cells. Understanding the role that the cytoskeletal network plays in metastasis requires a thorough analysis of actin dynamics[27]. The process of actin polymerization is integral in the metastatic steps of intravasation, migration and extravasation[28]. Of particular interest are filopodial, finger-like projections on the motile side of the cell comprised of an actin network. In order to understand the mechanical aspects of the ND- mediated changes in cancer cells at the single cell level, we studied the dose dependent effects of DPV576 on the stiffness and morphology of live murine metastatic breast cancer cells.

4.3 Methods

Chemicals: RPMI 1640, FBS, L-Glutamine, Penicillin G, Streptomycin Sulfate, Dulbecco's PBS, and trypsin-EDTA were purchased from Gemini-Bio Products. A mixture of ND and NP solution known as DPV576 was used with particle size, shape, and composition as previously described [29]. DPV576 was supplied by Venex Co, Ltd, Kanagawa, Japan.

SEM/AFM imaging of DPV576: DPV576 particle aqueous solution imaged by SEM at 100,000x magnification shows aggregation (Fig.5). AFM images of aqueous solution of DPV576 were obtained over mica substrates using Dimension Icon (Bruker, CA, USA) under tapping mode in air using TESPW tips (Bruker, CA, USA).

Murine Breast Cancer Cell Line: 4T1 cells, purchased from the American Tissue Culture Collection (ATCC) Manassas, VA, USA, were cultured in RPMI 1640 supplemented with 10% heat inactivated FBS, 2mmol L-Glutamine, 100units/mL Penicillin G, and 100 mcg/mL Streptomycin Sulfate. Cells were incubated at 37°C and 5% carbon dioxide. At approximately 80% confluency, cells were washed with PBS and passaged using 0.25% trypsin-EDTA treatment for dissociation.

DPV576 Treatment: 4T1 cells were cultured in two flasks and divided into a total of eight petri dishes. Cells were exposed to 0, 5, 10, 15% ND/NP solution (in duplicate) and were allowed to incubate for two hours. Subsequently, petri dishes were removed from incubator and used for AFM measurements.

AFM Measurements: All measurements were conducted using a Catalyst atomic force microscope (Bruker Instruments, Santa Barbara, California) with a combined inverted optical/confocal microscope (Zeiss, Corp, Thornwood, New York). This combination permits

lateral positioning of the AFM tip over the cell center with submicron precision. AFM mechanical measurements were collected in contact mode using sharpened silicon nitride cantilevers with experimentally determined spring constants of 0.02N/m and a tip radius of <20 nm. Mechanical measurements were obtained at 37°C with force measurements recorded at a pulling rate of 1Hz. AFM measurements were obtained in at least 30 cells in one experiment. The AFM tip was always precisely positioned (within micron range) on top of the cell nuclear regions using motorized stage and inverted optical view of the combined confocal-AFM microscope.

AFM Imaging of cellular extensions: 4T1 cells were incubated with 15% DPV576 for one hour after which cells were fixed with 2% paraformaldehyde in PBS and imaged in PBS using Silicon-nitride probes with spring constants of 0.02N/m.

Time Lapse Optical Light Microscopy: Images were acquired using a Catalyst atomic force microscope (Bruker Instruments, Santa Barbara, California) with a combined inverted optical/confocal microscope (Zeiss, Corp, Thornwood, New York). A 4T1 cell suspension was dispensed into petri dishes and incubated overnight to allow for cell adherence. After washing with RPMI-1640 complete media, suspended ND/NP were added at 5, 10, 15% (v/v) concentrations in duplicate. Following 2 hours of incubation, the cells were observed and recorded at 20X magnification.

Peak Force AFM: Dimension Icon scanning probe microscope (Bruker Instruments, Santa Barbara, California) was used for peak force images. Measurements were taken using a MSNL (Sharp Microlever Silicon Nitride) tip with a spring constant of 0.0288 N/m and a sensitivity of 28.1 nm/V. The temperature of the sample was maintained at 37°C.

Statistical Analysis: Statistical significance for cell stiffness was determined by using Student's t-test. Differences were considered significant at the $p<0.05$ level.

AFM indentation theory: The mechanical properties of linear, isotropic, and elastic materials can be described by two intrinsic parameters, the Young's modulus E and the Poisson's ratio v. The indentation experiments with AFM are performed to characterize the mechanical properties of biological samples, especially cells in physiological conditions. The collected data are in the form of F = f (z) where F represents force executed by the cantilever, and z is the piezo-actuator translation. The piezo translation distance Δz equals the sum of the cantilever deflection Δd and the sample indentation δ,

$$\Delta z = \Delta d + \delta, \tag{1}$$

With a conical tip, the indentation depth and the applied force are connected through the Sneddon'smodel[30]:

$$F = \frac{2}{\pi} \cdot \tan\alpha \cdot \frac{E}{1-v^2} \cdot \delta^2, \tag{2}$$

where F is the applied force, δ is indentation, α is the half-opening angle of the cone, E is the Young's modulus of the sample, and v is the Poisson's ratio (v = 0.499, assuming the cell to be an incompressible solid[31]). To avoid the effects of the substrate over the stiffness measurements, only a small indentation which is less than 10% of the thickness of the sample was considered for the Sneddon's model.

For a thin sample, the small indentation will not hold, because indentations more than 400nm are required to correctly determine the contact point[32]. Therefore the measurements are limited to the central area of the cell. In order to investigate a thin sample including the cell periphery, a modified Sneddon's model[33] that accounts for the substrate effect is used:

$$F = \frac{8E \tan\alpha \cdot \delta^2}{3\pi} \cdot \left\{1 + 1.7795 \cdot \frac{2\tan\alpha}{\pi^2} \cdot \frac{\delta}{h} + 16 \cdot 1.7795^2 \cdot (\tan\alpha)^2 \cdot \frac{\delta^2}{h^2} + O\left(\frac{\delta^3}{h^3}\right)\right\}, \quad (3)$$

In the bottom effect cone correction (BECC) formula Eqn (3), h is the height of the sample at the specified location.

Data analysis: A statistically reliable force spectroscopy experiment consists typically of hundreds of force-distance curves. Thus a stable procedure to detect and process an extended data set is essential. We developed MATLAB (Mathworks) based routines for the analysis of force-distance curves. The customized program fulfills functions such as fitting the force-indentation data with appropriate Sneddon's model and acquiring stiffness at varying indentation depth.

The contact point is first determined over a 4 um ramp in all force-distance curves. The apparent loading force deviated from the baseline and started to increase once the tip indented into the sample (Fig. 1B). Linear fitting was applied to the first 1um in the force-distance curve, and the R^2 regression was recorded. The same process of linear fitting was done at small increases of 40 nm. The contact point was chosen when the R^2 regression was twice as large as the value in the first 1um. The acquired contact point was plotted in the same graph with the Force-separation curve, allowing one to adjust the threshold parameters based on performance.

Subsequently, force-indentation data was converted from the Force-separation data based on Eqn (1). Young's moduli were fitted through the least square method with Sneddon's model or a modified Sneddon's model (R^2 regression of 0.9). Stiffness at varying indentation depths was further determined by repeatedly increasing the fitting range by 100nm starting from the contact point.

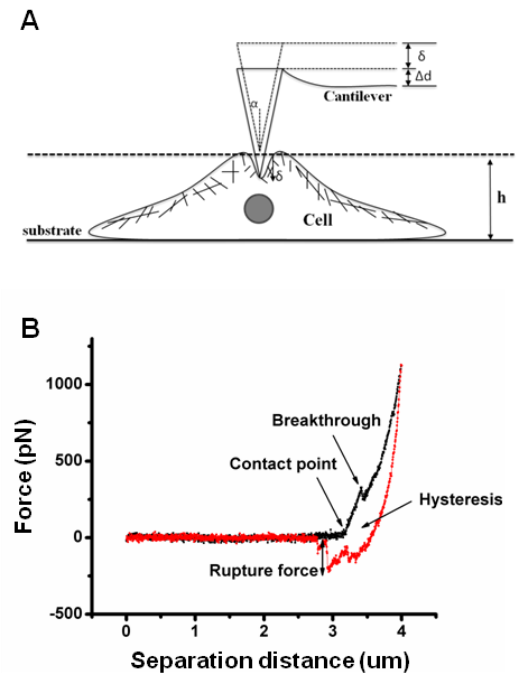

Fig. 1 (A) Schematic of the AFM indentation experiment above a cell with a conical tip (B) A sample Force-separation curve with various features was shown. The contact point was defined when the curve started to deviate from the baseline in the approach region (black curve) of the Force-separation curve. Discontinuity behavior (breakthrough) was observed at varying separation distances from the contact point in the approach region (black curve) of the Force-separation curve. Hysteresis was expressed by the area between approach and retract regions starting from the point of contact of the Force-separation curve. Rupture force was quantified as the magnitude of rupture event shown in the retract region (red curve) of the Force-separation curve.

4.4 Results

4.4.1 Nanomechanical analysis on live, metastatic, murine breast cancer cells (4T1)

Measurement of average Young's Modulus (E, KPa) values for cell nuclear and lamellipodial regions

The structure of the cytoskeleton varies across the cell body. Among such distinct structures, lamellipodia, a web-like actin network is located in the cell lamellipodial region[34]. The stiffness of cell is dependent on these distinct surface regions. Differentiation of the surface structural regions provides a better understanding of cell mechanics. The Sneddon's model[30, 32] is often used to measure the stiffness of a single cell in cell central region with AFM indentation. However, the substrate effect in the lamellipodial region (cell height was 2um in this case, showed in Fig. 1A) limits the application the model. Here, spatial differences in cell stiffness of the central nuclear region of the 4T1 cells and their lamellipodia extensions were investigated by using the Sneddon's model and the thin layer model[33], respectively. AFM force indentation experiments were carried out over the central region and lamellipodial region of 4T1 cells with a conical tip. The Young's modulus E was quantified with the appropriate Sneddon's model. The Young's modulus of 4T1 cell nucleus displayed a bimodal distribution with two main peaks. E values (Mean ± SEM) for the 4T1 cell nucleus were 1.63 ± 0.09 KPa and 4.04 ± 0.17KPa, respectively. The Young's modulus of 4T1 cell lamellipodial region also displayed a bimodal distribution but higher cell stiffness. E values (Mean ± SEM) for the cell edge were 1.79 ± 0.07 KPa and 5.63 ± 0.07 KPa, respectively. Fig. 2 displays individual cell stiffness profiles for the cell nuclear and lamellipodial regions. The average Young's modules of cell lamellipodial region were generally higher than those of cell nucleus, which agreed with the stiffness distribution graph.

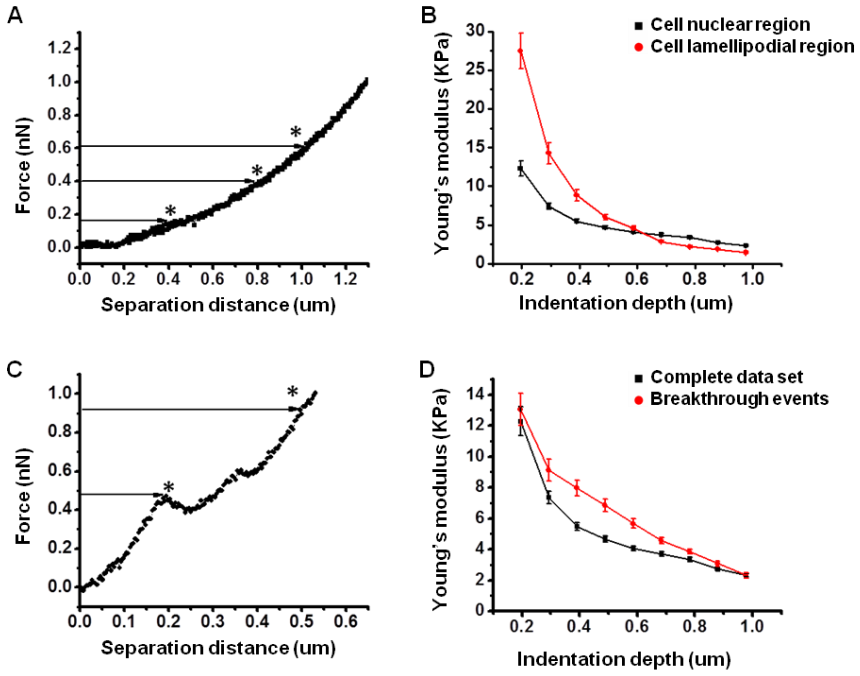

Fig.2 Young's modulus (*E*) of 4T1 cells were obtained at varying indentation depths. (A) Approach region of typical Force-separation curve showing three distinct segments (*). Each segment was fitted through appropriate Sneddon model to acquire *E* (KPa) at the designated indentation depth. (B) Modulus of 4T1 cell nuclear and lamellipodial regions at varying indentation depths. E values for both regions displayed a sharp decrease within first 500nm indentation and plateau after 700nm indentation (C) Example of two distinct segments (*) in the approach region of the Force-separation curve with discontinuity behavior. Breakthrough events were observed in the approach region of the Force-separation curves at varying distance from the point of contact. Break at the breakthrough distance was displayed as compared to the smooth curve shown in (A). (D) Modulus of 4T1 cell nuclear region with discontinuity behaviors (red curve) at varying indentation depths were compared with values of the complete data set. A

significant difference in stiffness between force curves with breakthrough events (red curve) and the complete data set (black curve) was observed between 300nm and 700nm cell indentation.

Measurement of Young's Modulus, (*E*, KPa) for cell nuclear and lamellipodial regions at varying indentation depths

A single cancer cell is often assumed to be a homogenous body when measuring the cell modulus with Hertz-Sneddon model via AFM. Such an assumption disregards the fact that different cellular regions display variant mechanical properties and gives an insufficient understanding of cellular mechanics. The apparent stiffness of cells is not only dependent on the distinct surface regions, but also arises from the complex array of sub-surface structures including actin cytoskeleton, cytoplasm, and nucleus[35-36]. Differentiation among those cellular sub-structural regions allows for better understanding of cell mechanics. Here, we explored the mechanical properties of 4T1 cells considering their inhomogeneous cell bodies. Localized stiffness[17, 37] of 4T1 cells at varying indentation depths was investigated. Fig.2A showed a sample of three subset ranges from the force-separation curve, located at a separation distance of 400nm, 800nm, and 1000nm. Each subset data generated the localized stiffness of 4T1 cells at designated indentation depths. Stiffness at varying indentation depth was plotted in Fig. 2B. E values for both 4T1 cell nuclear and lamellipodial regions decreased within the first 500nm indentation, where stiffness in the cell lamellipodial region was higher than those in the central region. The slopes (value ± standard error) of Young's modulus vs. indentation depth curve in the first 500nm indentation for cell nuclear and lamellipodial regions were -25.3 ± 6.8 KPa/um and -71.6 ± 17.3 KPa/um, respectively. The sharp decrease in stiffness with increasing

indentation depth suggests that the membrane region of the cell displayed distinct mechanical properties than sub-membrane region.

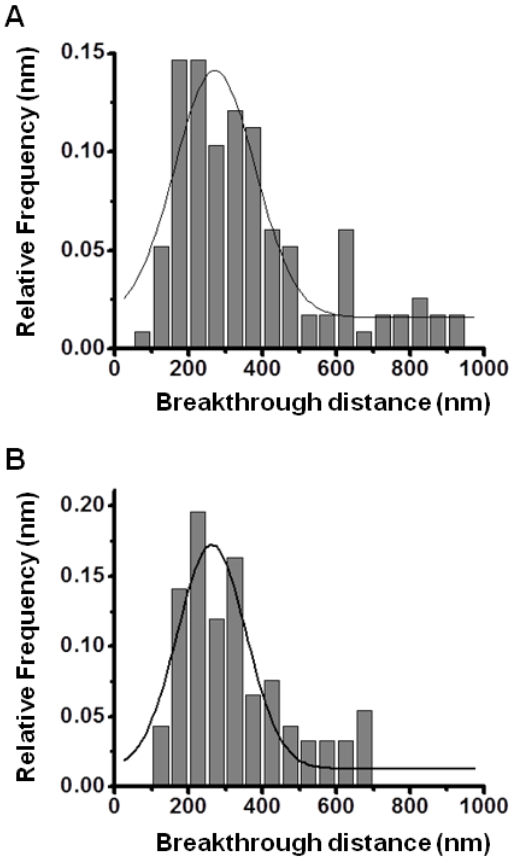

Fig. 3 Breakthrough distances in the approach region of the Force-separation curves of 4T1 cell nuclear and cell lamellipodial regions. (A) Histograms showed relative frequency vs. breakthrough distance with Gaussian fit for 4T1 cell nuclear region. The average breakthrough distances (Mean ± SEM) were 271.0 ± 14.5 nm. (B) Histograms showed relative frequency vs. breakthrough distance with Gaussian fit for 4T1 cell lamellipodial region. The average breakthrough distance was measured to be (Mean ± SEM) 262.4 ± 12.8 nm.

Measurement of breakthrough events

In some cases, discontinuity behavior was observed in the approach region of the Force-separation curves during the AFM cell mechanical measurements, as shown in Fig. 2C. Part of the Force-separation curves implied that these breakthrough events and the locations varied even within a single cell. The breakthrough distances relative to the contact point displayed a Gaussian distribution. The average breakthrough distances (mean ± SEM) for the 4T1 cell nucleus and cell edge were 271.0 ± 14.5 nm and 262.4 ± 12.8 nm, respectively.

The E values for the cell nuclear region at varying indentation depths were investigated to identify the mechanical characteristics behind these breakthrough events. The stiffness of such breakthrough events were compared with the complete data set with all the force curves obtained. The E values for both areas decreased in the first 800nm of cell indentation, and a significant difference in stiffness between breakthrough events (Fig. 2D, red line) and the complete data set (Fig. 2D, black line) was observed between 300nm and 700nm cell indentation. The starting point of deviation (300nm) detected in the localized stiffness graph (Fig. 2D) was very close to the average breakthrough distance (271.0 ± 14.5nm) observed in the approach region of the Force-separation curves during AFM indentation.

Measurement of index of plasticity

Young's modulus values of 4T1 cells using the Sneddon's model and the modified Sneddon's model pertain largely to the elastic properties of cells. However, cells are elastoplastic[38-39] and hysteresis between approach and retract regions of Force-separation

curves are often observed during AFM measurements. The hysteresis indicates the dissipation of energy during the indentation measurements[40], and quantification of such differences will allow us to understand both elastic and plastic properties of cells. Plasticity index is a parameter which characterizes the relative elastic behavior of the material when it undergoes an external force was introduced[41]. The plasticity index ranges from of 0 to 1 (see supplementary information), where 0 signifies fully elastic, and where 1 signifies fully plastic. Intermediate values between 0 and 1 indicate mixed viscoelastic-plastic properties. The average plastic indexes (Mean ± SEM) for the nuclear and lamellipodial regions of 4T1 cells were measured as 0.26 ± 0.01 and 0.37 ± 0.03, respectively, indicating that cell nuclear region was more elastic than cell lamellipodial region.

Measurement of cell adhesions

In addition to the approach curve analysis, rupture events were observed in the retract region of the Force-separation curves during the AFM cell mechanical measurements, as shown in Fig. 1B. Rupture force was quantified as the magnitude of rupture event. The average rupture forces (mean ± SEM) for cell nucleus and cell edge were 87 ± 3 pN and 55 ± 6 pN, respectively, suggesting that the cell nuclear region was 58% more adhesive than that of the cell lamellipodial region.

Peak Force mapping

In addition to AFM force spectroscopy, we also performed Peak force imaging for simultaneous topography and mapping the biomechanical properties of 4T1 cells. A typical Peak Force topography image of the 4T1 cells is shown in Fig. 4A. Line profiles (Fig. 4A) across the cell showed that the height in central region and lamellipodial region of the cell were 5um and 2um respectively. Peak Force imaging enables nanomechanical mapping of material properties, including modulus and adhesion, while simultaneously imaging sample topography at a high resolution[42]. Fig 4B to E shows an example of simultaneous topography and biophysical property mapping of lamellopodial and nuclear regions of a 4T1 cell. The extensions at the cell edge (Fig. 4B) displayed the cytoskeletal network. The Peak Force modulus image (Fig. 4C) of single 4T1 cells showed a contrast in the stiffness across the different surface regions. Stiffness in the lamellipodial region was higher than that in the cell's central region. The cell lamellipodial regions were also observed to be more adhesive compared to cell central region as shown in Fig. 4D.

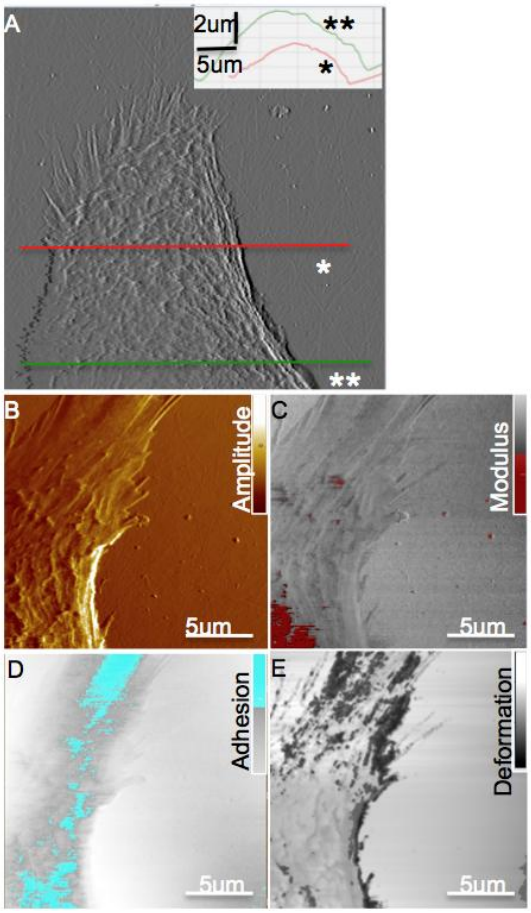

Fig. 4 Peak Force AFM images of live 4T1 cell lamellipodial region characterizing topography and mechanical properties. (A) A representative Peak Force Error image, which was the derivative of topography in the scan direction showing central region and cell extensions at the edge. Line profiles along the central region (**) and lamellipodial region (*) of the cell indicated height variations in the two regions. B-E showed simultaneous maps of a cell with distinct nuclear and lamelliopodial regions. (B) and (C) corresponded to Peak Force error and Young's modulus using DMT fit. Lower modulus regions on the cell (nuclear region) were marked red. D and E corresponded to adhesion (more adhesive regions marked in blue) and deformation (less deformable regions in black) maps of the region as in B. The color scales were from C- for Young's modulus (C), adhesion (D) and deformation image (E) were from 0–42.2 KPa (red

lowest to white highest), 0–100pN (blue most adhesive to white least adhesive) and E- 0–1300 nm (black least deformable to white most deformable), respectively.

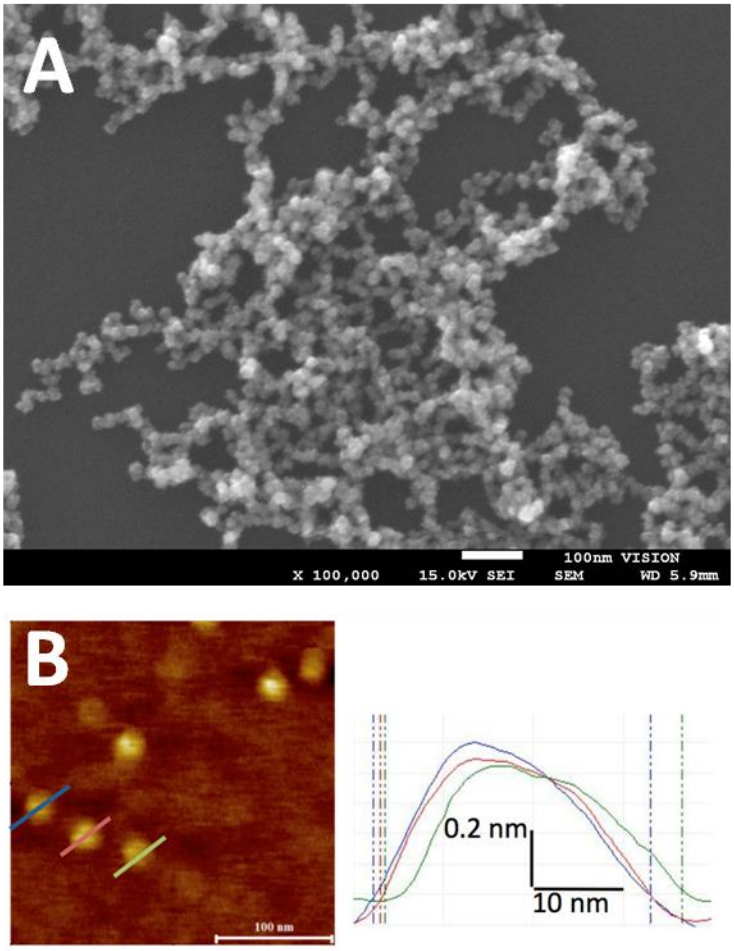

Fig 5. Particle size determined for DPV576 using SEM and AFM imaging. Top image shows SEM image(100,000X magnification) displaying aggregation of particles and bottom image shows AFM scan of isolated DPV576 particles. Line profile of three individual particles are shown on the right with corresponding size of ~20-40nms.

4.4.2 Biophysical analysis on live, metastatic, murine breast cancer cells (4T1) treated by nanodiamond/nanoplatinum

DPV576 particle size determination: SEM and AFM imaging of DPV576 particles show a size range from 20-40nm and the aggregates of interconnected ND/NP particles up to 200nm (Fig. 5 A, B).

DPV576-treated 4T1 cells show decreased Average Young's Modulus (*E*, KPa) measured by AFM

The average Young's modulus (*E*, kPa) was measured for cells and plotted against the relative frequency for all four groups: control (untreated) and DPV576-treated cells at concentrations: 5%, 10% and 15% (Fig. 6, A-D). Control cells demonstrated the highest average Young's modulus of 3.6 ± 0.2 kPa (A), while DPV576-treated cells showed a concentration dependent decrease in Young' modulus with average Young's modulus values of 2.8 ± 0.2 kPa at 5% (B), 2.2 ± 0.1 kPa at 10% (C) and 1.9 ± 0.3 kPa at 15% (D) DPV576 treatments respectively. All three DPV576-treated groups were significantly different from the control group values ($p<0.05$).

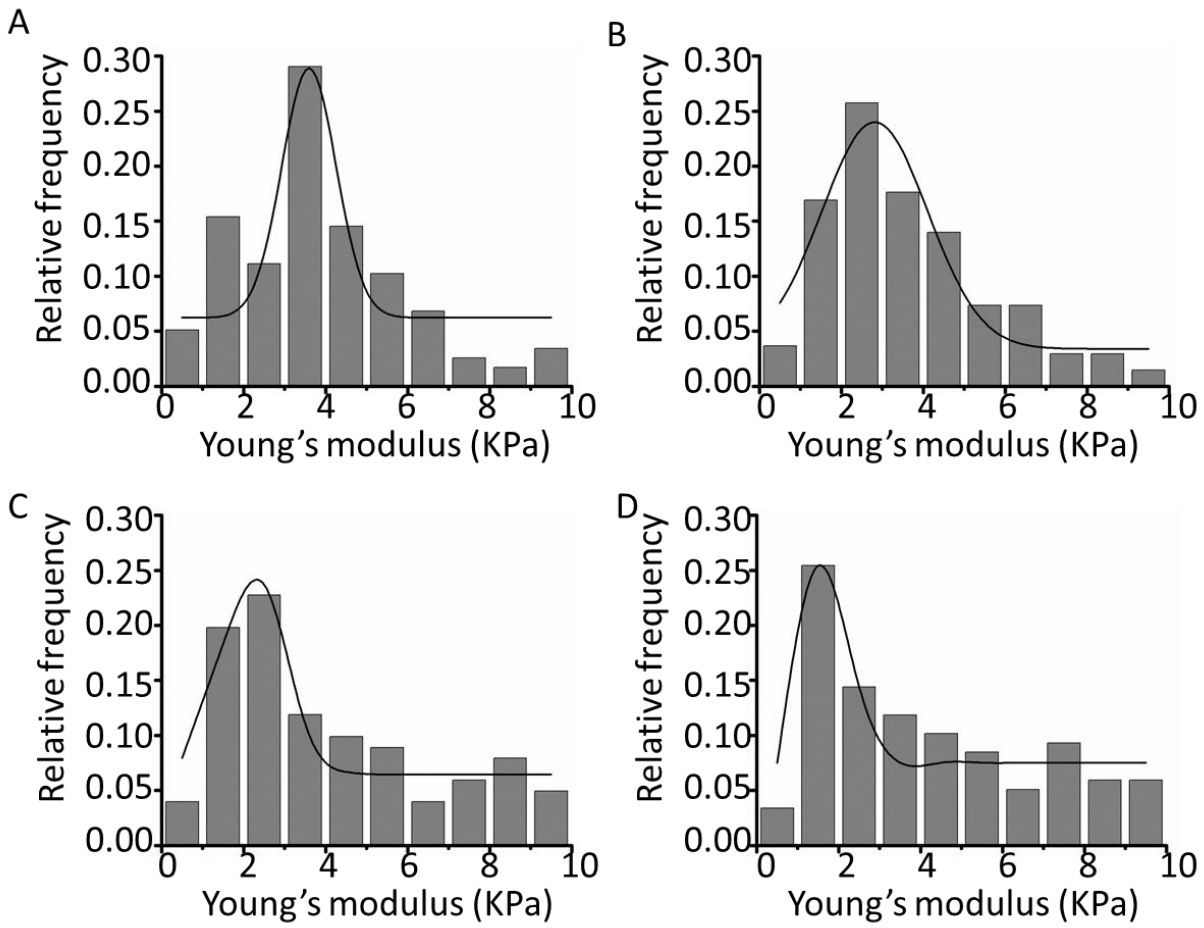

Fig 6. Average Young's modulus (KPa) of DPV576-treated 4T1 cells shows significant reduction in cell stiffness after 2 hrs. Histograms showed relative frequency vs. Young's modulus with Gaussian fits for 4T1 cells. Data shows *E* values (Mean ± SD) for the control group (A), 5% DPV576 (B), 10% DPV576 (C) and 15% DPV576 (D) Cells were cultured in duplicate and 15 cells were measured from each set, giving a total of 30 cells per group. Results were compared using a Gaussian fitted histogram plot. All three DPV576-treated groups were significantly different from the control group values ($p<0.05$).

Localized Young's Modulus, (*E*, KPa) at Varying Indentation Depths

Cells treated with DPV576 displayed a distinct reduction in average stiffness of cells compared with those of untreated cells. However, the cell is not a homogeneous entity and the apparent stiffness of cells also relies on the complex array of sub-surface structures including the actin cytoskeleton, cytoplasm, and nucleus. Differentiating between the stiffness among these sub-structural regions allows for a better understanding of localized mechanical changes in cells upon treatment with DPV576. Therefore, we further explored the localized stiffness of 4T1 cells treated with different doses of DPV576 at various indentation depths.

Fig. 7A shows a sample of three subset ranges from the force-separation curve. Each subset data generated the localized stiffness of 4T1 cells at designated indentation depths. Stiffness measurements taken at varying indentation depths are plotted in Fig. 7B. *E* values for all of the 4T1 cells decreased with increasing indentation depths, which suggested that the cell surface regions were generally stiffer compared to those of the sub-surface regions. At each indentation depth (0.3, 0.6 and 0.9 μm cell indentation), cells treated with a higher dose of DPV576 displayed a lower stiffness, which was in agreement with previous results.

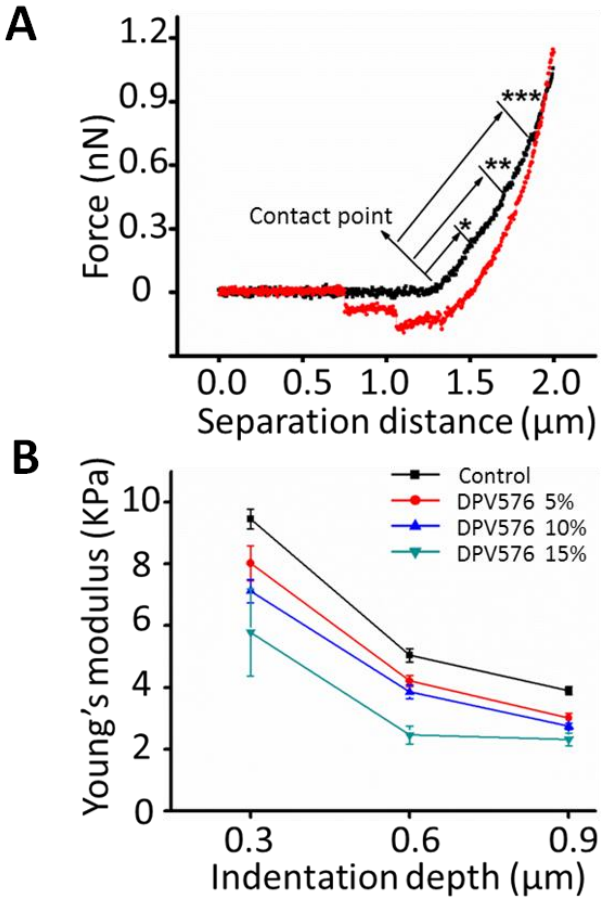

Fig 7. Young's modulus (*E)* of 4T1 cells are obtained at varying indentation depths with different concentrations of DPV576 treatment. (A) Schematic of the AFM indentation experiment above a cell with a conical tip. (B) A sample Force-separation curve is shown. The contact point is defined when the curve starts to deviate from the baseline in the approach region (black curve) of the Force-separation curve. Approach region of typical Force-separation curve is divided into three distinct segments indicated by contact points. Each segment is fitted through the appropriate Sneddon model to acquire *E* (KPa) at the designated indentation depth. (C) Modulus of 4T1 cell nuclear regions at varying indentation depths. *E* values for all concentrations decreased at increased indentation depths. The stiffness of cells treated with a higher concentration of DPV576 becomes softer at all the indentation depths.

Filopodial Retraction (FR) and Retraction Rate

Filopodia are spike-like structures which play an integral role in cell migration and more particularly in metastasis. By studying the shape and retraction rate of filopodia, we can understand the changes in the cells' cytoskeletal network as it is undergoing metastasis [28]. Morphological changes in FR post treatment with DPV576 are shown in Figure 8. Control cells revealed little to no signs of FR (Fig. 8A-C). Cells treated with 5% DPV576 (D-F) showed microspike retraction. Cells treated with 10% DPV576 showed FR from single cells (G-I) as well as cell-cell separation events (J-L). Cells treated with 15% DPV576 showed FR from a single cell (M-O) as well as cell-cell separation events (P-R). All cells were monitored over the course of 40 minutes.

FR rates of cells were measured for each of the four groups and plotted as retraction distance in nanometers vs. time in minutes. It was noted that the control (diamond) and 5% DPV576 (square) groups demonstrated similar velocities of 0.30 nm/min and corresponded to the lowest velocity trends out of all four groups. 10% DPV576 (triangle) treated cells showed an intermediate rate of 0.5 nm/min of FR. 15% DPV576 (circle) treated cells showed the steepest velocity of 1.425 nm/min, indicating the highest rate of FR (Fig. 9).

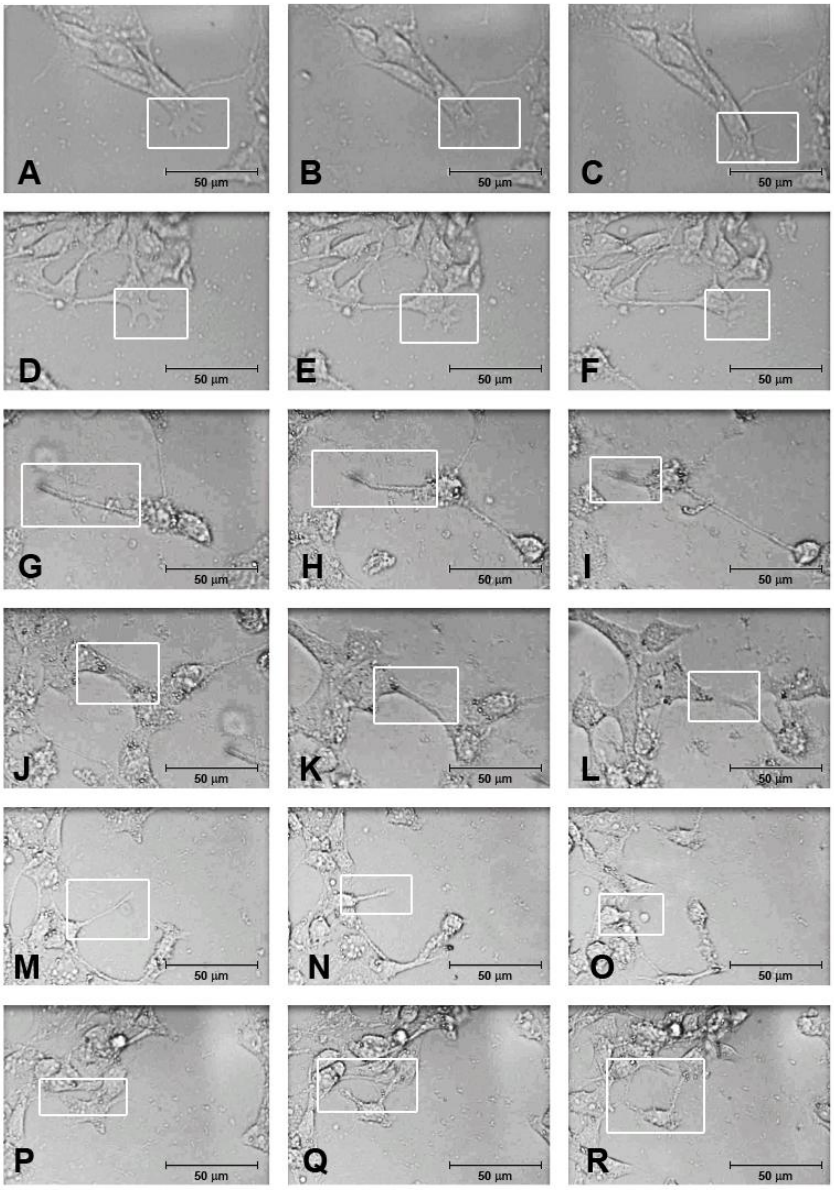

Fig 8. Changes in cell morphology post exposure to increasing concentrations of DPV576. Cell extensions imaged at 0 minutes (left column), 20 minutes (middle) and at 40 minutes (right). Control cells are shown in panels A-C, 5% DPV576 treated cells show partial FR in panels D-F, 10% DPV576 caused partial FR in panels G-I as well as cell-cell separation events causing by filopodial collapse in panels J-L, 15% DPV576 caused complete FR in panels M-O as well as cell-cell separation events caused by filopodial collapse in panels P-R.

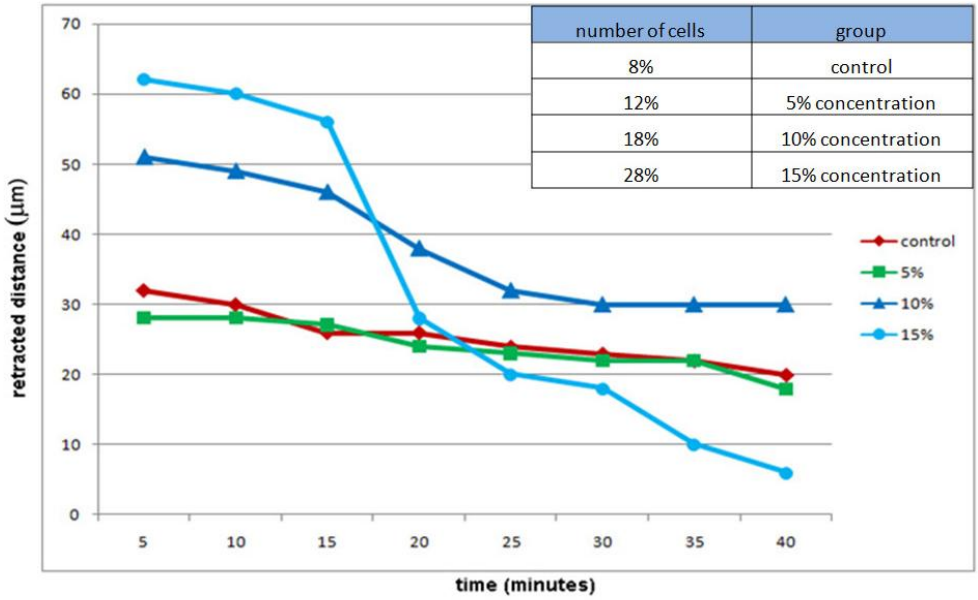

Fig 9. Concentration dependent changes in rate of FR Rates are measured using retraction distance (µm) over time (minutes). Table shows the number of cells (out of 100 cells) with retracted filopodia. The length of retracted filopodia is measured every five minutes over a 40-minute period. Diamond shaped line shows control (untreated cells) rate, square line shows 5% DPV576, triangle line shows 10% DPV576 and circle line shows 15% DPV576. A series of time-lapse images are compared over the course of 40 minutes and the total number of FRs and extensions are measured to acquire data points.

Changes in structural characteristics in cellular Filopodia upon treatment with DPV576, observed via AFM imaging

Atomic force microscopy (AFM) enables high-resolution three-dimensional (3D) imaging of cultured cells. Cells grown on culture dishes were immobilized by a quick fixation step to preserve their transient cellular morphologies followed by AFM characterization in buffer. This approach preserves the structural integrity of individual cells and allows visualization of membrane morphologies, such as microvilli and filopodia. Additional information including the 3D measurements of these characteristic features can be attained from AFM topographs. We examined the filopodial structure for both untreated and cells post treatment with DPV576 using high resolution AFM imaging. Fig. 10A exhibits filopodia from an untreated cell and shows an organized network of straight and well-organized filaments within the filopodia region. However, treatment of 4T1 cells with DPV576 at a concentration of 15% for one hour caused significant changes in the filopodial architecture.

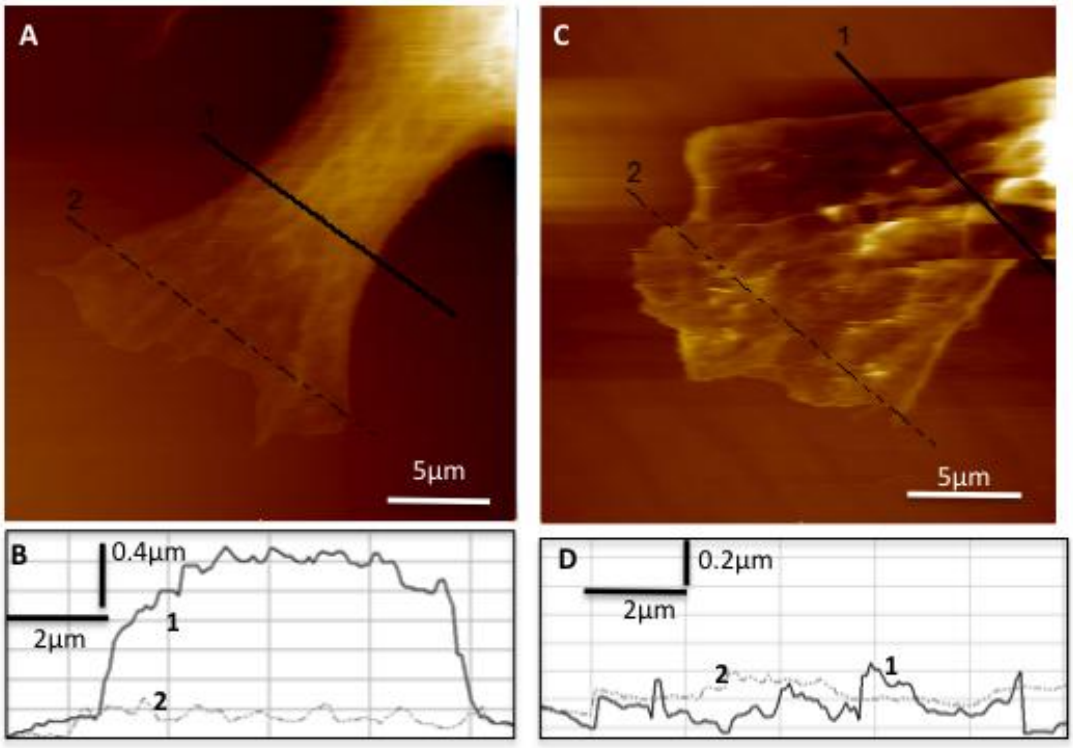

Fig 10. Representative AFM Images of untreated and DPV576 treated 4T1 cells showing structural changes in filopodia regions (A) Filopodia from an untreated cells shows several organized parallel filaments (B) Line profile across two different regions of the filopodia extensions (marked 1, solid black; 2, grey dotted line) show topographic heights of around 1-2µm. (C) A 4T1 cell treated with 15% DPV576 displaying lack of filament organization at the cell edge (D) Topographic height of the filopodia (marked 1, solid black; 2, grey dotted line) show flattened (<0.5µm) cellular edges, suggesting loss of cytoskeleton architecture upon DPV576 treatment as observed in C and D.

4.5 Discussions

In part 1, our current study demonstrated a spatial nanomechanical analysis of 4T1 cells (typically Young's modulus, adhesion, and deformability). Though Peak Force images shows relative difference in nanomechanical properties of different cellular regions, it is still limited in providing quantitative measurements on soft viscoelastic materials[43-45] of inhomogeneous and structurally varied cellular regions. This is particularly true at the lamellipodial regions where thin indentation depths pose the greatest challenge. We initially explored the biophysical properties of two distinct structural regions of 4T1 cells. The stiffness of the cell central region of 4T1 cells were quantified by AFM indentation measurements using the Sneddon model. A thin layer model was used at cell lamellipodial region to avoid substrate effect. The Young's modulus in both cell nuclear region and lamellipodial region indicated bimodal distributions, with two peaks in the histogram of cell stiffness. E values of both peaks in cell lamellipodial region were higher than those in the cell nuclear region. These quantitative measurements were complemented with Peak Force stiffness mapping which displayed a contrast in the stiffness of distinct surface regions. High E values in the cell lamellipodial region suggested this region showed different cytoskeletal structures as compared to the central nuclear region. This is likely due to the web-like structure in cell lamellipodial region of 4T1 cells as revealed through the Peak Force Amplitude.

We also explored the localized mechanical properties of cells at varying indentation depths. The apparent cell stiffness decreased gradually at increasing indentation depths for both the cell nuclear region and the lamellipodial region of the 4T1 cells. E values of lamellipodial region were higher than those in central region at low indentation depth (< 500nm). That the apparent elastic modulus decreased gradually as the probe indented deeper into the cell

suggested membrane regions had higher E values than the underlying sub-membrane regions. Large variations in E values (the slope of stiffness vs. indentation depth curve in the first 500nm indentation for cell lamellipodial region was three times as big as that in cell nuclear region) indicated that localized structures at varying indentation depth were distinct, likely resulting from differences in stiffness of the cell membrane, cytoplasm, and nucleus regions. The observed breakthrough events in the approach curve during the AFM Force-separation curves were analyzed. The measured breakthrough distances were close to the start point of deviation (300nm) observed in the localized stiffness graph. This suggested that the sub-membrane regions for cells showing the breakthrough events were distinct compared with the complete data set of 4T1 cells. Though a 2s recovery time was given between each force curve for single cell, the membrane structure of the cell could have been preburbed because of the external force caused by the AFM tip[46-47]. Alternatively, the presence of inclusions underneath the membrane could have caused this discrepancy.

Other mechanical characteristics of 4T1 cells were further studied. The plastic index for both the cell nuclear and lamellipodial regions indicated mixed viscoelastic-plastic properties for 4T1 cells. The average plastic indexes of the lamellipodial region were higher than that in the central region, which signified that the cell nucleus was more elastic (more than 30%) than the cell lamellipodial region. We showed that the cell nucleus is 58% more adhesive than that of cell edge. These quantitative results were confirmed in the adhesion mapping from Peak Force, which clearly displayed higher adhesions in the cell central region than those in cell lamellipodial region. This could provide insights into the cell mobility[48]; however, a larger contact area between the tip and cell membrane in cell central region compared with that of cell lamellipodial region should be considered.

In part 2, we carried out the nanomechanical characterization technique and applied it to explore the effects of NDs over 4T1 cells. Our previous work has indicated that NDs could induce the morphological damage of multi-drug resistant, human leukemic cells (HL60/AR) cells based on AFM topographical imaging [49] but the effect of DPV576 NPs on the nanomechanical properties of single cells remained unexplored. As differences in cell morphology might also lead to difference in their nanomechanical characteristics, we further used AFM force spectroscopy to probe the nanomechanical changes at the single cell level by probing average and localized, depth dependent Young's modulus from control and DPV treated 4T1 cells. In the current study, we showed that 4T1 metastatic breast cancer cells, exposed to DPV576 resulted in decreased cell stiffness of 4T1 cells compared to control cells in a dose dependent manner. Furthermore, the localized cell modulus values for all doses of 4T1 cells decreased with increasing indentation depths, suggesting that the cell surface regions were generally stiffer compared to those of the sub-surface regions. At each indentation depth, cells treated with a higher dose of DPV576 displayed a lower stiffness. Our results showing that DPV576 NPs can decrease the Young's modulus of 4T1cells can be compared to similar findings from other studies that reported reduction in cell stiffness of fibroblasts by silica nanoparticles [50] or reduction in stiffness of tumor epithelial cells and reduced tumor size influenced by carbon nanorods [51]. Other nanoparticles [52] such as cobalt acetate also exhibited a decrease in the stiffness of *Brevibacterium casei* cells [53]. Titanium oxide nanoparticles were shown to increase stiffness of human neutrophils [54] while decreasing stiffness in human skin fibroblasts [55].

The cytoskeleton of cells, an intricate structural framework that predominantly shapes a cell and provides its mechanical rigidity [56]. In particular, F-actin is reported as a potential

target of nanomaterials in cancer cells [57] and the integrity of actin network can be reflected by the Young's modulus measurement by AFM [58]. Constant alterations in actin organizational network occurs during cancer cell migration and extravasation. In particular, actin polymerization results in the formation of slender protrusive structures known as invadopodia and filopodia. These protrusions are used by the cell to move through the extracellular matrix, migrate through the vasculature and tunnel to a new tumor site [28]. To further study the role of F-actin in NPs induced Young's modulus changes of 4T1 cells, we measured the morphological changes in FR post treatment with DPV576. Our results indicate that the DPV576 treatment of cells showed an increased and rapid rate of FR compared to control cells.

Additionally, Filopodia, associated with cell spreading, were captured and visualized in three dimensions and revealed high-density ridges and sub-cellular cytoskeleton organization of cellular extensions. The AFM imaging approach provided an effective means to characterize these cellular extensions and the changes associated with DPV576 treatment of cells at high resolution. The quantitative imaging and measurements allowed for systematic correlation of membrane structural extensions with the cellular changes in DPV treated cells. Based on the 3D topographic images obtained using AFM, it is evident that that the structural cytoskeletal organization of the cells is altered. The filopodia retract upon DPV576 treatment, resulting in rapid loss of filamentous actin bundles within the cell extensions. The filopodia become significantly flattened compared to untreated controls, likely due to loss of architecture within the cellular cytoskeleton. It appears that the changes in cellular cytoskeleton propagate along the cell length, thereby influencing the reduction both the average and localized depth dependent Young's modulus of the treated cells.

4.6 Summary

We demonstrated that nanomechanical measurements of metastatic cancer cells are dependent on the localized cellular regions analyzed. We showed that the 4T1 cell central regions are softer, more elastic and more adhesive than the cell lamellipodial regions. The surface stiffness in both cell nuclear and lamellipodial regions were higher than those of underlying layers. Peak Force QNM of single 4T1 cell revealed a thorough nanomechanical mapping at distinct structural regions. The mechanical mapping including tomography, modulus, adhesion, and deformation was complemented with the AFM force indentation analysis. The capability to detect and correlate the cell biomechanical characteristics quantitatively using AFM and Peak Force AFM provides an improved and integrative structure versus mechanics analysis of metastatic cancer cells at the nanoscale level.

DPV576 has the ability to decrease the stiffness of metastatic breast cancer cells and restructure their filopodia organization. Using AFM based average cell modulus and depth dependent analysis, we were able to detect a dose dependent decrease in cell stiffness (as measured using Young's modulus) for DPV576 treated cells. Moreover, time lapse light microscopy and AFM imaging revealed that DPV576 treatment caused FR and filopodial degeneration in cells. The AFM imaging approach provided an effective method to characterize the cellular extensions and the changes associated with DPV576 treatment of cells at high resolution. Our study reveals the important biophysical and morphological effects of DPV576 on metastatic cells and suggests that it may be useful as an anti-metastatic agent by decreasing cell stiffness.

4.7 References

1. Wang, Y., *Breast cancer metastasis driven by ErbB2 and 14-3-3zeta: A division of labor.* Cell Adh Migr, 2010. **4**(1): p. 7-9.
2. Fan, P., et al., *Modulating therapeutic effects of the c-Src inhibitor via oestrogen receptor and human epidermal growth factor receptor 2 in breast cancer cell lines.* Eur J Cancer, 2012. **48**(18): p. 3488-98.
3. Sengupta, S., S. Mitra, and K.K. Bhakat, *Dual regulatory roles of human AP-endonuclease (APE1/Ref-1) in CDKN1A/p21 expression.* PLoS One, 2013. **8**(7): p. e68467.
4. Pavan, W.J. and D.W. Raible, *Specification of neural crest into sensory neuron and melanocyte lineages.* Developmental Biology, 2012. **366**(1): p. 55-63.
5. Xia, R.H., et al., *The Combination of SMAD4 Expression and Histological Grade of Dysplasia Is a Better Predictor for the Malignant Transformation of Oral Leukoplakia.* Plos One, 2013. **8**(6).
6. Sharma, S., et al., *Correlative nanomechanical profiling with super-resolution F-actin imaging reveals novel insights into mechanisms of cisplatin resistance in ovarian cancer cells.* Nanomedicine-Nanotechnology Biology and Medicine, 2012. **8**(5): p. 757-766.
7. Cross, S.E., et al., *Nanomechanical analysis of cells from cancer patients.* Nat Nanotechnol, 2007. **2**(12): p. 780-3.
8. Suresh, S., *Nanomedicine: elastic clues in cancer detection.* Nat Nanotechnol, 2007. **2**(12): p. 748-9.

9. Suresh, S., *Biomechanics and biophysics of cancer cells.* Acta Biomater, 2007. **3**(4): p. 413-38.

10. Suresh, S., et al., *Connections between single-cell biomechanics and human disease states: gastrointestinal cancer and malaria.* Acta Biomaterialia, 2005. **1**(1): p. 15-30.

11. Guck, J., et al., *Optical deformability as an inherent cell marker for testing malignant transformation and metastatic competence.* Biophysical Journal, 2005. **88**(5): p. 3689-3698.

12. Unnikrishnan, G.U., V.U. Unnikirishnan, and J.N. Reddy, *Constitutive material modeling of cell: a micromechanics approach.* Journal of Biomechanical Engineering-Transactions of the Asme, 2007. **129**(3): p. 315-323.

13. Laurent, V.M., et al., *Gradient of rigidity in the lamellipodia of migrating cells revealed by atomic force microscopy.* Biophys J, 2005. **89**(1): p. 667-75.

14. Lee, Y.J., D. Patel, and S. Park, *Local Rheology of Human Neutrophils Investigated Using Atomic Force Microscopy.* International Journal of Biological Sciences, 2011. **7**(1): p. 102-111.

15. Park, S. and Y.J. Lee, *Nano-mechanical Compliance of Muller Cells Investigated by Atomic Force Microscopy.* International Journal of Biological Sciences, 2013. **9**(7): p. 702-706.

16. Pogoda, K., et al., *Depth-sensing analysis of cytoskeleton organization based on AFM data.* European Biophysics Journal with Biophysics Letters, 2012. **41**(1): p. 79-87.

17. Kasas, S. and G. Dietler, *Probing nanomechanical properties from biomolecules to living cells.* Pflugers Archiv-European Journal of Physiology, 2008. **456**(1): p. 13-27.

18. Roduit, C., et al., *Stiffness tomography by atomic force microscopy.* Biophys J, 2009. **97**(2): p. 674-7.

19. Lekka, M. and P. Laidler, *Applicability of AFM in cancer detection.* Nat Nanotechnol, 2009. **4**(2): p. 72; author reply 72-3.

20. Yau, W.L., et al., *Over-Expression of miR-106b Promotes Cell Migration and Metastasis in Hepatocellular Carcinoma by Activating Epithelial-Mesenchymal Transition Process.* Plos One, 2013. **8**(3).

21. Quint, D.A. and J.M. Schwarz, *Optimal orientation in branched cytoskeletal networks.* J Math Biol, 2011. **63**(4): p. 735-55.

22. Bray, D. and K. Chapman, *Analysis of microspike movements on the neuronal growth cone.* J Neurosci, 1985. **5**(12): p. 3204-13.

23. Tomaskovic-Crook, E., E.W. Thompson, and J.P. Thiery, *Epithelial to mesenchymal transition and breast cancer.* Breast Cancer Research, 2009. **11**(6).

24. Simic, P., et al., *SIRT1 Suppresses the Epithelial-to-Mesenchymal Transition in Cancer Metastasis and Organ Fibrosis.* Cell Reports, 2013. **3**(4): p. 1175-1186.

25. Schrand, A.M., et al., *Are diamond nanoparticles cytotoxic?* J Phys Chem B, 2007. **111**(1): p. 2-7.

26. Yuan, Y., et al., *Pulmonary toxicity and translocation of nanodiamonds in mice.* Diamond and Related Materials, 2010. **19**(4): p. 291-299.

27. Yau, W.L., et al., *Over-expression of miR-106b promotes cell migration and metastasis in hepatocellular carcinoma by activating epithelial-mesenchymal transition process.* PLoS One, 2013. **8**(3): p. e57882.

28. Machesky, L.M., *Lamellipodia and filopodia in metastasis and invasion.* FEBS Lett, 2008. **582**(14): p. 2102-11.

29. Ghoneum, M., A. Ghoneum, and J. Gimzewski, *Nanodiamond and nanoplatinum liquid, DPV576, activates human monocyte-derived dendritic cells in vitro.* Anticancer Res, 2010. **30**(10): p. 4075-9.

30. Sneddon, I.N., *Boussinesqs Problem for a Rigid Cone.* Proceedings of the Cambridge Philosophical Society, 1948. **44**(4): p. 492-507.

31. Charras, G.T., P.P. Lehenkari, and M.A. Horton, *Atomic force microscopy can be used to mechanically stimulate osteoblasts and evaluate cellular strain distributions.* Ultramicroscopy, 2001. **86**(1-2): p. 85-95.

32. Rico, F., et al., *Probing mechanical properties of living cells by atomic force microscopy with blunted pyramidal cantilever tips.* Physical Review E, 2005. **72**(2): p. 021914.

33. Gavara, N. and R.S. Chadwick, *Determination of the elastic moduli of thin samples and adherent cells using conical atomic force microscope tips.* Nature Nanotechnology, 2012. **7**(11): p. 733-736.

34. Gross, S.R., *Actin binding proteins Their ups and downs in metastatic life.* Cell Adhesion & Migration, 2013. **7**(2): p. 199-213.

35. Caille, N., et al., *Contribution of the nucleus to the mechanical properties of endothelial cells.* J Biomech, 2002. **35**(2): p. 177-87.

36. Kim, Y., et al., *Characterization of cellular elastic modulus using structure based double layer model.* Medical & Biological Engineering & Computing, 2011. **49**(4): p. 453-462.

37. Roduit, C., et al., *Stiffness Tomography by Atomic Force Microscopy.* Biophysical Journal, 2009. **97**(2): p. 674-677.

38. Rebelo, L.M., et al., *Comparison of the viscoelastic properties of cells from different kidney cancer phenotypes measured with atomic force microscopy.* Nanotechnology, 2013. **24**(5).

39. Peeters, E.A.G., et al., *Viscoelastic properties of single attached cells under compression.* Journal of Biomechanical Engineering-Transactions of the Asme, 2005. **127**(2): p. 237-243.

40. Klymenko, O., et al., *Energy Dissipation in the AFM Elasticity Measurements.* Acta Physica Polonica A, 2009. **115**(2): p. 548-551.

41. Briscoe, B.J., L. Fiori, and E. Pelillo, *Nano-indentation of polymeric surfaces.* Journal of Physics D-Applied Physics, 1998. **31**(19): p. 2395-2405.

42. Bede Pittenger, N.E., Chanmin Su, Ben Ohler, *Quantitative mechanical property mapping at the nanoscale with PeakForce QNM.* 2010.

43. Tranchida, D., et al., *Nanoscale mechanical characterization of polymers by atomic force microscopy (AFM) nanoindentations: viscoelastic characterization of a model material.* Measurement Science & Technology, 2009. **20**(9).

44. Clifford, C.A. and M.P. Seah, *Quantification issues in the identification of nanoscale regions of homopolymers using modulus measurement via AFM nanoindentation.* Applied Surface Science, 2005. **252**(5): p. 1915-1933.

45. Withers, J.R. and D.E. Aston, *Nanomechanical measurements with AFM in the elastic limit.* Adv Colloid Interface Sci, 2006. **120**(1-3): p. 57-67.

46. Kasas, S., G. Longo, and G. Dietler, *Mechanical properties of biological specimens explored by atomic force microscopy.* Journal of Physics D-Applied Physics, 2013. **46**(13).

47. Liang, X., G. Mao, and K.Y. Ng, *Mechanical properties and stability measurement of cholesterol-containing liposome on mica by atomic force microscopy.* J Colloid Interface Sci, 2004. **278**(1): p. 53-62.

48. Huttenlocher, A., et al., *Integrin and cadherin synergy regulates contact inhibition of migration and motile activity.* Journal of Cell Biology, 1998. **141**(2): p. 515-526.

49. Ghoneum, A., S. Sharma, and J. Gimzewski, *Nano-hole induction by nanodiamond and nanoplatinum liquid, DPV576, reverses multidrug resistance in human myeloid leukemia (HL60/AR).* Int J Nanomedicine, 2013. **8**: p. 2567-73.

50. Gaharwar, A.K., et al., *Physically crosslinked nanocomposites from silicate-crosslinked PEO: mechanical properties and osteogenic differentiation of human mesenchymal stem cells.* Macromol Biosci, 2012. **12**(6): p. 779-93.

51. Lee, J., et al., *Modulating malignant epithelial tumor cell adhesion, migration and mechanics with nanorod surfaces.* Biomed Microdevices, 2011. **13**(1): p. 89-95.

52. Lee, S.M., et al., *Nanomechanical measurement of astrocyte stiffness correlated with cytoskeletal maturation.* J Biomed Mater Res A, 2014.

53. Kumar, U., K. Vivekanand, and P. Poddar, *Real-time nanomechanical and topographical mapping on live bacterial cells-Brevibacterium casei under stress due to their exposure to Co2+ ions during microbial synthesis of Co3O4 nanoparticles.* J Phys Chem B, 2009. **113**(22): p. 7927-33.

54. da Rosa, E.L., *Kinetic effects of TiO2 fine particles and nanoparticles aggregates on the nanomechanical properties of human neutrophils assessed by force spectroscopy.* BMC Biophys, 2013. **6**(1): p. 11.

55. Vileno, B., et al., *Stiffness alterations of single cells induced by UV in the presence of nanoTiO2.* Environ Sci Technol, 2007. **41**(14): p. 5149-53.

56. Guck, J., et al., *Optical deformability as an inherent cell marker for testing malignant transformation and metastatic competence.* Biophys J, 2005. **88**(5): p. 3689-98.

57. Wang, L., et al., *Selective targeting of gold nanorods at the mitochondria of cancer cells: implications for cancer therapy.* Nano Lett, 2011. **11**(2): p. 772-80.

58. Solon, J., et al., *Fibroblast adaptation and stiffness matching to soft elastic substrates.* Biophys J, 2007. **93**(12): p. 4453-61.

Chapter 5.

Correlative Nanoscale Imaging of Actin Filaments and its Complexes

5.1 Abstract

Actin remodeling is an area of interest in biology in which correlative microscopy can bring new way to analyze protein complexes at the nanoscale. Advances in EM, X-ray diffraction, fluorescence, and single molecule techniques have provided a wealth of information about the modulation of F-actin structure and its regulation by actin binding proteins (ABPs). Yet, there are technological limitations of these approaches to achieving quantitative molecular level information on the structural and biophysical changes resulting from ABPs interaction with F-actin. Fundamental questions about actin structure and dynamics and how these determine the function of ABPs remain unanswered. Specifically, how local and long-range structural and conformational changes result in ABPs induced remodeling of F-actin needs to be addressed at the single filament level. Advanced, sensitive and accurate experimental tools for detailed understanding of ABPs-actin interactions are much needed. This article discusses the current understanding of nanoscale structural and mechanical modulation of F-actin by ABPs at the single filament level using several correlative microscopic techniques, focusing mainly on results obtained by Atomic Force Microscopy (AFM) analysis of ABP-actin complexes.

5.2 Introduction

To understand biological processes at the molecular level it is essential to identify the involved proteins and their assemblies, to characterize their structure and function, and to unravel their interplay with other proteins and molecules[1]. Actin remodeling is an area in biology where AFM can bring a new way to analyze protein complexes at the nanoscale. Actin[2] forms filamentous protein complexes (F-actin) (Fig.1) found in almost all eukaryotic cells[3]. Actin cytoskeleton is an important, exciting and fascinating area of research in cell biology.

Important, because actin and the dynamic remodeling of its various assembly forms are the central players in cell movement and shape[3], cytokinesis, intracellular transport, and other biological processes[4-6]. Exciting, because the fast progress in this field has increased greatly over the last few years our knowledge of the proteins and factors that affect and/or regulate different stages of actin filament nucleation and elongation[7-9], bundling and cross-linking[10], and severing and de-polymerization[11-13]. Fascinating, because many aspects of the remodeling of actin filaments are yet to be clarified.

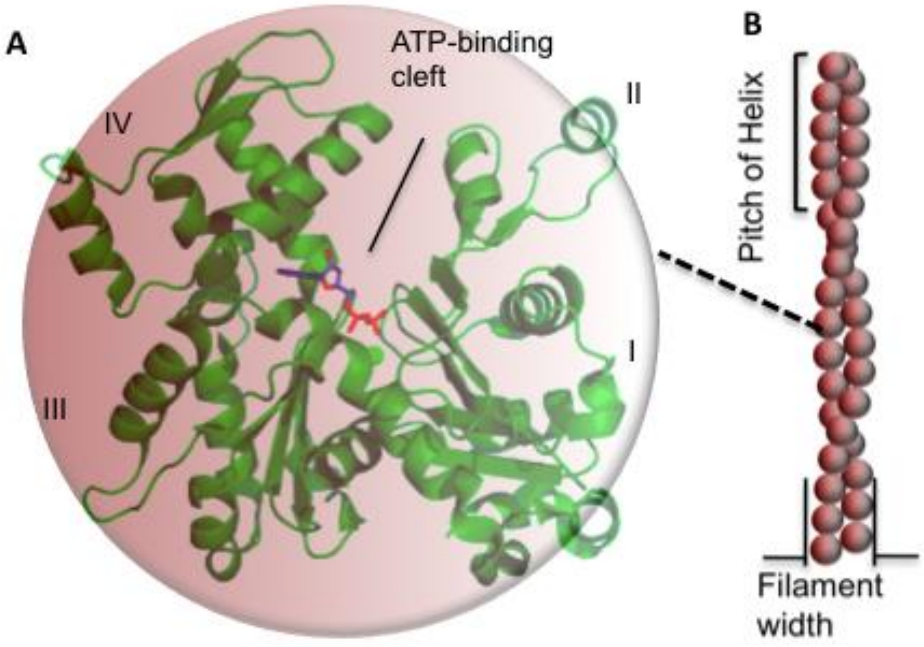

Fig. 1 Monomeric (G-actin) and filamentous (F-actin) forms of actin (A) G-Actin (PDBcode: 1j6z) [2] with highlighted ADP and divalent cation (B) Monomers assemble for form long filaments.

Current techniques to study F-actin-ABP complexes

In different cells actin cytoskeleton is regulated by more than 150 ABPs that enable its important physiological functions[14]. Many of those proteins bind to/interact with two or more actin protomers within the filament creating conditions and natural pathway for cooperative spreading of changes in F-actin. Techniques like x-ray crystallography[15-19], electron microscopy[20-23] and nuclear magnetic resonance spectroscopy[23-24] have contributed greatly to elucidate the structure and properties of F-actin-ABP complexes. Some of the major advantages and limitations of these techniques are summarized in **Table 1**.

Electron microscopy (EM) is the principle technique in common use for high- resolution studies of F-actin structures (Fig.2). Based on images obtained by transmission electron microscopy (TEM), F-actin filaments have been shown to exhibit a double strand helical structure, with a helical pitch of 36-37 nm and microns in length. More recently, reconstruction of filaments from many cryo-electron microscopy (cryo-EM) images has proved to be more powerful for elucidating F-actin architecture[25-28], and capable of revealing details at resolutions in the range of 4 to 5 Å[29-30]. Cryo-EM, however, has certain inherent limitations. It is useful mainly for analyzing regular F-actin structures having uniform helical symmetry. It yields the "average" structure for the entire F-actin filament population or sub-populations and does not elucidate heterogeneity of individual helix changes. More advanced applications of cryo-EM[25, 31] provide information on structures lacking any helical symmetry, but even here the common assumption is that all actin filaments have identical helical parameters. EM images have so far been difficult to analyze (Fig. 2) when the helical structures are polymorphic and lack architectural uniformity as in the case of several ABPs decorated actin filaments, such as with cofilin[22].

Table 1. F-actin ABP structural determination techniques

Technique	Advantages	Limitations
X-Ray crystallography	▪Atomic resolution ▪Suitable for G-actin	▪No 3D crystal structures for F-actin-ABP complexes
NMR	▪Atomic resolution ▪Dynamic information	▪Large sample amounts, protein labeling, >40KDa difficult
Electron crystallography	▪-nm to atomic resolution	▪Well ordered 2D crystals, technically difficult
Electron Microscopy	▪Study of large complexes like F-actin ▪Study interactions b/w actin monomers	▪Electron dense staining and UHV, resolution limit ~5A ▪<100KDa difficult
Cryo-EM	▪3.5-4A resolution ▪More informative ABP-F-actin complex architecture ▪Multiple orientations of ABPs-F-actin complexes	▪Not suitable for analyzing ABP induced changes in actin filaments
Atomic Force Microscopy	▪um to atomic resolution ▪No fixing, electron dense staining, UHV ▪Quantitative 3D structural information on single ABP-F-actin complexes ▪Study ABP-F-actin structure heterogeneity by measuring individual helix without averaging ▪Measure nanoscale assembly of ABPs on F-actin for binding cooperative determination ▪Inexpensive equipment compared to above techniques; simple instrumentation design and data interpretation	▪Surface technique ▪Immobilization of ABPs-F-actin on substrates ▪Relatively new tool in ABPs-F-actin structural studies
Light microscopy/ FRET/TIRF	▪Dynamic studies ▪mm to ~300nm resolution range ▪Most commonly used technique for ABPs-F-actin binding cooperativity determination	▪Diffraction limit~200-300nm

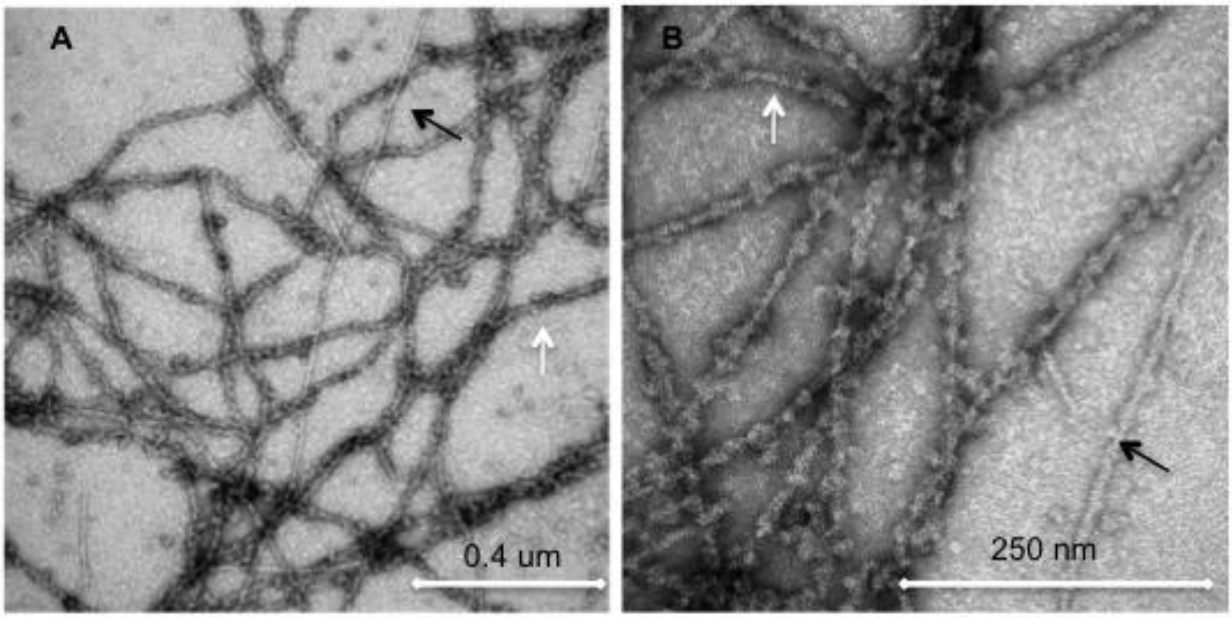

Fig. 2 TEM images of negatively stained drebrin-F-actin. Undecorated and drebrin decorated filaments are marked by black and white arrows respectively.

5.3 Results and Discussions

Applications of AFM to High-resolution studies of proteins form and function

AFM[32] is a powerful technique for biophysical nanoscale characterization of biological structures [33-38]. It offers unique capability for direct 3D imaging of single actin filaments without electron dense staining, fixation, or extreme temperatures, and with imaging resolution comparable to that of electron microscopes. Additionally, AFM is a versatile technique that also brings information on structure, mechanics, dynamics and specific bio-molecular binding interactions under physiological solvent conditions[37, 39-41]. The atomic force microscope is a member of the scanning probe microscopy techniques, which utilize a probing tip that scans the surface of a sample. Soft cantilevers with spring constants of about 0.01–0.1 N/m can sense

forces as low as few piconewtons, and piezoelectric scanners can translate the sample or tip in x, y and z-directions with sub-nanometer resolution. This combined functionality enables the atomic force microscope to render three-dimensional images of the sample with atomic resolution[42]. Since the development of AFM as an imaging technique in structural biology, a number of selected proteins and protein conformational changes have been investigated at sub-molecular resolution. As a contact microscope, AFM does not suffer from diffraction limits, unlike optical microscopes, enabling it to reach atomic resolution. In particular, Tapping mode imaging[43] involves minimal physical contact with the samples, which helps in preventing tip-induced damage to soft biological molecules. Consequently, AFM's exceptionally high signal-to-noise sub-nanometer lateral resolution and vertical resolution of 1Å[36, 44-46] can be achieved.

Several examples from the literature show the potential of AFM to study both the "form" and "function" of proteins, thereby resolving questions in proteomics and structural biology quasi-simultaneously. Among biomolecules, membrane proteins in their native state have been imaged most extensively[36, 46]. The surface topography of bacteriorhodopsin was resolved down to 1 nm [45], and vertical resolution of up to ~1Å was attained for the native complex in photosynthetic membranes[44, 47]. Besides isolated viruses and phages[48-49], specific substructures like viral capsomeres, bacteriophage connectors and tails[50-51] have been imaged at a resolution comparable to EM. Nevertheless, native-like 2D arrays or structurally oriented (but not necessarily homogeneous) conformations (e.g., membranes) or linear biomolecules-DNA[34], RNA[52], collagen[53], or amyloid[54], are better suited for high resolution AFM imaging than single isolated protein molecules. This technique was successfully used for imaging 'bare' actin filaments[55].

AFM imaging for mapping structural changes and remodeling of F-actin induced by ABPs

To date only few examples of ABPs changing the helical twist of F-actin have been reported. The most striking case is that of cofilin, which exerts its severing function by capturing and stabilizing an 'over-twisted' actin conformation and consequently, leading to filaments severing. Quantitative single filament level information on changes in helical twist, increase in filament volume and change in mechanical properties such as persistence length are needed to advance our understanding of filament stabilization or disassembly by cofilin and other ABPs. AFM imaging can be effectively used to provide detailed biophysical nanoscale characterization by determining ABP-induced changes in individual helix of unstained, unfixed actin filaments at high resolution, without averaging.

Our recent work reported images of bare actin filaments (Fig. 3A) obtained using tapping mode AFM imaging[56]. The measured helical pitch (36nm) (Fig. 3C) and persistence length of actin filaments obtained from AFM images agreed well with the EM [57] and thermal fluctuation[58] observations, respectively. This validates the use of AFM technique for quantitative in vitro studies of structural and mechanical remodeling of actin filaments. In a novel application of AFM, we imaged the remodeling of F-actin by drebrin A (a neuronal ABP) and showed that it involves changes of helical twist (Fig. 3D) and actin filament stiffness (55% persistence length increase and higher elastic modulus)[56]. To further test the resolution and validate the analysis of AFM actin filament images, we examined cofilin bound actin filaments. Cofilin is an extensively studied ABP, which is known to change the F-actin structure and mechanics based on EM studies[22]. Cofilin-decorated F-actin had a significantly reduced helical pitch (~28.7nm), in good agreement with previously reported results[22]. Thus, structural differences between unbound- and drebrin and cofilin bound-F-actin, as measured by AFM,

demonstrate that this method can determine how ABPs change the structure of the actin filaments[56] and hence affect their dynamics and polymerization/depolymerization. Thus, AFM can be added to the list of techniques suitable for obtaining molecular level structural details of F-actin complexes at nanoscale resolution**.** AFM imaging analysis can easily provide individual helix measurements of ABP-F-actin complexes that are difficult to obtain using other imaging methods, such as EM or cryo-EM. The proof-of-concept demonstration of AFM based F-actin remodeling by drebrin, paves the way for similar measurements on other ABPs. It is likely that the use of AFM would expand, making it a routine and complementary technique to EM and cryo-EM to study ABPs- F-actin complexes, and to analyze the structural and mechanical modulation of F-actin by these proteins.

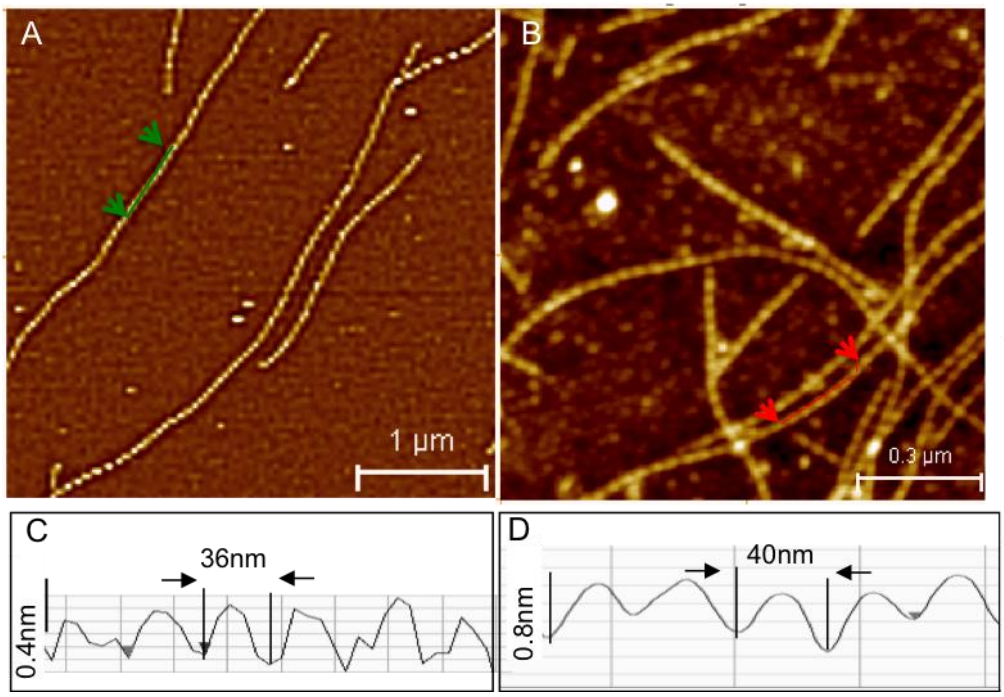

Fig. 3 AFM tapping mode images of (A) bare actin (B) drebrin-F-actin at AFM images. (C-D) show helix pitch from line profiles along bare and drebrin F-actin. Adapted from Sharma S. *et al*. [55] with permission from American Chemical Society.

Measurements of Cooperativity of ABP-binding and F-actin remodeling

Most molecular models of F-actin assume precisely defined filaments with a homogeneous rigid rod-like structure. However, there is abundant evidence revealing polymorphic states of F-actin and variations in the helical twist of the filament[59-61]. First, actin filaments can bend and flex along their long axis with a persistence length (a mechanical parameter that quantifies stiffness) of about 17 μm (in a complex with phalloidin)[62]. Second, actin subunits in a filament can also twist and tilt[63], leading to long-range rearrangements of actin subunits within filaments along their long axis. Lastly, several actin subdomains, such as the DNAse-I-binding loop, are mobile. Thus, actin filaments can adopt multiple conformations. This is the case for actin filaments in different nucleotide states (ATP, ADP-Pi or ADP)[64], but also for actin filaments with identical bound nucleotides[29, 65]. Moreover, different structures of the filament have been reported for its complexes with ABPs. Many ABPs exhibit binding preference for specific actin filament conformations *in vitro*[66]. ABPs might stabilize specific actin filament conformations with long-range effects, or selectively bind to preferred actin filament populations. ADF/cofilin has been shown to interact with and stabilize a specific conformational state of ADP–F-actin, and to modify the mechanical properties of the bound filaments[11, 67-68]. Structural modification of F-actin have also been reported for myosins[69], gelsolin[70-71] and other proteins.

The different conformations of an actin filament regulate its binding properties (F-actin binding sites are non-equivalent and non-identical). Actin filaments are not decorated with similar ratios of all the ABPs present in the cell. Most likely, F-actin remodeling mechanisms allow for dynamic synergy or cooperativity of binding or dissociation of specific ABPs. It is

proposed that the properties of F-actin are modified upon binding by ABP, with long-range effects that subsequently affect the binding of other ABPs. Allosteric interactions can have long-range effects on individual actin filaments, maintaining the filaments in a specific conformation over biologically relevant distances[66, 70], although not necessarily over the entire length of the actin filaments[61]. Thus, binding a single ABP may be sufficient to modify the structure of the filament over a significant distance[68, 72], explaining why additional ABPs would subsequently bind cooperatively to the filament to form regions of actin filaments saturated with this ABP e.g. binding of ADF/cofilin.

Indirect evidence for such effects comes from the structure and mechanical properties of actin filaments at the molecular scale. Direct visualization of how ABPs bind to F-actin and influence the structure and conformation of the decorated actin segment, as well as the probability of ABPs binding and structural effects at the neighboring F-actin sites, can reveal fundamental aspects of ABP interactions and ABPs induced F-actin remodeling at the macromolecular level. Cooperativity is an important property in the regulation and function of several ABPs such as cofilin, tropomyosin[72] etc. Cooperativity of protein- protein binding is defined as positive if the binding of one protein molecule strengthens the binding of subsequent molecules, and as negative if the binding of one molecule weakens the binding of subsequent molecules. Quantitative measurements of cooperativity typically rely on fitting the Hill equation[73] to protein- protein binding data, considering actin as an infinitely cooperative lattice with n sites that exist in only two forms, fully bound or unbound states. The binding density ν (protein molecules bound per actin subunit) is given by

$n = K_a [L]^n_H / 1 + K_a [L]^n_H$ where [L] is the concentration of free protein at equilibrium, K_a is the association equilibrium constant, and n_H is the Hill coefficient. In case of all-or-none binding, the

Hill cooperativity coefficient *n* indicates the binding stoichiometry, but when cooperativity occurs and the stoichiometry is known from other data, then *n* differs from the exact stoichiometry and provides fundamental information about intra-molecular communication [74-75]. Recently nearest-neighbor cooperativity model was applied successfully to the binding of cofilin to actin filaments[72]. In bulk studies, individual macromolecules within an ensemble have traditionally been assumed to be identical. However, recent single-molecule methods reveal that the presence of molecular heterogeneity results in lower cooperativity values in bulk measurements[76].

Analyzing the role of heterogeneity in F-actin substructure in the binding cooperativity of ABPs is critical for deriving molecular models of actin interactions

Conventional solution experiments are unable to detect single filament level changes in helical periodicity or conformations of F-actin upon drebrin or other ABP binding. Imaging of dynamic structural changes spreading across the filament in real time would require temporal resolution on the microsecond scale with sub-nm spatial resolution. Fluorescence microscopy, using FRET/ fluorescence correlation spectroscopy, provides information on labeled molecules on a microsecond timescale, but its limited spatial resolution (~300nm) precludes tracking of individual molecules. Evanescent wave fluorescence can detect individual fluorescent molecules, but is unable to resolve closely associated molecules like actin protomers within the filament[77]. Single molecule FRET can directly measure dynamic changes in F-actin, but provides no structurally resolved information on changes such as in the helical parameters of F-actin [78]. The binding characteristics of ABPs are frequently derived from dynamic fluorescence measurements such as TIRF (Total Internal Reflection Fluorescence) Microscopy[79], allowing

for preliminary conclusions regarding the effect of these proteins on filaments size distribution, assembly or severing [80-82]. For example, drebrin$_{1-300}$ binding to actin filaments was imaged in a recent study by a two-color TIRF microscopy (Fig. 4).

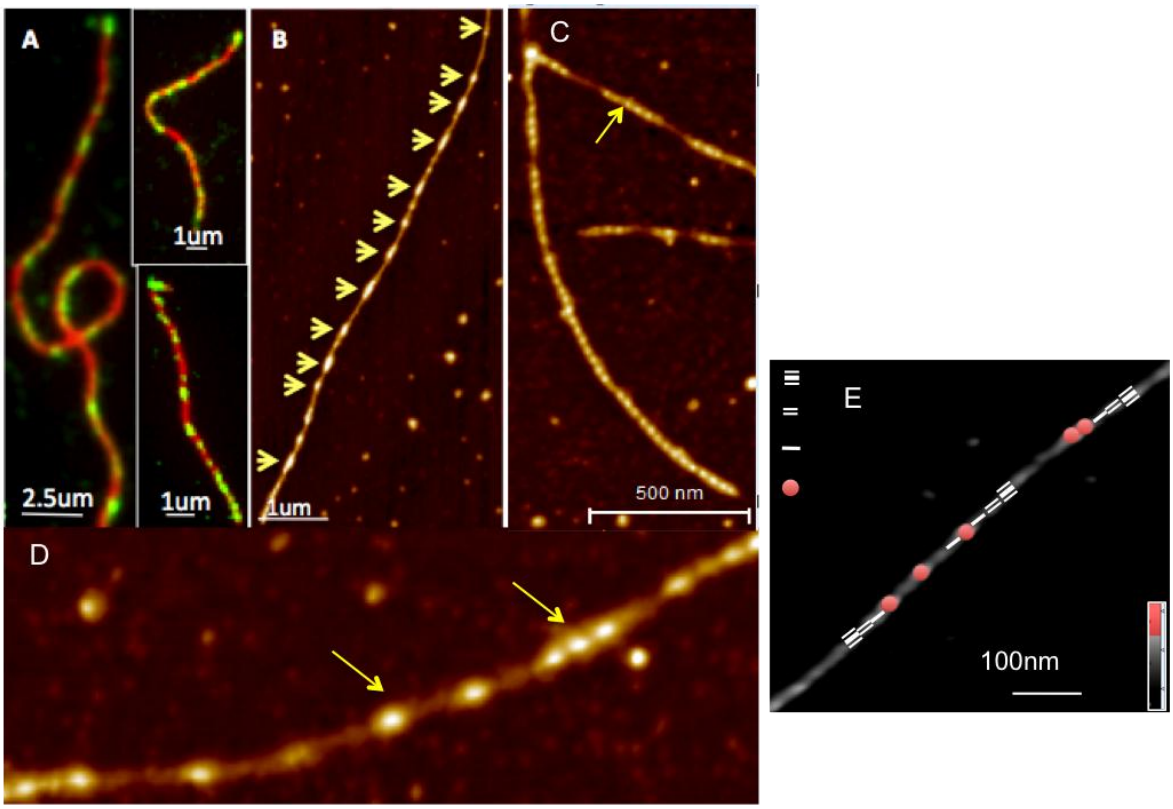

Fig. 4 (A) TIRF imaging revealed a cluster-like attachment of drebrin (green) to the actin filaments (red), providing the first indications of cooperative interaction between Drebrin$_{1-300}$ and F-actin. (B) AFM images of F-actin decorated with DrebrinA$_{1-300}$ at sub-saturating ratios, reveal their cooperative binding (binding clusters are marked by yellow arrows along individual filament). (C and D) show drebrin clusters along actin filament at higher resolution. (E) Representation of the positions for drebrin-unbound F-actin helix of 1st, 2nd and 3rd neighbor relative to the drebrin-bound helix from AFM image of partially decorated Drb$_{1-300}$ F-actin Adapted from Sharma S. *et al.* [82] with permission from Cell Press.

Resolution achieved by optical techniques limits the measuring/mapping of nanoscale protein binding and cluster assembly on individual actin filaments. These current techniques employ bulky probes, which may affect the protein and have insufficient resolution to measure the size of the bound protein cluster (<sub diffraction limit i.e. 300nm) and the resulting structural changes in F-actin. Clearly, high-resolution images of actin-ABPs complexes are required to enable measurement of local changes in F-actin induced by ABPs. Although such a resolution is achieved in EM analysis of these complexes, the averaging of structural information inherent in EM analysis precludes the examination of individual F-actin helical structures to distinguish between localized (directly bound) and transmitted (unbound regions) effects of ABPs.

In contrast to ensemble measurements and single molecule spectroscopy techniques, one can easily measure the ABP binding assembly (cluster size) and F-actin modulation at the single filament level, at the nanoscale, via AFM imaging. AFM allows imaging of individual actin filaments that are partially saturated with ABPs and yields high-resolution quantitative 3D structural information on the end-to-end contiguous versus non- contiguous protein binding sites under such conditions. Moreover, it enables to analyze changes in helical periodicity of ABP-bound and unbound F-actin regions.

We have shown AFM measurements for drebrin (under-twist)(Fig. 3) and cofilin (over-twist)[56] induced changes in the actin helix (in opposite directions). The same approach can be used to analyze the helical changes in actin filaments for other ABPs. We also measured the ABP binding assembly (nanoscale cluster size) and F-actin modulation at the single filament level via AFM imaging to test if the protein binds in a cooperative manner to F-actin. F-actin

filaments can be partially decorated with ABPs (at under-saturating conditions) to study the binding patterns, cooperative effects, and the influence on F-actin modulation/stabilization by ABP using AFM imaging. If ABP binding has positive co-operativity, clusters of protein will form along the actin filament. Though AFM resolution limits the imaging of individual protein molecules, the fact that ABP may bind in nano-scale clusters along the actin filament makes AFM an excellent tool to directly visualize the overall ABP binding at the single actin filament level. Both non-contiguous ABP bound (decorated) regions of actin filaments and regions free of ABP (undecorated) can be analyzed. The size of the ABP clusters over F-actin would depend on the density of binding and the extent of its cooperativity.

Additionally, one can exploit the nanoscale resolution of ABP-actin complexes in AFM to measure directly the periodicity for individual filaments, and thus to determine the helical pitch of the filament both in its bare and ABP bound regions. Our recent study measured the changes in helical periodicity of F-actin upon drebrin binding and the propagation of its binding effects within the filament[83]. AFM showed that drebrin binding induces helical changes in F-actin in both the directly occupied and the unbound regions, i.e., it reveals the propagation of the drebrin-induced structural changes to the adjacent, undecorated regions on the filaments. This work provides the first un-averaged experimental information on the remodeling of ABP occupied and unoccupied regions of F-actin at the single-filament level.

Mechanics of single molecule F-actin-ABPs complexes

The mechanical properties of actin filaments are tightly correlated with the helical structure of the polymer, and it is expected that factors affecting the structure of the filament also affect its flexibility. There are several ways in which ABPs are known to modulate actin

mechano-structure and function. ABPs have been shown to alter filament rigidity by cross-linking them, or to create bends and promote cooperativity in actin[22], which may facilitate regulation or remodeling of the actin cytoskeleton. Mechanical properties of actin have been investigated thus far using a number of techniques including EM, fluorescence and thermal fluctuation measurements [57-58]. The resolution achievable with AFM imaging allows determining the local flexibility of specific sites within the filament similar to other techniques, but at a higher resolution (helix level). Flexibility of actin filaments can be obtained from a comparison of the contour length and the mean-square distance between the ends or other sites in the molecule[84-85]. For semi flexible polymer like actin (Lp~L), Worm-Like Chain (WLC) 2D model can be used (with the assumption of equilibration), to determine the persistence length of actin filaments from AFM topography images (Fig. 5). Persistence length (p) is a measure of length-scale for molecule stiffness *i.e*, the distance over which the direction of a polymer segment persists, in the time or ensemble average, owing to limited flexibility of the polymer.

If R is defined as the end-to-end distance of the overall polymer and L is the contour length of the polymer, the relationship between them and the persistence length, p, of the polymer is [86]

$$< R^2 >= \int_0^L \int_0^L < \vec{u}(s) \cdot \vec{u}(s') > ds' ds = \int_0^L \int_0^L e^{-|s-s'|/2p} ds' ds$$
$$\Rightarrow < R^2 >= 4pL(1 - \frac{2p}{L}(1 - e^{-L/2p}))$$

where s, and s’ are two positions on the polymer chain; $\bar{u}$ (s) and $\bar{u}$(s’) are unit vector tangents to the polymer chain at position s and s’. Another method to estimate the persistence length of actin filaments is by measuring the local filament angle distribution [87]. By tracing the actin contours, we can calculate the local bend angle, θ, of two consecutive segments at different step

size l (vector length). Using the probability distribution function for the WLC model in two dimensions it can be shown that

$$\langle \cos(\theta) \rangle = e^{-l/2p}$$

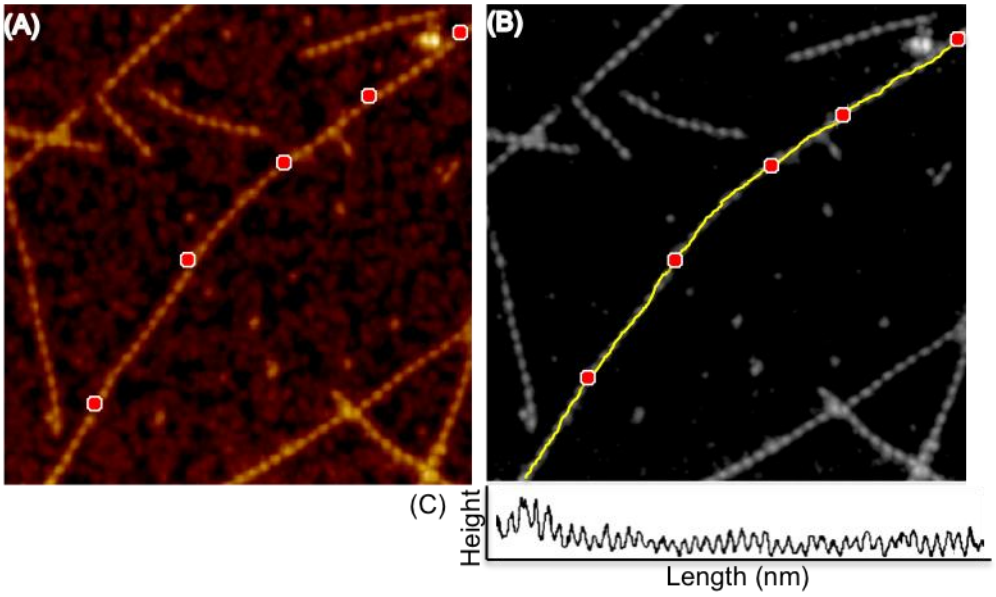

Fig. 5 Representative spline (medial axis) profile along drebrin-F actin (A) Points chosen along filament length shown as red markers (B) Spline fit along the markers showing in yellow (C) Profile along chosen points on the filament.

Volume analysis of ABP-F-actin complexes

The binding ratio of ABP to actin can be determined from flattened and plane-fitted AFM images by measuring the overall increase in the volume of actin-ABP complex compared to bare actin filaments (Fig. 6). The surface height is measured using histogram function and subtracted from the measured height of actin or ABP bound actin for volume determination. The filaments (each segment length =37nm) are then detected individually using the grain analysis function. The density slice selects the pixels above the surface that represent the filament section to be analyzed. The image analysis function scans the image and detects all of the highlighted segments within the density slice and generates height and area information, which permits the calculation of the net volume of actin filaments. Increase in the overall volume of actin filaments upon ABP binding compared to bare F-actin can thus be used to assess the number of ABP molecules bound per actin helical repeat.

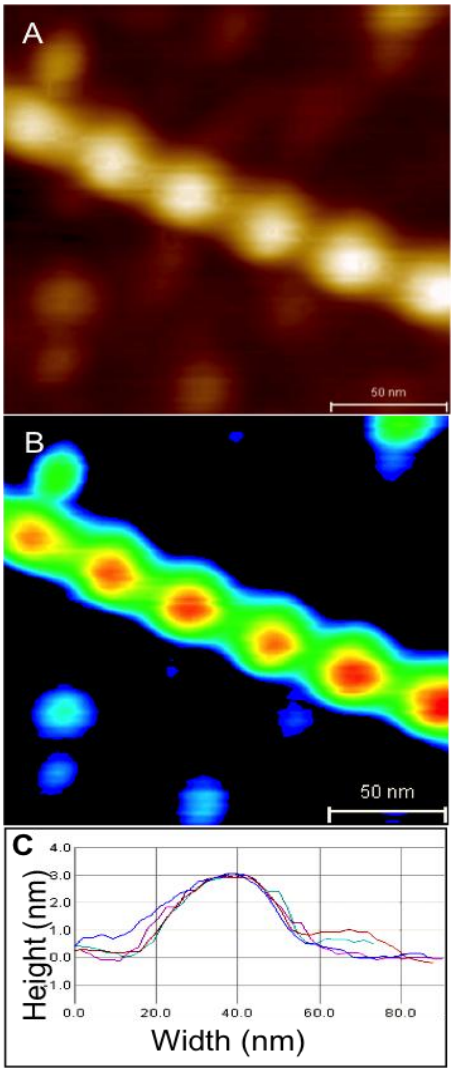

Fig. 6 Volume determination of ABP-F-actin AFM 3D images (A) Unprocessed AFM tapping mode height image (B) Zero order flattened and background subtracted image (C) Multiple line profiles taken along filament cross section to detect height and width of the filaments. Adapted from Sharma S. *et al.* [55] with permission from American Chemical Society.

Imaging F-actin ABP complexes under physiological conditions

A major advantage of AFM is the capability of high-resolution imaging of biomolecules in their native environment. However, to date AFM studies on actin -ABP complexes have been done mostly in ambient air and therefore in non-physiological conditions. AFM has been used previously to study complex processes such as the dynamics of proteins[88] and DNA-protein interactions[89]. AFM imaging in solution is difficult since the F-actin-substrate interactions need to be optimized, in order to withstand tip-sample interaction forces during imaging. Here we present the sub-nanometer AFM images of rabbit skeletal F-actin obtained in buffer conditions (Fig. 7). Data obtained in air and in solution have been compared and found to be consistent in helix pitch (36nm) for bare F-actin. AFM imaging under physiological conditions in aqueous solution was also used previously to show distinct variations in monomer stacking and increase in pitch of the helix for malarial parasite actin compared to skeletal actin filaments[90].

Additionally, the development of High-speed atomic force microscopy (HS-AFM)[91-92] has enabled studying the structure and dynamics of functioning biomolecules simultaneously. Kodera *et al*.[93] used HS-AFM to directly observe myosin V moving along actin filaments with unprecedented time resolution. The work provided visual evidence supporting the 'swinging lever-arm' model for myosin motility.

Frequency-modulation AFM (FM-AFM)[94] is another imaging mode where the tip–sample interaction is probed via minute changes in the cantilever resonance frequency (unlike amplitude in tapping mode). FM-AFM has been successfully applied recently for single biomolecules to visualize, different structural conformations of the two-polynucleotide strands in the DNA double helix[95].

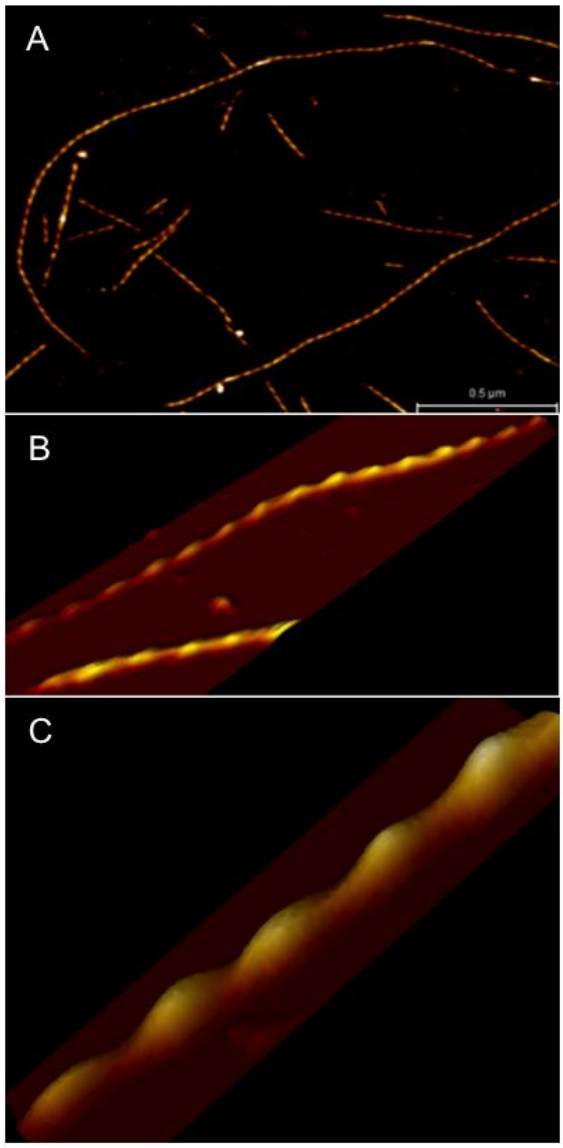

Fig. 7 AFM imaging of F-actin under physiological conditions (A) Several actin filaments imaged showing stable attachment to silane modified mica surface (B) Higher resolution image of F-actin and (C) 3D view of F-actin filament section showing well resolved helical periodicity.

Mapping Nanomechanical changes in ABP-F-actin complexes

Stress and strain are important factors modulating cells reaction to their environment. Since actin filaments are associated with a large number of actin-binding proteins, including nucleators, capping proteins and cross-linking proteins, it is interesting to understand how these other proteins modulate and regulate the response of an actin filament to mechanical stress. Stress induced structural modifications in actin filaments have been studied biochemically or spectroscopically[96-98]. Tension on an actin filament can regulate its disassembly by ABPs[99]. Hayakawa *et al.* [100]show that actin filament binding and severing by ADF/cofilin are inhibited when tension is generated in the filament. They also show that in cells ADF/cofilin localizes more strongly to relaxed than stretched actin stress fibers[100]. Thus, mechanical stress and contractility may regulate the dynamics of actin filaments in cells, perhaps by altering filament twist to inhibit ADF/cofilin binding. Yet, it is still not fully understood how forces affect the molecular interactions and what role ABPs play in regulating the mechanical behavior and remodeling of F-actin. How strong a force is required to pull the associated proteins apart in the absence or presence of other ABPs, are some of the basic questions that can potentially be addressed using AFM based force spectroscopy measurements. One can obtain combined topography and rupture force maps of bare F-actin, and fully and partially decorated F-actin-ABP complexes. Furthermore, AFM tips can also be functionalized [101] [102] [103] to measure and map the unbinding of ABPs as the molecules are pulled away from F-actin.

Thus, AFM imaging yields information on: (1) nanoscale 3D morphology of single filaments, helix parameters, and variations in helical twist, binding cooperativity, filament bending modulus and persistence length; (2) Quantification of ABPs induced “individual” change in helical twists of the filaments in the regions directly in bound by the protein; (3)

Propagation of changes if any, and the extent of the propagation of helical twist change in neighboring unbound regions of F-actins; and (4) Direct measurement of bound protein cluster size and assembly, for determination of the binding cooperativity of the proteins at a single filament level.

Higher-order ABP-F-actin structures

Within the cells, actin filaments rarely exist as isolated single filaments but instead associate into higher-order structures or networks, together with over 60 different ABPs. Such higher-order cellular organization of actin is crucial to both the form and function of cells. Modest changes in the concentration of ABPs can significantly modify the structure of the network because they can both bundle and cross-link the actin filaments. These structural changes can lead to concomitant change in the structure, and mechanical properties. The changes in structure occur over a wide range of length scales, ranging from a few nanometers to several micrometers.

The current AFM technology is powerful in visualizing nanoscale structural and dynamic (HS-AFM) events of isolated and purified biological molecules such as F-actin but limited in the dynamic observation of the outer surface and the interior of live cells (i.e. *in situ* imaging)[104-106]. The extension of high-speed AFM for imaging live cells, which allows direct in situ observation of dynamic processes of biomolecules, remains an exciting challenge in the near future. Emerging super resolution light microscopy techniques such as Stimulated emission depletion (STED)[107] allow sub-diffraction limit visualization of cellular structures[108] and are beginning to provide detailed information about the higher-order actin structures within the cells (Fig. 8), if not single filament level. It will be interesting to see how combining the

capabilities of STED and AFM could improve our understanding of actin filaments and networks regulated by various ABPs within the cellular environments.

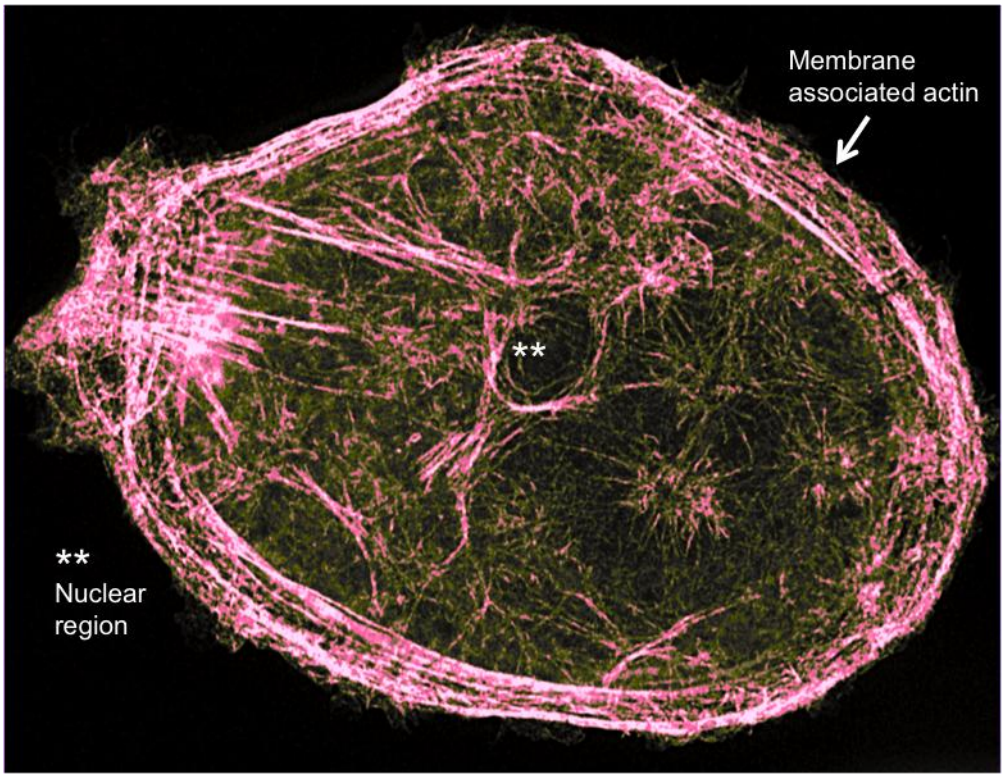

Fig. 8 Super-resolution STED image of an ovarian cancer cell showing detailed actin cytoskeleton. Adapted from Sharma S. *et al.* [97] with permission from American Chemical Society.

5.4 Summary

The unique capability of AFM as a biophysical nano-characterization tool in studying F-actin remodeling induced by ABPs, not offered by other biochemical and biophysical techniques, includes sub-nanometer resolution–quantification at the single filament level - of structural (individual helix determination, volume analysis) and mechanical changes (persistence length) induced by the bound ABPs. AFM offers direct visualization of cooperative binding interactions and enables determination of the extent of propagation of these changes within the unbound regions of filaments, as demonstrated in our proof-of-concept studies involving neuronal ABP-drebrin. AFM based approach can be used to study F-actins interactions with cofilin, tropomyosin, coronin, formin, and other ABPs, and to obtain fundamental and quantitative molecular level information on the structural and biophysical F-actin remodeling and its regulation by ABPs at the single filament level.

5.5 References

1. Alberts, B., *The cell as a collection of protein machines: Preparing the next generation of molecular biologists.* Cell, 1998. **92**(3): p. 291-294.

2. Otterbein, L.R., P. Graceffa, and R. Dominguez, *The crystal structure of uncomplexed actin in the ADP state.* Science, 2001. **293**(5530): p. 708-11.

3. Chen, H., B.W. Bernstein, and J.R. Bamburg, *Regulating actin-filament dynamics in vivo.* Trends Biochem Sci, 2000. **25**(1): p. 19-23.

4. Engqvist-Goldstein, A.E. and D.G. Drubin, *Actin assembly and endocytosis: from yeast to mammals.* Annu Rev Cell Dev Biol, 2003. **19**: p. 287-332.

5. Parsons, J.T., A.R. Horwitz, and M.A. Schwartz, *Cell adhesion: integrating cytoskeletal dynamics and cellular tension.* Nat Rev Mol Cell Biol, 2010. **11**(9): p. 633-43.

6. Kaksonen, M., C.P. Toret, and D.G. Drubin, *Harnessing actin dynamics for clathrin-mediated endocytosis.* Nat Rev Mol Cell Biol, 2006. **7**(6): p. 404-14.

7. Paul, A.S. and T.D. Pollard, *Review of the mechanism of processive actin filament elongation by formins.* Cell Motil Cytoskeleton, 2009. **66**(8): p. 606-17.

8. Rouiller, I., et al., *The structural basis of actin filament branching by the Arp2/3 complex.* J Cell Biol, 2008. **180**(5): p. 887-95.

9. Dominguez, R., *Actin filament nucleation and elongation factors--structure-function relationships.* Crit Rev Biochem Mol Biol, 2009. **44**(6): p. 351-66.

10. Schmid, M.F., et al., *Structure of the acrosomal bundle.* Nature, 2004. **431**(7004): p. 104-107.

11. McCullough, B.R., et al., *Cofilin increases the bending flexibility of actin filaments: implications for severing and cell mechanics.* J Mol Biol, 2008. **381**(3): p. 550-8.

12. Kueh, H.Y., et al., *Actin disassembly by cofilin, coronin, and Aip1 occurs in bursts and is inhibited by barbed-end cappers.* J Cell Biol, 2008. **182**(2): p. 341-53.

13. Gandhi, M., B.L. Goode, and C.S.M. Chan, *Four novel suppressors of gic1 gic2 and their roles in cytokinesis and polarized cell growth in Saccharomyces cerevisiae.* Genetics, 2006. **174**(2): p. 665-678.

14. Chhabra, E.S. and H.N. Higgs, *The many faces of actin: matching assembly factors with cellular structures.* Nat Cell Biol, 2007. **9**(10): p. 1110-21.

15. Holmes, K.C., et al., *ATOMIC MODEL OF THE ACTIN FILAMENT.* Nature, 1990. **347**(6288): p. 44-49.

16. Rayment, I., et al., *Structure of the actin-myosin complex and its implications for muscle contraction.* Science, 1993. **261**(5117): p. 58-65.

17. Rayment, I., et al., *Three-dimensional structure of myosin subfragment-1: a molecular motor.* Science, 1993. **261**(5117): p. 50-8.

18. Dominguez, R., et al., *Crystal structure of a vertebrate smooth muscle myosin motor domain and its complex with the essential light chain: Visualization of the pre-power stroke state.* Cell, 1998. **94**(5): p. 559-571.

19. Fedorov, A.A., et al., *Structure determination of yeast cofilin.* Nat Struct Biol, 1997. **4**(5): p. 366-9.

20. Volkmann, N., et al., *Structure of Arp2/3 complex in its activated state and in actin filament branch junctions.* Science, 2001. **293**(5539): p. 2456-9.

21. McLaughlin, P.J., et al., *Structure of gelsolin segment 1-actin complex and the mechanism of filament severing.* Nature, 1993. **364**(6439): p. 685-92.

22. McGough, A., et al., *Cofilin changes the twist of F-actin: implications for actin filament dynamics and cellular function.* J Cell Biol, 1997. **138**(4): p. 771-81.

23. Lukoyanova, N., et al., *Each actin subunit has three nebulin binding sites: implications for steric blocking.* Curr Biol, 2002. **12**(5): p. 383-8.

24. Schutt, C.E., et al., *The structure of crystalline profilin-beta-actin.* Nature, 1993. **365**(6449): p. 810-6.

25. Galkin, V.E., et al., *High-resolution cryo-EM structure of the F-actin-fimbrin/plastin ABD2 complex.* Proc Natl Acad Sci U S A, 2008. **105**(5): p. 1494-8.

26. Tang, J., D.W. Taylor, and K.A. Taylor, *The three-dimensional structure of alpha-actinin obtained by cryoelectron microscopy suggests a model for Ca(2+)-dependent actin binding.* J Mol Biol, 2001. **310**(4): p. 845-58.

27. Volkmann, N., et al., *An atomic model of actin filaments cross-linked by fimbrin and its implications for bundle assembly and function.* J Cell Biol, 2001. **153**(5): p. 947-56.

28. Galkin, V.E., et al., *The utrophin actin-binding domain binds F-actin in two different modes: implications for the spectrin superfamily of proteins.* J Cell Biol, 2002. **157**(2): p. 243-51.

29. Oda, T., et al., *The nature of the globular- to fibrous-actin transition.* Nature, 2009. **457**(7228): p. 441-5.

30. Murakami, K., et al., *Structural basis for actin assembly, activation of ATP hydrolysis, and delayed phosphate release.* Cell, 2010. **143**(2): p. 275-87.

31. Voss, N.R., et al., *Software tools for molecular microscopy: an open-text Wikibook.* Methods Enzymol, 2010. **482**: p. 381-92.

32. Binnig, G., C.F. Quate, and C. Gerber, *Atomic force microscope.* Phys Rev Lett, 1986. **56**(9): p. 930-933.

33. Radmacher, M., et al., *From molecules to cells: imaging soft samples with the atomic force microscope.* Science, 1992. **257**(5078): p. 1900-1905.

34. Bustamante, C., et al., *Circular DNA molecules imaged in air by scanning force microscopy.* Biochemistry, 1992. **31**(1): p. 22-6.

35. Hansma, H.G. and J.H. Hoh, *Biomolecular imaging with the atomic force microscope.* Annu Rev Biophys Biomol Struct, 1994. **23**: p. 115-39.

36. Muller, D.J., et al., *Imaging purple membranes in aqueous solutions at sub-nanometer resolution by atomic force microscopy.* Biophys J, 1995. **68**(5): p. 1681-6.

37. Muller, D.J. and Y.F. Dufrene, *Atomic force microscopy as a multifunctional molecular toolbox in nanobiotechnology.* Nat Nanotechnol, 2008. **3**(5): p. 261-9.

38. Sharma, S. and G. J.K, *Atomic Force Microscopy for Medicine,* in *Life at the nanoscale: Atomic Force Microscopy of live cells*, Y. Dufrene, Editor. 2011, Pan Stanford Publishing. p. 421-436.

39. Hinterdorfer, P. and Y.F. Dufrene, *Detection and localization of single molecular recognition events using atomic force microscopy.* Nature Methods, 2006. **3**(5): p. 347-355.

40. Muller, D.J., et al., *Force probing surfaces of living cells to molecular resolution.* Nat Chem Biol, 2009. **5**(6): p. 383-90.

41. Florin, E.L., V.T. Moy, and H.E. Gaub, *Adhesion forces between individual ligand-receptor pairs.* Science, 1994. **264**(5157): p. 415-417.

42. Ohnesorge, F. and G. Binnig, *True atomic resolution by atomic force microscopy through repulsive and attractive forces.* Science, 1993. **260**(5113): p. 1451-6.

43. Hansma, H.G., et al., *Recent advances in atomic force microscopy of DNA.* Scanning, 1993. **15**(5): p. 296-9.

44. Fotiadis, D., et al., *Structural characterization of two aquaporins isolated from native spinach leaf plasma membranes.* J Biol Chem, 2001. **276**(3): p. 1707-14.

45. Schabert, F.A., C. Henn, and A. Engel, *Native Escherichia coli OmpF porin surfaces probed by atomic force microscopy.* Science, 1995. **268**(5207): p. 92-4.

46. Scheuring, S., et al., *High resolution AFM topographs of the Escherichia coli water channel aquaporin Z.* EMBO J, 1999. **18**(18): p. 4981-7.

47. Scheuring, S., et al., *Nanodissection and high-resolution imaging of the Rhodopseudomonas viridis photosynthetic core complex in native membranes by AFM. Atomic force microscopy.* Proc Natl Acad Sci U S A, 2003. **100**(4): p. 1690-3.

48. Kuznetsov, Y., P.D. Gershon, and A. McPherson, *Atomic force microscopy investigation of vaccinia virus structure.* J Virol, 2008. **82**(15): p. 7551-66.

49. Kuznetsov, Y.G., et al., *Atomic force microscopy investigation of human immunodeficiency virus (HIV) and HIV-infected lymphocytes.* J Virol, 2003. **77**(22): p. 11896-909.

50. Ikai, A., et al., *Atomic force microscopy of bacteriophage T4 and its tube-baseplate complex.* FEBS Lett, 1993. **326**(1-3): p. 39-41.

51. McPherson, A. and Y.G. Kuznetsov, *Atomic force microscopy investigation of viruses.* Methods Mol Biol, 2011. **736**: p. 171-95.

52. Hansma, H.G., et al., *TectoRNA and 'kissing-loop' RNA: atomic force microscopy of self-assembling RNA structures.* J Microsc, 2003. **212**(Pt 3): p. 273-9.

53. Fujita, Y., K. Kobayashi, and T. Hoshino, *Atomic force microscopy of collagen molecules. Surface morphology of segment-long-spacing (SLS) crystallites of collagen.* J Electron Microsc (Tokyo), 1997. **46**(4): p. 321-6.

54. Adamcik, J., et al., *Understanding amyloid aggregation by statistical analysis of atomic force microscopy images.* Nat Nanotechnol, 2010. **5**(6): p. 423-8.

55. Shao, Z., D. Shi, and A.V. Somlyo, *Cryoatomic force microscopy of filamentous actin.* Biophys J, 2000. **78**(2): p. 950-8.

56. Sharma, S., et al., *Atomic force microscopy reveals drebrin induced remodeling of f-actin with subnanometer resolution.* Nano Lett, 2011. **11**(2): p. 825-7.

57. Takebayashi, T., Y. Morita, and F. Oosawa, *Electronmicroscopic investigation of the flexibility of F-actin.* Biochim Biophys Acta, 1977. **492**(2): p. 357-63.

58. Isambert, H., et al., *Flexibility of actin filaments derived from thermal fluctuations. Effect of bound nucleotide, phalloidin, and muscle regulatory proteins.* J Biol Chem, 1995. **270**(19): p. 11437-44.

59. Reisler, E. and E.H. Egelman, *Actin structure and function: what we still do not understand.* J Biol Chem, 2007. **282**(50): p. 36133-7.

60. Trachtenberg, S., et al., *Actin and flagellar filaments: two helical structures with variable twist.* Ann N Y Acad Sci, 1986. **483**: p. 88-99.

61. Galkin, V.E., et al., *Structural polymorphism in F-actin.* Nat Struct Mol Biol, 2010. **17**(11): p. 1318-23.

62. Ott, A., Libchaber, A, *Measurement of the persistence length of polymerized actin using fluorescence microscopy.* Phys. Rev. E Stat. Phys. Plasmas Fluids Relat. Interdiscip. Topics, 1993. **48**: p. R1642-45.

63. Egelman, E.H., N. Francis, and D.J. Derosier, *F-actin is a helix with a random variable twist.* Nature, 1982. **298**(5870): p. 131-135.

64. Belmont, L.D., et al., *A change in actin conformation associated with filament instability after Pi release.* Proc Natl Acad Sci U S A, 1999. **96**(1): p. 29-34.

65. Kueh, H.Y. and T.J. Mitchison, *Structural plasticity in actin and tubulin polymer dynamics.* Science, 2009. **325**(5943): p. 960-3.

66. Hild, G., B. Bugyi, and M. Nyitrai, *Conformational dynamics of actin: effectors and implications for biological function.* Cytoskeleton (Hoboken), 2010. **67**(10): p. 609-29.

67. Prochniewicz, E., et al., *Cofilin increases the torsional flexibility and dynamics of actin filaments.* J Mol Biol, 2005. **353**(5): p. 990-1000.

68. De La Cruz, E.M., *How cofilin severs an actin filament.* Biophys Rev, 2009. **1**(2): p. 51-59.

69. Prochniewicz, E. and D.D. Thomas, *Perturbations of functional interactions with myosin induce long-range allosteric and cooperative structural changes in actin.* Biochemistry, 1997. **36**(42): p. 12845-12853.

70. Orlova, A., E. Prochniewicz, and E.H. Egelman, *Structural dynamics of F-actin: II. Cooperativity in structural transitions.* J Mol Biol, 1995. **245**(5): p. 598-607.

71. Prochniewicz, E., et al., *Cooperativity in F-actin: binding of gelsolin at the barbed end affects structure and dynamics of the whole filament.* J Mol Biol, 1996. **260**(5): p. 756-66.

72. De La Cruz, E.M., *Cofilin binding to muscle and non-muscle actin filaments: isoform-dependent cooperative interactions.* J Mol Biol, 2005. **346**(2): p. 557-64.

73. Hill, A.V., *The possible effects of the aggregation of the molecules of hæmoglobin on its dissociation curves.* J. Physiol., 1910. **40**.

74. Weiss, J.N., *The Hill equation revisited: uses and misuses.* Faseb J, 1997. **11**(11): p. 835-41.

75. Wyman, J., Jr., *Linked Functions and Reciprocal Effects in Hemoglobin: A Second Look.* Adv Protein Chem, 1964. **19**: p. 223-86.

76. Solomatin, S.V., M. Greenfeld, and D. Herschlag, *Implications of molecular heterogeneity for the cooperativity of biological macromolecules.* Nat Struct Mol Biol, 2011. **18**(6): p. 732-4.

77. Kovar, D.R., et al., *Control of the assembly of ATP- and ADP-actin by formins and profilin.* Cell, 2006. **124**(2): p. 423-35.

78. Kozuka, J., et al., *Dynamic polymorphism of single actin molecules in the actin filament.* Nat Chem Biol, 2006. **2**(2): p. 83-6.

79. Schneckenburger, H., *Total internal reflection fluorescence microscopy: technical innovations and novel applications.* Curr Opin Biotechnol, 2005. **16**(1): p. 13-8.

80. Kuhn, J.R. and T.D. Pollard, *Real-time measurements of actin filament polymerization by total internal reflection fluorescence microscopy.* Biophys J, 2005. **88**(2): p. 1387-402.

81. Chan, C., C.C. Beltzner, and T.D. Pollard, *Cofilin dissociates Arp2/3 complex and branches from actin filaments.* Curr Biol, 2009. **19**(7): p. 537-45.

82. Cai, L., et al., *Coronin 1B antagonizes cortactin and remodels Arp2/3-containing actin branches in lamellipodia.* Cell, 2008. **134**(5): p. 828-42.

83. Sharma, S., et al., *Molecular cooperativity of drebrin(1-300) binding and structural remodeling of f-actin.* Biophys J, 2012. **103**(2): p. 275-83.

84. Kratky, O. and G. Porod, *RONTGENUNTERSUCHUNG GELOSTER FADENMOLEKULE.* Recueil Des Travaux Chimiques Des Pays-Bas-Journal of the Royal Netherlands Chemical Society, 1949. **68**(12): p. 1106-1122.

85. Landau, L.D., *The Properties of the Green Function for Particles in Statistics.* Soviet Physics Jetp-Ussr, 1958. **7**(1): p. 182-184.

86. Rivetti, C., M. Guthold, and C. Bustamante, *Scanning force microscopy of DNA deposited onto mica: equilibration versus kinetic trapping studied by statistical polymer chain analysis.* J Mol Biol, 1996. **264**(5): p. 919-32.

87. Frontali, C., et al., *An absolute method for the determination of the persistence length of native DNA from electron micrographs.* Biopolymers, 1979. **18**(6): p. 1353-73.

88. Rief, M., et al., *Reversible unfolding of individual titin immunoglobulin domains by AFM.* Science, 1997. **276**(5315): p. 1109-12.

89. Rivetti, C., M. Guthold, and C. Bustamante, *Wrapping of DNA around the E.coli RNA polymerase open promoter complex.* EMBO J, 1999. **18**(16): p. 4464-75.

90. Schmitz, S., et al., *Malaria parasite actin polymerization and filament structure.* J Biol Chem, 2010. **285**(47): p. 36577-85.

91. Ando, T., T. Uchihashi, and T. Fukuma, *High-speed atomic force microscopy for nano-visualization of dynamic biomolecular processes.* Progress in Surface Science, 2008. **83**(7-9): p. 337-437.

92. Hansma, P.K., et al., *Applied physics. High-speed atomic force microscopy.* Science, 2006. **314**(5799): p. 601-2.

93. Kodera, N., et al., *Video imaging of walking myosin V by high-speed atomic force microscopy.* Nature, 2010. **468**(7320): p. 72-6.

94. Fukuma, T., et al., *True atomic resolution in liquid by frequency-modulation atomic force microscopy.* Applied Physics Letters, 2005. **87**(3).

95. Leung, C., et al., *Atomic force microscopy with nanoscale cantilevers resolves different structural conformations of the DNA double helix.* Nano Lett, 2012. **12**(7): p. 3846-50.

96. Tsuda, Y., et al., *Torsional rigidity of single actin filaments and actin-actin bond breaking force under torsion measured directly by in vitro micromanipulation.* Proc Natl Acad Sci U S A, 1996. **93**(23): p. 12937-42.

97. Shimozawa, T. and S. Ishiwata, *Mechanical distortion of single actin filaments induced by external force: detection by fluorescence imaging.* Biophys J, 2009. **96**(3): p. 1036-44.

98. Kojima, H., A. Ishijima, and T. Yanagida, *Direct measurement of stiffness of single actin filaments with and without tropomyosin by in vitro nanomanipulation.* Proc Natl Acad Sci U S A, 1994. **91**(26): p. 12962-6.

99. Galkin, V.E., A. Orlova, and E.H. Egelman, *Actin filaments as tension sensors.* Curr Biol, 2012. **22**(3): p. R96-101.

100. Hayakawa, K., H. Tatsumi, and M. Sokabe, *Actin filaments function as a tension sensor by tension-dependent binding of cofilin to the filament.* J Cell Biol, 2011. **195**(5): p. 721-7.

101. Yakovenko, O., et al., *FimH forms catch bonds that are enhanced by mechanical force due to allosteric regulation.* J Biol Chem, 2008. **283**(17): p. 11596-605.

102. Sharma, S., et al., *Structural-Mechanical Characterization of Nanoparticle Exosomes in Human Saliva, Using Correlative AFM, FESEM, and Force Spectroscopy.* Acs Nano, 2010. **4**(4): p. 1921-1926.

103. S. Sharma, S.E.F., S.; Gonzalez, O.; Petzold, O.; Baker, W.; Walczak, W.; Yongsunthon, R.; Baker, D.; Gimzewski, J.K, *Influence of Substrates on Hepatocytes: A Nanomechanical Study*. Journal of Scanning Probe Microscopy 2009. **4**(7).

104. Rotsch, C. and M. Radmacher, *Drug-induced changes of cytoskeletal structure and mechanics in fibroblasts: an atomic force microscopy study.* Biophys J, 2000. **78**(1): p. 520-35.

105. Azeloglu, E.U. and K.D. Costa, *Atomic force microscopy in mechanobiology: measuring microelastic heterogeneity of living cells.* Methods Mol Biol, 2011. **736**: p. 303-29.

106. Arce, F.T., et al., *Heterogeneous elastic response of human lung microvascular endothelial cells to barrier modulating stimuli.* Nanomedicine, 2013.

107. Hell, S.W. and J. Wichmann, *Breaking the Diffraction Resolution Limit by Stimulated-Emission - Stimulated-Emission-Depletion Fluorescence Microscopy.* Optics Letters, 1994. **19**(11): p. 780-782.

108. Sharma, S., et al., *Correlative nanomechanical profiling with super-resolution F-actin imaging reveals novel insights into mechanisms of cisplatin resistance in ovarian cancer cells.* Nanomedicine, 2011.